UNIVERSITY OF PADOVA

32ND PHD CYCLE

DEPARTMENT OF MANAGEMENT AND ENGINEERING

MECHATRONICS AND PRODUCT INNOVATION ENGINEERING

Stability Monitoring and Controller Autotuning of Power Converters in DC Microgrid

---

Supervisor:
Prof. Paolo Mattavelli

PhD Candidate:
Aram Khodamoradi

2019

Abstract

Recently, there has been an increasing interest towards grouping several power resources together with some loads as well as some energy storage systems in a *microgrid* environment. This is mainly because a high number of distributed energy resources (DERs), such as renewable energies and energy storage systems can be integrated in a microgrid environment, that, in turn, will lead to a reduction in the transmission and distribution losses, the overall system costs, as well as the CO_2 emissions. In addition, as the generation is going to be mostly near to the consumption point, the power quality, efficiency and reliability will be significantly increased. Microgrids are also a smart choice for the remote locations that are beyond reach of the current grid.

Dc microgrids bring with some advantages over their ac counter part. For instance, they are more compatible with the dc nature of many DERs such as photovoltaics and energy storage systems. Also, the inductive voltage drop is removed in a dc system. Thus, a large number of DERs can be integrated into a dc microgrid by taking advantage of power electronic converters, that introduce several control and operation benefits.

Power converters used in dc microgrids are usually equipped with several control loops. When many converters are connected to a common dc bus, the dynamic performance of some control loops may be different from the behavior designed for the stand-alone converter, due to possible effects of the interconnected converters. This issue—which is typically referred to as the 'interaction effect' of multiple parallel converters— can lead to stability and performance concerns in a dc microgrid. Thus, interaction effect on a generic control loop depends on the interconnected power converters, for instance, on their topology, control structure, parameters, etc. In order to know the real-time control performance and stability of the control loops within dc microgrid power converters, it is important to equip the converters with online stability monitoring tools. The monitored data will not only include the internal stability conditions of each loop, but also take the interaction effect into account. Subsequently, some corrective actions can be introduced in the system to maintain a desired dynamic performance and avoid instability. In addition, in the context of *smart microgrids*, the advanced monitoring tools, as well as adaptive control and management actions are of a wide interest.

This work firstly, investigates an on-line stability monitoring technique that is inspired by the Middlebrook's injection method. This method allows to estimate and monitor the stability margins of a generic control loop (e.g., current loop, voltage loop, droop loops, etc.) within dc microgrid power converters. Since we target a multi-converter environment, the presence of multiple perturbations coming from the monitoring units of several converters is also taken into account. Secondly, two different on-line tuning techniques are proposed, that both aim to achieve the desired phase margin for a generic control loop at the reference bandwidth. These methods are based on injecting a small-signal perturbation at the desired reference crossover frequency into the loop under study. In other cases—where a full picture about the performance of different loops over the entire bandwidth is desired—multiple orthogonal pseudo-random binary sequences (PRBSs) are proposed to be simultaneously injected in several control loops. This will provide the frequency responses of all the loops in a single measurement cycle. Finally, in order to further assess the microgrid-level stability and dynamic performance, some of the monitored data are effectively used to estimate the dc bus impedance, which has been shown to provide a measure of the stability and performance of the entire microgrid. This part of the work is carried out during the research period spent in the power electronics group, at the University of South Carolina, SC, USA, under supervision of prof. Enrico Santi. All the stability monitoring and adaptive tuning functions are experimentally validated in a laboratory setup that emulates a dc microgrid.

Dedicated to my parents.

Acknowledgements

First of all, I would like to thank prof. Paolo Mattavelli for providing me with the chance to do a PhD in the power electronics group at the University of Padova. Words are not enough to appreciate his kind understanding and trust, especially since I was coming from a power system and control background, and here I started to learn many things in the field of power electronics. Most of all, during the first year of PhD, this challenging path turned to be enjoyable and rather interesting, due to his mindful help. His kind support also during the research period spent abroad is unforgettable.

During the first year of PhD there were many new things to learn and this challenge would have not been succeeded, if there was not the kind support of my dear colleagues Eng. Guangyuan Liu and Dr. Andrea Petucco. I will always be grateful to them for their enjoyable collaboration and their contribution in the experimental part of my works. Their help and considerations were not limited to the work in the laboratory, and they were always there for any problem during these years.

I also want to thank Dr. Tommaso Caldognetto and prof. Paolo Magnone in the power electronics group at the University of Padova. The useful discussions with them shed light on many technical and writing aspects of my work. The kind help of Dr. Ahmed Abdelhakim upon my arrival to Padova and Vicezna and beyond that is also highly appreciated. Thanks also to other colleagues in the laboratory of Vicenza, namely, Dr. Francesco Cavazzana, Dr. Ludovico Ortombina, Dr. Fabio Tinazzi, and others.

My special thanks to Eng. Hossein Abedini, that I cannot imagine any success for myself without his disinterested support. During the third year of my PhD, he gave a good contribution in most of the experimental validations of our works.

I want to also express my gratitude to all the people of the power electronics group at the University of South Carolina (USC), Columbia, SC, in particular, to prof. Enrico Santi for hosting me in his group during the last five months of my PhD. His flexibility, kindness and useful advises are highly appreciated. I am also thankful

to my friend Eng. Hessamaldin Abdollahi, the PhD student of Prof. Santi that gave a high contribution in our works together and provided a continuous support during my stay in USA, making me more comfortable with the new life situation.

Many thanks to Dr. Tuomas Messo from Tampere University of technology, Finland, for the nice suggestion he gave me during his stay in Padova and after that. Still from Tampere University of technology, I want to thank Dr. Tomi Roinila for the useful discussions that we had at USC where we were both visiting.

Finally, endless thanks to my parents for their unconditional help, their motivating encouragements, and their true endeavor to make the things easier for me.

September 2019
Aram Khodamoradi

Contents

Contents viii

List of Figures xi

List of Tables xvii

1 Introduction 1
- 1.1 DC microgrids 1
- 1.2 Stability of dc microgrids 5
  - 1.2.1 Effect of constant power loads 6
  - 1.2.2 Connection/disconnection of a DER converter 7
  - 1.2.3 Frequently changing microgrids 7
- 1.3 Existing works on stability monitoring and adaptive tuning 8
  - 1.3.1 Loop gain-based methods 8
  - 1.3.2 State space-based methods 10
  - 1.3.3 Impedance-based methods 11
- 1.4 Disseration outline and summary of contributions 12

2 Online stability monitoring of DC microgrid power converters 17
- 2.1 Introduction 17
- 2.2 Concept description 19
- 2.3 Proposed estimation technique 21
  - 2.3.1 Proposed phase margin and crossover frequency estimator 21
  - 2.3.2 Design of the frequency loop regulator $G_{\tilde{f}}$ 23
  - 2.3.3 Gain margin monitoring 25
  - 2.3.4 Perturbation amplitude 26
- 2.4 Multiple converter scenario 28
  - 2.4.1 Non-simultaneous monitoring 28
  - 2.4.2 Simultaneous monitoring 28
- 2.5 Application to droop-controlled converters 30
- 2.6 Simulation and experimental results 31
  - 2.6.1 MT applied to the inner current and voltage loops 34
  - 2.6.2 MT applied to the droop loop 37
  - 2.6.3 Dynamic behavior of the MT 41
- 2.7 Summary 44

3 Autotuning of DC microgrid power converters 47
3.1 Introduction 47
3.2 Concept Description 49
3.3 Proposed tuning techniques 51
    3.3.1 Estimation technique 1 51
    3.3.2 Estimation technique 2 53
    3.3.3 Design of the tuning loop 54
    3.3.4 Unfeasible reference phase margin 57
    3.3.5 Application to the dc microgrid power converters 60
3.4 Case Study and Experimental Results 61
3.5 Summary 66

4 Applying PRBSs for loop gain identification and adaptive tuning 67
4.1 Introduction 67
4.2 Simultaneous frequency response measurement of multiple control loops 72
    4.2.1 Generating orthogonal excitations 72
    4.2.2 Using orthogonal PRBSs in dc microgrid power converters . 75
    4.2.3 Loop gain measurement in multiple converters 76
4.3 Case study 77
4.4 Experimental validation 82
    4.4.1 Simultaneous monitoring of two loop gains 83
    4.4.2 An application of the identified models 88
4.5 Summary 91

5 Using the monitored loop gains for dc bus impedance estimation and damping 93
5.1 Introduction 93
5.2 Interaction stability based on bus impedance 97
5.3 Representation of bus impedance in terms of loop gain 99
    5.3.1 Loop gain of the source converter 99
    5.3.2 Bus impedance estimation 102
    5.3.3 Validation of the bus impedance estimation 103
5.4 Extension to the case of multi-source system 106
5.5 Proposed online monitoring and tuning technique 108
5.6 Case Study and Experimental Results 110
    5.6.1 Before tuning 112
    5.6.2 After tuning 115
5.7 Summary 118

6 Conclusions and Future Work 121

List of Figures

1.1 An example of power system configuration with the recent changes due to the presence of microgrids [6]. 2
1.2 Typical structure of a dc microgrid with several DERs. 4
1.3 Dc microgrid: a multi-converter environment, each converter involving several control loops. 5
1.4 A generic load converter with constant power. 6
1.5 Time- and frequency-domain behaviors of the voltage loop of a buck converter, under connection of either a single converter or two similar converters in parallel to the dc bus. 7
1.6 Frequency response measurement of a generic control loop within SMPS, by injecting a perturbation signal s_p, either wide-band or narrow-band, either at point (1) or (2). 9
1.7 Dividing a dc microgrid with N generic sources and M generic loads into the source-side and the load-side subsystems, and modeling each subsystem through its equivalent impedance. 11

2.1 Stability monitoring of a generic control loop within DER converters. 19
2.2 Scheme of the proposed online stability monitoring technique. . . . 21
2.3 A generic control loop with high phase margin and low gain margin. 26
2.4 Parallel connection of two DER converters to the dc bus, both equipped with the proposed MT. The small-signal perturbations s_{p1}, s_{p2} can also have similar frequencies. 29
2.5 Droop-controlled converter equipped with the proposed stability monitoring unit, that can be activated by an enable signal from supervisory controller. 31
2.6 Dc microgrid prototype under study including three buck converters, each converter implementing the control structure displayed in Fig. 2.5. 32
2.7 Droop loop transfer function of converter #2 in Fig. 2.6: analytical versus experimental data. 33
2.8 Simulation results of the current loop stability monitoring. Parameters listed in Table 2.1 and Table 2.2. 34
2.9 Experimental results of applying MT to the current and the voltage loops of a single buck converter. 35
2.10 Ripples in the input voltage v_{in}, output voltage v_o and inductor current i_L, in presence of small-signal perturbations coming from MT. Time scale : 1 ms/div. 36

2.11 Simulation results of applying MT to the droop loop of the converters in Fig. 2.6. 38
2.12 Experimental results of the simultaneous monitoring of the droop loops of converters #1 and #2 in Fig. 2.6. 39
2.13 Experimental results of applying MT to the droop loop of converter #2 in Fig. 2.6. Time scale : 5 ms/div. 40
2.14 Effect of the LPF cut-off frequency on the monitored crossover frequency ($\tilde{f}$) and phase margin ($\tilde{PM}$). Time scale : 1 ms/div. 41
2.15 Experimental results under transient: opening the switch Sw_1 in Fig. 2.6. Time scale : 5 ms/div. 42
2.16 Experimental results under transient: $R_L \to \frac{R_L}{2}$. During this experiment, the switch Sw_1 is still open. 43
2.17 Stability monitoring and the load sharing under transient: increasing a control parameter (the integral gain of the voltage regulator in this case). Time scale : 200 ms/div. During this experiment, the switch Sw_1 is still open. 44

3.1 Autotuning of a generic control loop T of digitally-controlled power converters. The compensator gains (k_p, k_i, k_d) are tuned by the matrix $\mathbf{G_1}$ (or $\mathbf{G_2}$) to reach zero error $\vec{\varepsilon}$, i.e., to achieve reference stability margins (f_c^*, ϕ_m^*). The error $\vec{\varepsilon}$ can be defined either based on the estimation technique 1 in 3.3.1, or based on the estimation technique 2 in 3.3.2. 50
3.2 Estimation technique 1. 51
3.3 Estimation technique 2. 53
3.4 MIMO feedback system resulting from the tuning scheme shown in Fig. 3.1. 55
3.5 Simulation results of the tuning technique 2 in Fig. 3.3, applied to the voltage loop of a buck converter (converter #1), that works in parallel with a similar converter (converter #2). 58
3.6 Modified version of the tuning scheme shown in Fig. 3.1, allowing to decrease the reference crossover frequency in order to always reach the reference phase margin. 58
3.7 Simulation results of applying the modified tuning technique shown in Fig. 3.6 to the voltage loop of a buck converter (converter #1), that works in parallel with a similar converter (converter #2). . . . 59
3.8 Modified version of the tuning scheme shown in Fig. 3.1, allowing to track maximum reachable bandwidth, under achievement of the reference phase margin. 59
3.9 Simulation results of applying the modified tuning technique shown in Fig. 3.8 to the voltage loop of a buck converter (converter #1), that works in parallel with a similar converter (converter #2). . . . 60
3.10 Droop-controlled DER converter equipped with the proposed autotuning technique addressed in Fig. 3.8. 61
3.11 The laboratory setup emulating an islanded dc microgrid. Each power converter implements the structure shown in Fig. 3.10. 62

3.12 Experimental results of tuning $G_v(s)$ of converter #1, showing the convergence of both ε^R, ε^I to zero, which means that the desired stability margins are achieved. Time scale: 0.5 sec/div. 63
3.13 Experimental results of tuning $G_v(s)$ of converter #1, showing the required changes in the PID gains in order to obtain the desired stability margins. Time scale: 1 sec/div. 63
3.14 Analytical model and experimentally-measured (SFRA) frequency responses of the droop loop of converter #1, before tuning $G_v(s)$. . 64
3.15 Analytical model and experimentally-measured (SFRA) frequency responses of the droop loop of converter #1, after tuning $G_v(s)$. . . 65
3.16 Experimental results of the error vector and the reference crossover frequency, before and after activating the external loop in Fig. 3.8, that tracks the maximum allowable bandwidth. Time scale: 1 sec/div. 65

4.1 Loop gain measurement by injecting a PRBS signal u at any point of the digital feedback loop, for example, before the compensator. . 68
4.2 A pure white noise and a PRBS, together with their corresponding autocorrelations. 69
4.3 Generating M orthogonal PRBS signals (including an MLBS and $M-1$ IRS signals), by using an N-bit feedback shift register. N is an odd integer in this example. 73
4.4 Energy spectra of the PRBSs generated based on the algorithm shown in Fig. 4.3. The generated PRBSs are orthogonal over their common period l_{IRS_m}. 74
4.5 Applying M orthogonal PRBSs to simultaneous identification of M control loops within a dc microgrid power converter. 76
4.6 The dc microgrid model under study. 77
4.7 Structure of the DER converters considered in Fig. 4.6. In this work, the current and the droop control loops (of converter #1) are simultaneously monitored. 78
4.8 Small-signal representation of the open loop gains under study. . . . 80
4.9 Analytical model of the current loop, in (4.13), and the droop loop, in (4.15), compared with the simulation results of simultaneous multiple loop gain identification for converter #1. 82
4.10 Experimental results when converter #1 is perturbed by only injecting IRS at point (2) of Fig. 4.7. The current loop identification is not accurate around the crossover frequency. 85
4.11 Experimental results when converter #1 is perturbed by two orthogonal PRBSs. The signals IRS, and MLBS are respectively injected at point (2), and point (1) of Fig. 4.7. 87
4.12 Effect of increasing f_{gen} (decreasing k_{gen}) on the identification results. 88

4.13 Application of the proposed identification method in adaptive tuning. b_x, b_y are sent to the supervisory controller, where, *i*) the frequency response of G—that is the open loop gain without considering the compensator—at the reference crossover frequency $f^*_{c,d}$ is found: $G(f^*_{c,d})$ *ii*) the voltage regulator G_v is designed accordingly, to reach the reference phase margin $\phi^*_{m,d}$ and the reference crossover frequency for the droop loop $G_D = G \cdot G_v$. Finally, the updated G_v is sent back to the digital controller. 89
4.14 Time schedule of the implemented adaptive tuning algorithm. The orthogonal PRBSs are injected periodically with the cycle T_p. . . . 90
4.15 Experimental results of tuning the G_v parameters (K_{iv}, K_{pv}), based on PRBS identification results. 90
4.16 PRBS-based experimental identification results of the droop loop, before and after tuning G_v. The desired crossover frequency and phase margin are successfully achieved. 91

5.1 An example of dc microgrid with several power electronic converters, each having multiple control loops. The whole system is divided into a source subsystem, and a load subsystem 94
5.2 Impedance-based representation of an interconnected power converter system. 94
5.3 Some examples of different forbidden regions for the minor loop gain, that are less conservative than the Middlebrook criterion (unity circle) [104]. 95
5.4 Typical output impedance Z_S of droop-controlled and voltage-controlled DER converters. 96
5.5 PBSC together with AIR requiring the Nyquist contour of the normalized bus impedance to be confined within an allowable region. . 98
5.6 A generic droop-controlled or voltage-controlled DER converter. . . 100
5.7 Small-signal representation of the voltage-controlled DER converter (Fig. 5.6, when the switch Sw is open). 100
5.8 Simplified versions of the small-signal model in Fig. 5.7. 101
5.9 Loop gain $T_{v,l}$ and bus impedance Z_{bus}. The phase margins read from Fig. 5.9a, and the peak values of bus impedance read from Fig. 5.9b, are listed in Table 5.2. 105
5.10 Loop gain $T^{\#1}_{v,l}$ (when the droop loop is also closed), and bus impedance Z_{bus}. The phase margins read from Fig. 5.10a, and the peak values of bus impedance read from Fig. 5.10b, are listed in Table 5.3. . . . 107
5.11 Proposed online monitoring and tuning scheme. The peak bus impedance $\tilde{k}_b$ is estimated online, based on the phase margin of the voltage loop. The compensator gains of the voltage regulator (k_p, k_i) are, then, tuned by the matrix $\mathbf{A}$ to keep the bus impedance in an allowable region. 109
5.12 The laboratory setup emulating an islanded dc microgrid. The source converter implements the online monitoring and tuning tool in Fig. 5.11. 111

5.13 Analytical and experimentally measured voltage loop gain $T_{v,l}$, with $P_{CPL} = 450$ W. 112
5.14 Analytical and experimentally measured bus impedance Z_{bus}, with $P_{CPL} = 450$ W. 113
5.15 Analytical and experimentally measured voltage loop gain $T_{v,l}$, with $P_{CPL} = 225$ W. 113
5.16 Analytical and experimentally measured bus impedance Z_{bus}, with $P_{CPL} = 225$ W. 114
5.17 Experimental results of the proposed monitoring tool in steady-state and under transient. 114
5.18 Analytical and experimentally measured voltage loop gain $T_{v,l}$, after tuning G_v. 116
5.19 Analytical and experimentally measured bus impedance Z_{bus}, after tuning G_v. 116
5.20 Experimental results of the proposed monitoring and tuning unit. . 117
5.21 Experimental results of the bus voltage step response before and after tuning G_v. 118

List of Tables

2.1 Parameters of the setup shown in Fig. 2.6 32
2.2 Regulators parameters of the converters in Fig. 2.6 33
2.3 Expected values of the stability margins, and the MT results 37

3.1 Parameters of the setup shown in Fig. 3.11 62

4.1 Parameters of the setup shown in Fig. 4.6 78
4.2 Regulators parameters of the converters in Fig. 4.6 79
4.3 Effect of small-signal perturbation in different loops on a_x 84

5.1 Some examples for the assumption that peak value of Z_S occurs close to the voltage loop bandwidth. 104
5.2 Bus impedance estimation based on (5.13) 105
5.3 Bus impedance estimation based on (5.15) 107
5.4 Parameters of the setup shown in Fig. 5.12 111
5.5 Summary of the experimental results of the peak value of bus impedance117

Chapter 1

Introduction

1.1 DC microgrids

In the 1880s, the famous “Battle of the Currents” between Edison’s proposed dc power system and Westinghouse’s ac power system turned out as a big confrontation. The invention of transformers and a number of influential works of Nikola Tesla, resulted in a victory for the ac systems in this industrial war. Later, several breakthrough ac-based devices and principles led to the global acceptance of ac as the fundamental structure for power generation, transmission and distribution systems [1]. Nevertheless, in about half a century later, the invention of transistor changed the game. Transistors were followed by major developments in the field of power electronics, that also enabled transformation of dc voltages, as a byproduct. Since then, the structure of modern power systems is getting largely affected by the presence of power converters [2]. This influence arrived to the point that in the first years of the 21st century, some projects were started to build a dc-based electricity superhighway to carry inexpensive renewable electricity from places such as the Oklahoma panhandle to the east and west of the USA, where the major consumption points are located [3].

The other big change in the structure of power systems has been recently occurring, as more and more ‘microgrids’ are used. In a microgrid environment, usually, some distributed energy resources (DERs), such as renewable energies and energy storage systems, are grouped together with some loads, by taking advantage of power electronic converters. Importantly, the effective properties of the interfacing power converters, allow flexible and efficient integration of an increasing number of DERs in a dc, ac, or hybrid ac-dc microgrid [4, 5]. Hence, microgrids have recently drawn a large attention, due to the economic and environmental reasons. Fig. 1.1 shows this aspect, by providing an example of the traditional power system, in which all the load power is supplied by the conventional power plants, that are mainly based on fossil fuels [6]. Integration of renewable energies in both transmission and distribution levels, leads to a reduction in the need for power plant generation P_1. On the other hand, in Fig. 1.1b, a modern grid example is shown, in which the distribution and transmission networks are reconfigured by including some microgrids. Since in this scenario DERs are more commonly used, the total need for the power plant generation can be tremendously reduced (i.e., $P_2 << P_1$). This, also implies a reduction in the co_2 emissions [7]. Each microgrid can connect to the main grid through an interface converter, that is also responsible for the power delivered to, or taken from the main grid. The fact that the loads are supplied by the DERs existing in the microgrid, leads to a reduction in the need for distribution and transmission lines, the inductive voltage drop, and the overall losses and costs. Furthermore, microgrids help to improve the power

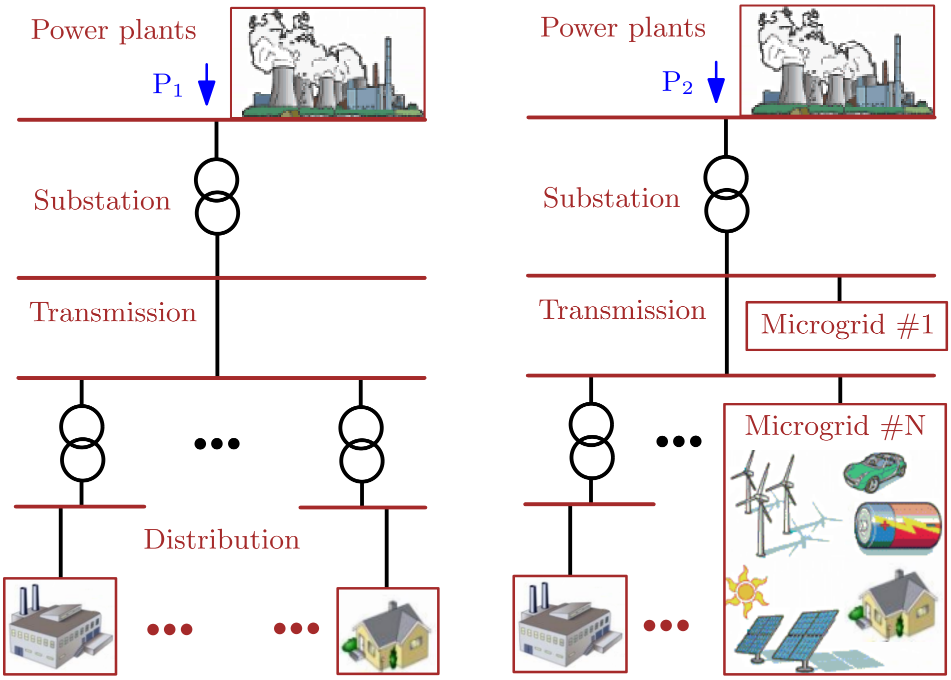

(a) Traditional power system (b) Modern grid

Fig. 1.1. An example of power system configuration with the recent changes due to the presence of microgrids [6].

quality, and efficiency. Microgrids are also a smart solution for the locations that are beyond the reach of the current grid, which is still the case for around 18% of the people around the world [7].

Dc microgirds introduce some advantages over their ac counter part, making them appealing in several applications. For example, dc microgrids are, potentially, more compatible with the dc nature of many DERs, such as, photovoltaic (PV) and energy storage system (ESS). Also, most of the home appliances are dc-based. On the other hand, the transmission and distribution lines are reduced in dc microgrids, leading to a reduction in losses and costs. Other advantages of dc microgrids include, but are not limited to, the higher efficiency, the larger power capacity and the improved controllability compared to ac microgrids [5, 8]. As an example of the statistical comparison, [9] concludes that moving from ac microgrid to its the dc counterpart leads to around 5% increase in the overall efficiency and around 45% decrease in the total cost. This also implies a corresponding decrease in the co_2 emissions.

Several dc microgrid examples are addressed in the literature [2]. From low power cases like cell phones, tablets, digital cameras, laptop computers, etc., to the telecommunication power supply stations, and to higher power level like shipboard and onboard distribution systems, as well as other residential and industrial applications are all the dc microgrid examples [10]. The typical structure of a dc microgrid with different DERs and loads is displayed in Fig. 1.2, which is based on the single-bus configuration. Examples of the multi-bus dc microgrid can be found in [11, 12]. As can be noticed in Fig. 1.2, there are five key elements within a dc microgrid:

(i) Renewable energy resources such as, PV and wind turbine.

(ii) Different loads such as, PC and electric vehicle.

(iii) ESSs that are used for different purposes, such as, ensuring the system reliability [13].

(iv) Electronic-based power conversion stages with different topologies [9, 14–16]. Many of the resources populating a microgrid change their output terminals behavior during normal operation, as the status of the interfaced resources (e.g., renewable source, storage device) or of the microgrid itself changes. Therefore, various kinds of control structures are used to ensure that DERs always keep performing suitably, regardless of the operating conditions. In particular, DER converters usually, involve inner current and voltage loops.

Also, droop control is often applied to address various needs of dc microgrids, such as, bus voltage regulation, power sharing among sources, management of storage units, and islanded operation [17–21]. Droop controller, however, introduces a load-dependent voltage deviation, requiring, thus, a higher-level control to restore [22]. In addition, several source-dependent control strategies might be implemented, such as maximum power point tracking (MPPT) for PV and wind turbines [23, 24], state of charge (SoC) estimation for ESSs [25], and so on.

(v) A microgrid-level supervisory controller. This upper level control is often adopted to communicate with the DER converters, for coordination, optimization, management and other tasks [26–28].

In addition to the five main elements mentioned above, some dc microgrids like the one shown in Fig. 1.2, also include an interfacing dc-ac converter. As mentioned above, the interface converter is also responsible for power control, and some other operation and management tasks [2]. In some other cases, however, the microgrid might operate autonomously, which is also called stand-alone, or islanded dc microgrid. The islanded operation is the common practice for several environments, such as, remote locations.

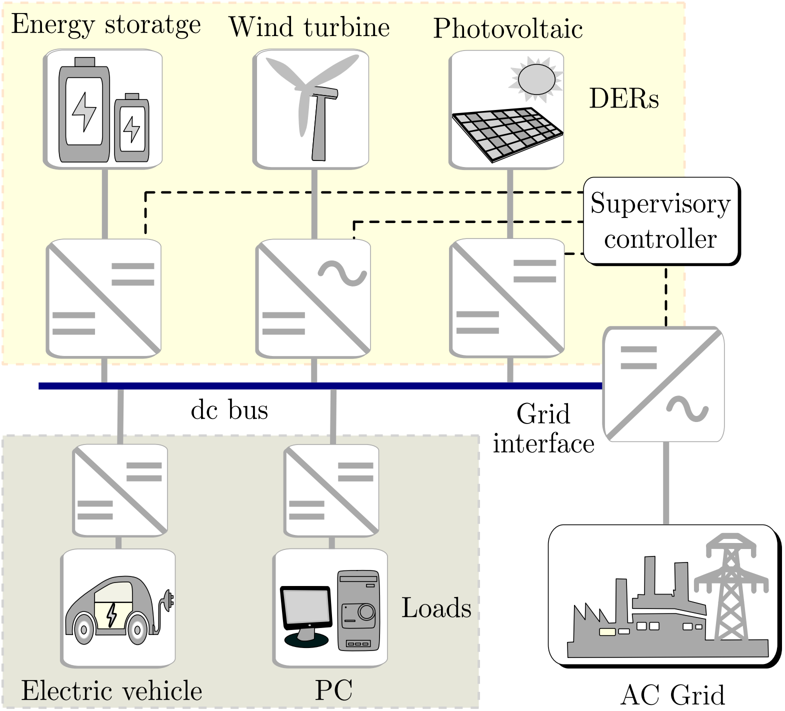

Fig. 1.2. Typical structure of a dc microgrid with several DERs.

1.2 Stability of dc microgrids

The first stability issue was observed in a dc distribution system was faced in an aircraft dc power system in the 1950's [29]. Since then, several experiences report the stability concerns over the interconnection of multiple power electronic converters in a microgrid environment [30]. This subsection, explains this issue and addresses the main motivations to perform investigation on the stability of dc microgrids. As mentioned above, DER converters usually involve multiple control loops. These control loops are often designed for a certain dynamics performance of the stand-alone converter, while they might show different performances when grouped with several other source and load converters [31]. In other words, performance of some loops—usually the slowest and the external ones—may get influenced by several variables, such as, the control structure, and the topology of the interconnected converters. This phenomenon is commonly referred to as converter interactions. Converter interaction can be explained by the fact that, the impedance seen from each converter's terminal—marked by Z_L in Fig. 1.3—changes according to the dc microgrid configuration [32]. This, in turn, leads to some variations in the stability margins of those loops that depend on Z_L. The three examples below, aim to further clarify the potential changes in the dynamic performance of some control loops, when multiple DER converters, and several load converters are grouped in a dc microgrid environment.

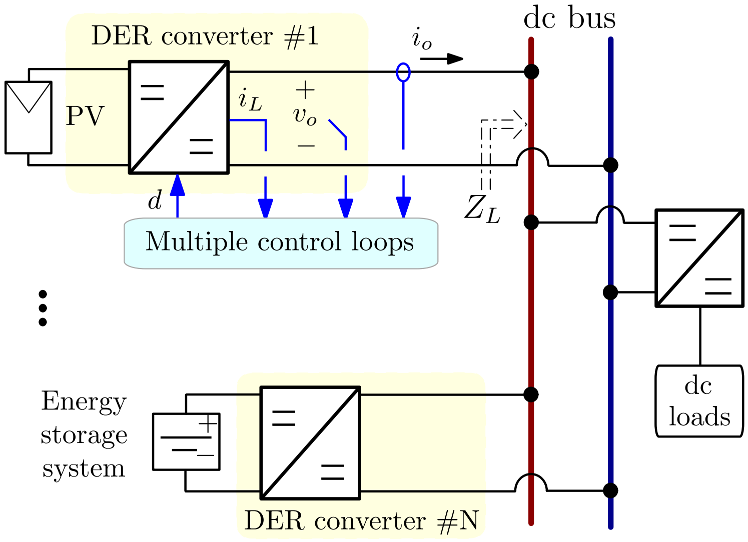

Fig. 1.3. Dc microgrid: a multi-converter environment, each converter involving several control loops.

1.2.1 Effect of constant power loads

The first example of converter interactions is a feedback-controlled load power converter which tends to behave as a constant power load (CPL) at its input terminal on the dc bus. Fig. 1.4 shows a generic load power converter with it's input current i_{in} and voltage v_{in}. Assuming that a constant power is absorbed by the load, one can write the input power P_{in} as follows:

$$P_{in} = v_{in} \cdot i_{in} = const. \tag{1.1}$$

Then, the derivative of (1.1) yields:

$$0 = d(v_{in} \cdot i_{in}) = dv_{in} \cdot I_{in} + V_{in} \cdot di_{in}. \tag{1.2}$$

being, V_{in} and I_{in} the steady-state values of the input current and voltage, respectively. Hence, the incremental input resistance can be defined as:

$$R_{in} = \frac{dv_{in}}{di_{in}} = -\frac{V_{in}}{I_{in}}. \tag{1.3}$$

The negative incremental resistance can also be rewritten based on $I_{in} = \frac{P_{in}}{V_{in}}$, as follows:

$$R_{in} = -\frac{V_{in}^2}{P_{in}} = -\frac{P_{in}}{I_{in}^2}. \tag{1.4}$$

Thus, the tightly-regulated load power converters present a negative incremental impedance within their bandwidth.

The CPL behavior is known to have a destabilizing effect, causing subsystem interaction [33–36]. This issue can be observed at the terminal of either a single load converter, or the group of several load converters.

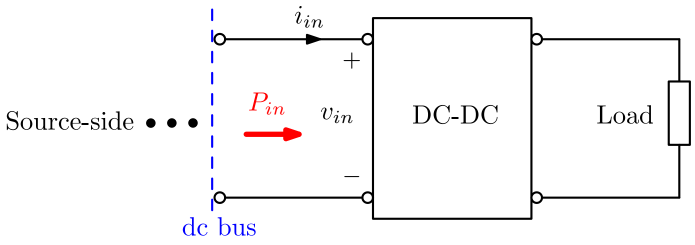

Fig. 1.4. A generic load converter with constant power.

1.2.2 Connection/disconnection of a DER converter

As the second example, let us consider a generic DER supplying a resistive load, through a voltage-controlled buck converter. In the simplest case, if a similar buck converter is connected to the common dc bus, the behavior of the voltage loop of the first converter gets affected. Fig. 1.5a represents this aspect by showing the reduction in the bandwidth of the voltage loop of a buck converter, while increasing the number paralleled converters. In this figure, just the magnitudes are shown. Fig. 1.5b shows the step response of bus voltage, under a change in the resistive load. As can be seen, the two-converter system bring with different dynamic performance with respect to the case of a single converter. This is because, the impedance seen from the terminal of a single buck converter—Z_L in Fig. 1.3—is just the load resistance. While, when two converters are in connected parallel, at the terminal of each converter, we see the load resistance in parallel with the output impedance of the other source converter. This situation can get even more critical in practical applications with a higher number of converters and more diverse topologies.

1.2.3 Frequently changing microgrids

Third example can be found in some environments with possibly frequent variations in the microgrid configuration, such as shipboard dc power distribution systems [37]. In this case, the behavior seen by a converter from its load-side and source-side can tremendously change along the ship's mission. A significant example for this aspect is the connection or disconnection of several pulse-load or pulse-sources that just occurs depending on the specific mission of the ship. This

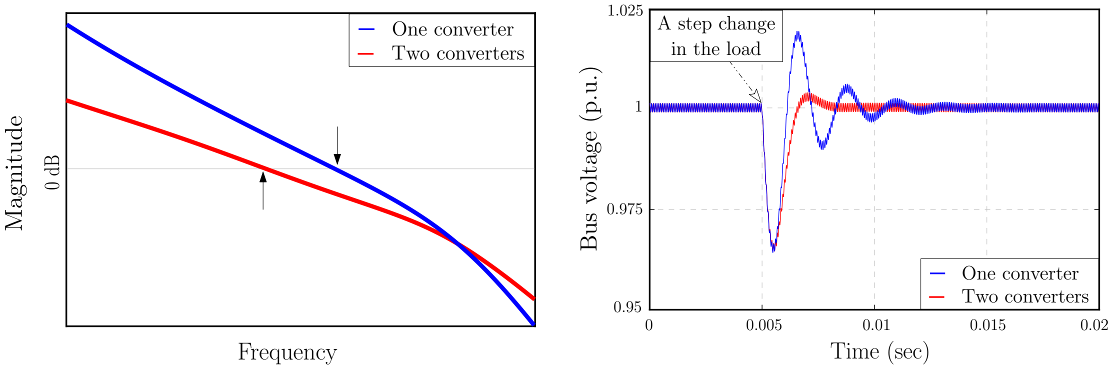

(a) Transfer functions (b) Step response

Fig. 1.5. Time- and frequency-domain behaviors of the voltage loop of a buck converter, under connection of either a single converter or two similar converters in parallel to the dc bus.

can, of course, lead to variations in Z_L, and therefore, in the dynamics performance of some control loops.

1.3 Existing works on stability monitoring and adaptive tuning

According to the motivation examples described above, it is important to perform continuous and online stability monitoring in the power converters operating in dc microgrids. The monitored data can be effectively exploited to tune the power converters controllers, thus ensuring a reliable operation of the microgrid. To this end, some small-signal modeling and linearization around the steady-state operating point of the switched mode power converters is required. The obtained small-signal models are usually valid at the frequency range of up to around half of the switching frequency [38]. This range, however, is much higher than the normal bandwidth of the power converters (i.e., in the range of one-tenth of the switching frequency [38, 39]), providing, thus, an accurate modeling of the system. The existing works on small-signal stability analysis and adaptive tuning of dc microgrid power converters can be mainly categorized in the following three groups: loop gain-based approach, state space-based approach, and impedance-based approach.

1.3.1 Loop gain-based methods

Measuring the loop gains of different converters within a microgrid is a common way to evaluate the control performances of several loops. The obtained frequency responses can provide us with stability information of a converter's control loops, which are also affected by the other interconnected converters. This can also give some impression about the overall system-level stability. However, the comprehensive methods for analyzing system-level stability are discussed in the next subsections.

So far, several investigations have been reporting the loop gain measurement, based on which the system stability margins can be evaluated. The existing methods are based on exciting the system either by the frequency sweep of a narrow-band signal, such as sine waves [40,41], or by a wide-band signal, such as impulse [42], or random signals [43–45]. The main advantage of wide-band perturbation is that, it can excite multiple frequency components at once, without needing the time consuming frequency sweep used in the narrow-band case. So, it significantly reduces the measurement time. The basis of loop gain injection and frequency

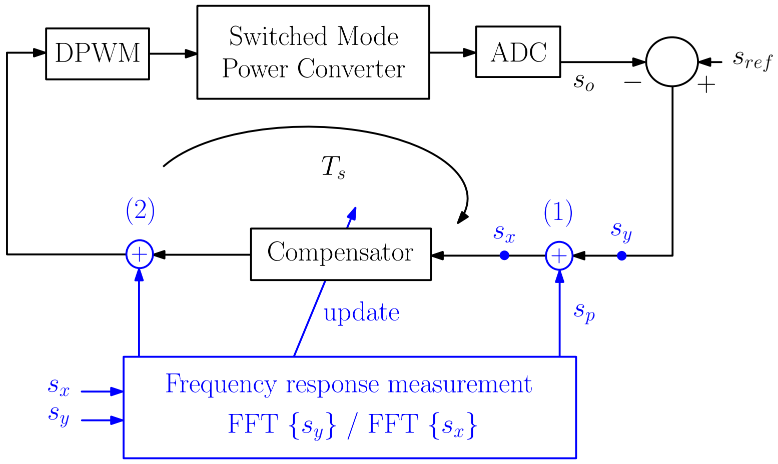

Fig. 1.6. Frequency response measurement of a generic control loop within SMPS, by injecting a perturbation signal s_p, either wide-band or narrow-band, either at point (1) or (2).

response measurement is shown in Fig. 1.6. As can be seen, a perturbation signal s_p is injected in a generic control loop T_s of the switched-mode power supplies (SMPS), during the normal closed-loop operation. Then, the frequency response of that loop can be found by evaluating the fast Fourier transform (FFT) of the signals right before s_y and right after s_x the injection point, and calculating their ratio. The injection can be inserted anywhere in the digital feedback loop, for instance, before or after the compensator. It is worth mentioning that, if instead of the whole loop T_s, just the control-to-output transfer function is desired (like what is done in [46]), then the concept is the same, just the points s_x and s_y will be defined in a different way. The obtained frequency responses can eventually be used to update the digital compensator of the loop under study, for achieving a desired behavior.

In [43], the system frequency response is calculated using a cross-correlation approach. In this method, a pseudo-random binary sequence (PRBS) is added to the duty cycle of a converter, or to the signal before the digital compensator. By assuming the converter as a linear time-invariant (LTI) system, the output voltage or current is measured. Then, the cross-correlation between the input and the output is found, and the impulse response of the system is calculated under the assumption that the PRBS signal is a good approximation of white-noise. Finally, by performing FFT, the frequency response of the system is found. Simplified versions of what mentioned above, can be found in [44, 45]. Two different dc distribution systems are considered in [37] and [46], in both of which, adaptive tuning of the power converters regulators is achieved by rapid PRBS-based identification of a generic control loop.

Recently, many other system identification approaches have been proposed for the stability analysis and adaptive tuning of power converters [40, 44, 47–50]. These approaches typically consider the system under study as either a black-box model [40, 44], or a gray-box model [49, 50]. Then, when the error between the real system behavior and the corresponding model behavior is minimized, an accurate model is deemed to have been obtained. The black-box model, also known as non-parametric system identification technique, features a low complexity level and does not require prior knowledge or estimations of the considered model. The drawbacks of this method are the need to long sequences of data to be acquired, slow response times, and inability in dealing with rapid system variations. On the other hand, the gray-box method, also known as parametric system identification technique, has a higher level of complexity, because the structure of the targeted model must be defined in advance. In particular, this methods are appropriate for SMPSs, due to the initial assumption of the dc-dc converter to behave as a second order system. However, all the system identification methods are applied when the system is operating in steady-state; consequently, a new model of the system must be identified in case of any variations in the steady-state operating condition.

Middlebrook's analog injection technique [51] is the basis of some other studies. It is the case of [52], which reports the application of the online measurement of crossover frequency and phase margin in digitally controlled SMPSs during normal operating conditions. A digital small-signal perturbation is added in series with the converters control loop, and the injection frequency is adjusted till reaching a frequency at which, the unity loop gain is observed, that is the crossover frequency. At this frequency, the phase margin is evaluated and monitored as a measure of the stability of system. This method is verified referring buck and boost converters, showing its ability to continuously estimate the crossover frequency and the phase margin without opening the feedback loop, and even in presence of load transients [52].

1.3.2 State space-based methods

This method usually considers a general state matrix for the entire system consisting of all the state variables of all the system components [53, 54]. Not only the internal stability of each converter can be analyzed based on a state-space model, but also, the overall system-level stability of the whole microgrid can be studied by including the state variables from all the converters [55]. This approach, however, requires a lot of information about the system, which, in real scenarios is not always feasible.

1.3.3 Impedance-based methods

In some cases, the loop gain-based methods might not provide all the required information about the microgrid-level stability, requiring thus, to measure more than one control loop. On the other hand, the high-level state-space models require a lot of data about the system, which is not always suitable, especially, when dealing with online stability monitoring and tuning tasks. In this subsection, an alternative system-level stability method is described, to directly judge the stability of a system, based on the terminal characteristics of different subsystems. To this end, a multi-converter system can be divided into a source-side subsystem and a load-side subsystem, as shown in Fig. 1.7. Then, the Nyquist criterion is applied to the ratio between source subsystem impedance (shown as Z_S in Fig. 1.7) and load subsystem impedance (shown as Z_L in Fig. 1.7), that is also called as minor loop gain (Z_S/Z_L). Investigating the interaction stability based on minor loop gain was proposed by Middlebrook in [34]. Since then, many studies have been following the same principle [56–59]. Still based on minor loop gain, some studies have proposed less conservative stability criteria [35, 60]. The impedance-based method is shown to be an effective tool for small-signal stability analysis, since it features the property of modularity by dividing the whole interconnected system into source and load subsystems. Besides, all the physical components and

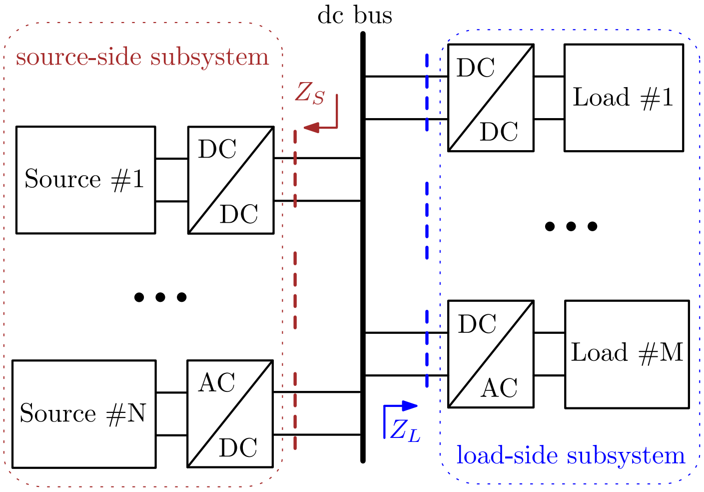

Fig. 1.7. Dividing a dc microgrid with N generic sources and M generic loads into the source-side and the load-side subsystems, and modeling each subsystem through its equivalent impedance.

control parts of the power converter are intrinsically considered in the measured impedances. So, both source and load subsystems can be regarded as “black boxes”, thus, eliminating the need to prior knowledge about their internal structures and parameters.

To come up with some limitations in the impedance-based stability analysis, such as sensitivity to the component grouping and power flow direction [61], the passivity-based stability criterion (PBSC) is proposed in the literature [62]. This criterion, together with the allowable impedance region (AIR) [63], detects the stability of a power converter system by only looking at the dc bus impedance. The dc bus impedance —defined as the parallel combination of the source subsystem impedance and the load subsystem impedance— has been shown to provide a measure of the dc microgrid stability and performance. Novel bus impedance-based stability analysis and stabilization techniques are proposed in some works, such as [32, 64].

1.4 Disseration outline and summary of contributions

Chapter 2 presents an on-line approach to evaluate and monitor the stability margins of dc microgrid power converters. The discussed online monitoring technique (MT) is based on the Middlebrook’s loop-gain measurement technique, adapted to the digitally controlled power converters. In this approach, a perturbation is injected into a specific control loop of the converter and after measuring the loop gain, its crossover frequency and phase margin are continuously evaluated and monitored. This technique follows the same concept as [52], but, it considers a different application (i.e., dc microgrid power converters), based on which, a different signal processing is proposed. The complete analytical derivation of the model, as well as detailed design aspects, are reported. In addition, the presence of multiple power converters connected to the same dc bus, all having the stability monitoring unit, is also investigated. The proposed technique can be extended to all the control loops within dc microgrid power converters, has a low implementation complexity, is robust to noise, and is compatible with the digital control platform of the DER converters, thus, it does not need an auxiliary processor for the signal processing part. The core idea of this work is used by some monitoring and tuning works that are recently published [65, 66].

Chapter 3 uses the basic concepts described in Chapter 2 for further correction and tuning tasks in dc microgrid power converters. In particular, two possible tuning techniques are addressed and discussed. Both techniques are based on injecting a small-signal sinusoidal perturbation, at the desired crossover frequency, into a generic control loop of power converters. The signals right before, and right after the injection point are then processed and, subsequently, some error vectors are defined. Finally, the regulator parameters are tuned to make the error signal converge to zero, allowing, thus, to reach the desired phase margin and crossover frequency. These tuning techniques are based on a similar concept as those used in [67, 68], with two major differences: the application, which herein, is for dc microgrid power converters, and the signal processing algorithm. In addition, this work takes account for the situation in which an unfeasible phase margin is desired. This case can happen when the applied regulator provides its maximum allowable phase to compensate a generic control loop, at the reference crossover frequency; but, still the phase margin of that loop is less than the desired reference phase margin.

Chapter 4 discusses the application of wide-band methods in online identification of different control loops. This can be necessary for some scenarios, in which, the crossover frequency and the phase margin are not enough to understand the entire control performance of dc microgrid power converters, and we need to monitor the loop gain over its whole bandwidth. In particular, PRBS signals are exploited, because of the short time required for identification, the possibility of adjusting the injection bandwidths, the easy generation algorithm based on feedback shift registers, the low peak factor due to the binary nature, and most importantly, the possibility to generate several PRBSs that each have different frequency components, i.e., they are orthogonal. In this context, Chapter 4 proposes the injection of multiple orthogonal PRBSs into different control loops of a power converter, at the same time. This is the extension of what is described in [37,46], from a single-loop identification to the simultaneous identification of multiple loops within dc microgrid power converters.

Chapter 5 provides a more general and system-level stability evaluation method for the dc microgrid, which is based on the dc bus impedance. In particular, this chapter firstly, represents the bus impedance in terms of voltage (or droop) loop gain of the source-side converter. Secondly, it provides an estimation for the peak value of bus impedance based on the phase margin. Thirdly, it proposes to continuously monitor the peak value of bus impedance by applying the loop injection technique described in Chapter 2 to the voltage (or droop) loop. The monitored value can then be used to autotune the voltage regulator, in order to keep the bus impedance in a well-known allowable impedance region. This, not only ensures the stability, but also provides the desired dynamic performance for the whole interconnected system. With respect to the similar bus impedance damping methods [32], this work requires low signal processing effort, is robust to noise and perturbations coming from the other converters connected to the common dc bus, and eliminates the need for time consuming and memory intensive impedance measurement tasks.

Finally, some conclusions and possible future extensions of this work are given in the last chapter.

In brief, the main contributions of this work are as follows:

- An online stability monitoring approach is proposed for dc microgrid power converters, that is able to continuously monitor the stability margins of a generic control loop. Based on the same concepts used for the online monitoring, two different autotuning schemes are discussed, aiming to maintain a certain dynamic performance for a loop regardless the possible variations in the microgrid operation.
- For the cases in which, a full picture of the control performance of several loops is needed, the above-mentioned monitoring of the stability margins might not be enough. In thi context, multiple orthogonal PRBSs are proposed to be simultaneously injected in several control loops, in order to identify multiple loop gains in one measurement cycle.
- In order to assess the microgrid-level stability and dynamic performance, some monitored loop gains are effectively used to estimate the dc bus impedance, which has been shown to reflect the dynamic stability of an interconnected system.

Following publications have been achieved as the the partial results of this thesis:

∗ Journal papers
  - A. Khodamoradi, G. Liu, P. Mattavelli, T. Caldognetto, P. Magnone, ‘Analysis of an On-Line Stability Monitoring Approach for DC Microgrid Power Converters’, IEEE Transactions on Power Electronics (2018).
  - A. Khodamoradi, G. Liu, P. Mattavelli, T. Messo, ‘Simultaneous Identification of Multiple Control Loops in DC Microgrid Power Converters’, IEEE Transaction on Industrial Electronics (2019).
  - Q. Xiao, P. Mattavelli, A. Khodamoradi, A., ‘DQ Impedance Analysis for Stability Assessment in Complex Converter Networks’, CES Transaction on Electrical Machines and Systems (2019).

  - A. Khodamoradi, H. Abdollahi, E. Santi, P. Mattavelli, ‘A Loop Gain-Based Technique for Online Bus Impedance Estimation and Damping in DC Microgrids’, under review of IEEE Transaction on Power Electronics.
  - A. Khodamoradi, G. Liu, P. Mattavelli, T. Messo, H. Abedini, ‘PRBS-based Loop Gain Identification and Output Impedance Shaping in DC Microgrid Power Converters’, under review of MATCOM special issue (2019), Transactions of IMACS.
  - Q. Xiao, P. Mattavelli, A. Khodamoradi, ‘Modelling and Analysis of Equivalent SISO D-Q Impedance of Grid-Connected Converters’, under review of MATCOM special issue (2019), Transactions of IMACS.

∗ Conference papers

  - H. Abdollahi, A. Khodamoradi, E. Santi, P. Mattavelli, ‘Online Bus Impedance Estimation and Stabilization of DC Power Distribution Systems: a Method Based on Source Converter Loop-Gain Measurement’, 2020 IEEE Applied Power Electronics Conference and Exposition (APEC 2020).
  - A. Khodamoradi, G. Liu, P. Mattavelli, ‘Auto-tuning of DC Microgrid Power Converters Based on a Constant Frequency Injection’, IEEE 21st Conference on power electronics and applications (EPE’ 2019).
  - F. Cavazzana, A. Khodamoradi, H. Abedini, P. Mattavelli, ‘Analysis of an Impedance Modeling Approach for Droop-Controlled Inverters in System DQ Frame’, 11th Annual IEEE Energy Conversion Congress and Exposition (ECCE 2019).
  - A. Khodamoradi, P. Mattavelli, F. Cavazzana, ‘Effect of Torsional Interactions on the Output Impedance of PMSG-Based Wind Turbines’, IEEE 20th Conference on power electronics and applications (EPE’ 2018).
  - G. Liu, A. Khodamoradi, P. Mattavelli, T. Caldognetto, P. Magnone, ‘Plug and Play DC-DC Converters for Smart DC Nanogrids with Advanced Control Ancilary Services’, 2018 IEEE International Workshop on Computer Aided Modeling and Design of Communication Links and Networks (CAMAD).
  - A. Khodamoradi, G. Liu, P. Mattavelli, T. Caldognetto, P. Magnone, ‘On-line Stability Monitoring for Power Converters in DC Microgrids’, 2017 IEEE Second International Conference on DC Microgrids (ICDCM).

Chapter 2

Online stability monitoring of DC microgrid power converters

2.1 Introduction

As discussed in the previous chapter, continuous and online stability monitoring of different control loops within dc microgrid power converters is an important task, that can also be exploited in further correction and tuning actions.

Evaluating the entire frequency response of different control loops is addressed in several works [40, 42–44, 47, 48, 69, 70]. To this end, the system is usually excited either by the frequency sweep of a narrow-band signal, such as sine waves [40], or by a wide-band signal, such as impulse [42], or random signals [43, 44]. Then, by measuring the input and output of each loop, performing FFT, and then calculating the ratio, the desired loop gain is evaluated. Based on the obtained loop gains, the stability and control performance of different loops can be studied. This methods, however, need time and space consuming measurements. Also, an auxiliary processor is required to perform the signal processing part, requiring also a communication interface.

On the other hand, some other approaches do not need the entire loop gain measurement and just focus on the frequency at which the loop gain crosses 0 dB, i.e., crossover frequency. These methods [52] are based on the Middlebrook's analog injection technique [51]. A digital small-signal perturbation is added in series with the converters control loop, and the injection frequency is adjusted till reaching a frequency at which, the unity loop gain is observed, that is the crossover frequency. At this frequency, the phase margin is evaluated and monitored as a measure of the stability of system. This method is verified referring buck and boost converters, showing its ability to continuously estimate the crossover frequency and the phase margin without opening the feedback loop, and even in presence of load transients [52].

On the basis of the same concept discussed in [52], this work proposes a stability monitoring technique for the parallel operation of multiple converters, which becomes, in recent years, an aspect of interest in microgrid applications. An alternative signal processing, with low implementation complexity, is proposed in this work. In addition, the situation of having multiple converters simultaneously performing the stability monitoring. This is a typical issue in microgrids when two or more converters inject a small-signal perturbation at the same time, with frequencies that can be close to each other. In general, the effects of different perturbation signals can get combined, leading to an error in the process of tracking the unity loop-gain frequency. To address this issue, a prioritization-based technique is considered, such that, just one converter is allowed to inject the small-signal perturbation at a certain time. For more critical cases, where simultaneous monitoring is required in several converters, it is shown that a small modification in the way the unity-gain frequency is extracted allows to minimize the error resulted from the combination of the perturbation signals. To summarize, the proposed monitoring technique is robust to noise and the perturbations coming from other converters connected in parallel to the common dc bus. Moreover, since it has a low implementation complexity and fast response time, it can be useful for future investigations on adaptive tuning techniques.

The remainder of this Chapter is arranged as follows. Section 2.2 briefly explains the concept of loop gain injection under normal closed-loop operation of a generic control loop. Section 2.3 provides details of the proposed estimation technique to find the crossover frequency and the phase margin. The small-signal derivations, and some design aspects are therein discussed. Section 2.4 presents the situation in which multiple power converters simultaneously performing the proposed stability monitoring. Section 2.5 considers a generic dc microgrid power converter, to which, the proposed monitoring tool is applied. Section 2.6 describes a laboratory dc microgrid setup and presents experimental validations of the technique.

2.2 Concept description

Middlebrook's injection technique [51] is well known and widely used to measure the frequency response of an analog system control loop without interrupting the feedback path. The technique consists in injecting a small-signal perturbation at a certain frequency into the considered control loop in order to stimulate and acquire the system behavior at that frequency. The stability monitoring technique presented herein is based on the same concept, but applied to digitally-controlled converters. Digital control platforms are usually preferable over the analog counterpart in several environments, including the microgrid one [71]. This is because the digital approach features programmability, reduced need to external passive components, high integration capability, and the intrinsic ability to implement complex functions, which is a crucial aspect for stability monitoring, auto-tuning, and other similar tasks [39].

Fig. 2.1 schematically represents the proposed monitoring technique applied to a generic control loop of a digitally controlled power converter. Regardless of the specific loop (e.g., current, voltage, or power control loop), the main components of a digital controller implementation are reported in Fig. 2.1, including, in particular, an analog-to-digital converter (ADC), a discrete-time compensator, and a digital

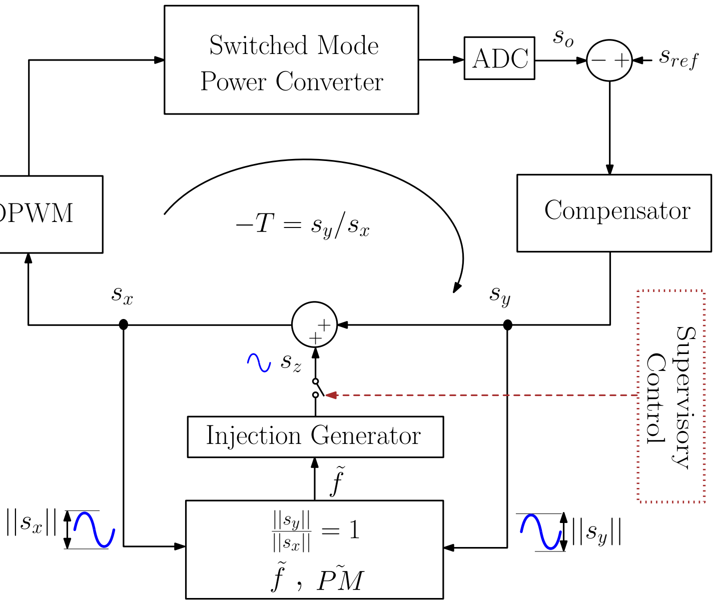

Fig. 2.1. Stability monitoring of a generic control loop within DER converters.

pulse width modulator (DPWM). The perturbation signal s_z, with frequency $\tilde{f}$, can be injected ideally at any point of the digital control loop. Notably, the digital implementation is free from any loading effect, which is an advantage over the analog case.

By referring to Fig. 2.1, the system loop gain evaluated at $\tilde{f}$ is:

$$T(s)|_{s=j2\pi\tilde{f}} = -\left.\frac{s_y(s)}{s_x(s)}\right|_{s=j2\pi\tilde{f}} = -\frac{s_y(j\,2\pi\tilde{f})}{s_x(j\,2\pi\tilde{f})} \tag{2.1}$$

where s_x and s_y are the signals after and before, respectively, the perturbation injection point. By definition, the crossover frequency f_c of the control loop corresponds to the frequency $\tilde{f}$ of the perturbation signal at which the open-loop transfer function shows unity gain; that is, if:

$$|T(j\,2\pi\tilde{f})| = 1 \tag{2.2}$$

then:

$$f_c = \tilde{f} \tag{2.3}$$

and:

$$PM = \tilde{PM} = 180 + \angle T(j\,2\pi\tilde{f}) \ = \angle s_y(j\,2\pi\tilde{f}) - \angle s_x(j\,2\pi\tilde{f}) \tag{2.4}$$

where PM and $\tilde{PM}$ indicate, respectively, the true and the estimated values of the phase margin. It is worth to remark that this approach is valid for systems with a loop gain higher than unity (i.e., $|T(j2\pi f)| > 1$) for some frequencies, which is almost always the case; otherwise, the stability margin cannot be assessed in this way, because there are no zero-crossings.

On the basis of this, the operation principle of the proposed crossover frequency and phase-margin estimation technique is to adjust the frequency $\tilde{f}$ of the injected perturbation s_z so as to have the amplitude difference between the two signals s_x and s_y converging to zero. In such an operating point (i.e., $|s_y| - |s_x| = 0$), (2.2)-(2.4) hold, therefore, the frequency $\tilde{f}$ and the phase shift between s_x and s_y are monitored and referred to as the crossover frequency and the phase margin of the considered control loop, respectively.

It is worth remarking that the small-signal perturbation can be injected in any control loop of the power converter, as far as that loop is stable—even with low stability margins. The information obtained by the monitoring process may eventually be exploited to perform provisions that keep the loop under investigation far from instability (e.g., by auto-tuning the associated regulators).

2.3 Proposed estimation technique

2.3.1 Proposed phase margin and crossover frequency estimator

Fig. 2.2 displays the technique that is here proposed for the estimation of the crossover frequency and phase margin of a control loop [72, 73]. First of all, a sine wave generator is used to produce a small-signal perturbation s_z of amplitude $|s_z|$ and frequency $\tilde{f}$. The signal s_z is injected into the control loop, resulting in a perturbation at the same frequency in the signals s_x and s_y. Similarly to common and well-known projections used in signal processing (e.g., to find the Fourier series of a signal), the two signals s_x and s_y are multiplied by sine and cosine terms at the estimated crossover frequency $\tilde{f}$. By doing so, it is possible to derive the signal projections into a common reference frame defined by the in-phase (i.e., sin) and the quadrature (i.e., cos) components of the injected perturbation s_z. The obtained projections can be represented in any two-dimensional reference plain, like, for example, the complex plane. Herein, the components of s_x and s_y

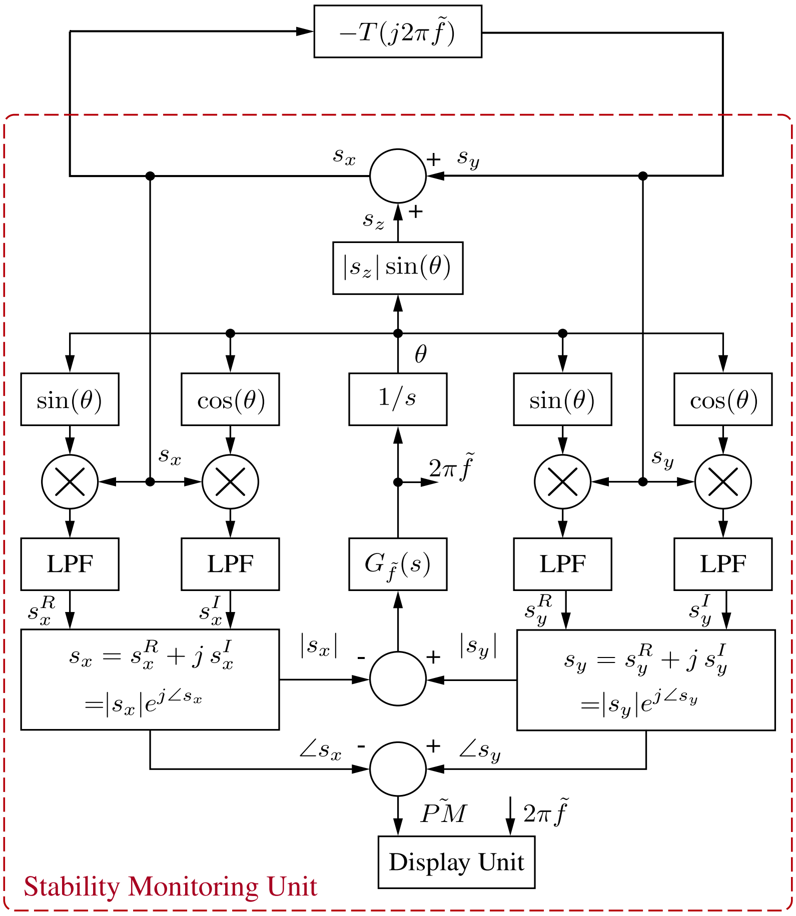

Fig. 2.2. Scheme of the proposed online stability monitoring technique.

at frequency $\tilde{f}$ are represented by a real and an imaginary part as $s_x^R + js_x^I$ and $s_y^R + js_y^I$.

To describe this process analytically, let us assume a linear and time-invariant (LTI) system. The effect of the perturbation s_z in a specific loop, can be represented as a sinusoidal signal at $\tilde{f}$, with a certain magnitude and phase:

$$s_x = |s_x|\cos(2\pi\tilde{f}t + \angle s_x), \quad s_y = |s_y|\cos(2\pi\tilde{f}t + \angle s_y) \tag{2.5}$$

By projecting s_x along the real and the imaginary axes we get:

$$s_x(t)\sin(2\pi\tilde{f}t) = -\frac{|s_x|}{2}\sin(\angle s_x) + \frac{|s_x|}{2}\sin(4\pi\tilde{f}t + \angle s_x) \tag{2.6}$$

$$s_x(t)\cos(2\pi\tilde{f}t) = \frac{|s_x|}{2}\cos(\angle s_x) + \frac{|s_x|}{2}\cos(4\pi\tilde{f}t + \angle s_x) \tag{2.7}$$

The same holds for s_y. The dc values of the results in (2.6) and (2.7) are, respectively, the imaginary and the real components of the signal s_x at $\tilde{f}$ (the same applies for s_y). In Fig. 2.2 the dc values are estimated by low-pass filters (LPFs) with transfer function $G_{LPF}(s)$.

Equations (2.6) and (2.7) after low-pass filtering can be written as:

$$LPF\left(s_x(t)\sin(2\pi\tilde{f}t)\right) = -\frac{|s_x|}{2}\sin(\angle s_x) + G_{LPF}(j4\pi\tilde{f}).\frac{|s_x|}{2}\sin(4\pi\tilde{f}t + \angle s_x) \tag{2.8}$$

$$LPF\left(s_x(t)\cos(2\pi\tilde{f}t)\right) = \frac{|s_x|}{2}\cos(\angle s_x) + G_{LPF}(j4\pi\tilde{f}).\frac{|s_x|}{2}\cos(4\pi\tilde{f}t + \angle s_x) \tag{2.9}$$

If the cut-off frequency of the LPFs f_{lpf} is significantly smaller than $\tilde{f}$, the gain of the LPF at twice the estimated crossover frequency, namely, $|G_{LPF}(j4\pi\tilde{f})|$, is small, and the high frequency components in (2.8) and (2.9) can be neglected. This means that (2.8) and (2.9) can precisely estimate $s_x^I = -\frac{|s_x|}{2}\sin(\angle s_x)$ and $s_x^R = \frac{|s_x|}{2}\cos(\angle s_x)$, respectively. Then, the obtained imaginary and real components can be used to evaluate the magnitude and phase of s_x and s_y, by using the arc tangent and square-root functions. Therefore, based on estimating the quantities $|s_x|$, $|s_y|$, $\angle s_x$, and $\angle s_y$, an accurate estimation of the phase margin and crossover frequency can be reached. The particular choice of f_{lpf} has an effect on the estimated stability margins, which is shown in Section 2.6 by means of numerical data. In general terms, according to (2.8) and (2.9), f_{lpf} should be significantly smaller than the crossover frequency, but it should not be so small to affect the design of the frequency loop regulator $G_{\tilde{f}}$, as explained later in this section.

The difference in amplitudes $|s_y| - |s_x|$ is processed by the frequency regulator $G_{\tilde{f}}$ in Fig. 2.2, whose output is the frequency of the perturbation signal. By including an integral part in $G_{\tilde{f}}$, the difference in the amplitudes converges to zero (i.e., $|s_x| = |s_y|$), because of the unity loop gain condition discussed in Section 2.2. At this point, the frequency of the perturbation signal is equal to the crossover frequency of the considered loop, while the phase margin is calculated as the phase shift between $s_x(j2\pi\tilde{f})$ and $s_y(j2\pi\tilde{f})$.

Finally, it is worth remarking that the signal processing of the proposed scheme shown in Fig. 2.2 can be also implemented in other ways, such as the one based on band-pass filters (BPF) adopted in [52]. However, this choice would require a BPF implementation that automatically adapts its center frequency, bandwidth, and Q-factor according to the loop under investigation, resulting in an increase in the response time and computational burden, which may be critical.

2.3.2 Design of the frequency loop regulator $G_{\tilde{f}}$

The regulator $G_{\tilde{f}}$ performs the regulation of the perturbation frequency $\tilde{f}$ on the basis of the measured difference in the amplitude of the two signals s_x and s_y (i.e., $|s_y| - |s_x|$). A model of this frequency control loop is therefore required for the design of $G_{\tilde{f}}$. However, due to system non-linearities, a general and rigorous analytical procedure for modeling this loop is not trivial and would require dedicated investigations. Instead, in the following, two simplifying assumptions are introduced, which allow to approximate the frequency loop model and design the regulator $G_{\tilde{f}}$.

Assumption 1

The dynamics of the frequency control loop is mostly determined by the LPFs used in the MT described in Fig. 2.2. As explained in Section 2.3-A, the cut-off frequency of the LPFs f_{lpf} must be significantly smaller than $\tilde{f}$ to have a precise amplitude estimation. Based on this condition and the fact that the rest of the MT process is much faster than the low-pass filtering part, assumption 1 represents a reasonable approximation of the system dynamics. Under assumption 1, the open-loop transfer function from the injection frequency $\tilde{f}$ to the amplitude difference $|s_y| - |s_x|$ can be approximated as:

$$T_{\tilde{f}}(s) = \frac{[|s_y| - |s_x|](s)}{\tilde{f}(s)} \simeq K_{\tilde{f}} \cdot G_{LPF}(s) \tag{2.10}$$

where $K_{\tilde{f}}$ is the static gain:

$$K_{\tilde{f}} = \left.\frac{\partial\left[|s_y(j2\pi f)| - |s_x(j2\pi f)|\right]}{\partial f}\right|_{f=\tilde{f}} \tag{2.11}$$

By referring to Fig 2.2, it is possible to notice that:

$$s_x(j2\pi f) = \frac{1}{1+T(j2\pi f)} s_z(j2\pi f) \tag{2.12}$$

$$s_y(j2\pi f) = -\frac{T(j2\pi f)}{1+T(j2\pi f)} s_z(j2\pi f) \tag{2.13}$$

Therefore, substituting (2.12) and (2.13) in (2.11), and assuming s_z generated with constant amplitude $|s_z|$, the value of $K_{\tilde{f}}$ can be expressed as:

$$K_{\tilde{f}} = \left.\frac{\partial\left[|s_y(j2\pi f)| - |s_x(j2\pi f)|\right]}{\partial f}\right|_{f=\tilde{f}} = |s_z| \left.\frac{\partial}{\partial f}\left(\frac{|T(j2\pi f)|-1}{|1+T(j2\pi f)|}\right)\right|_{f=\tilde{f}} \tag{2.14}$$

According to the basic differentiation identities for the derivative of a generic rational expression, and based on the fact that $|T(j2\pi\tilde{f})|\Big|_{f=\tilde{f}} \simeq 1$, (2.14) can be written as follows:

$$\begin{aligned} K_{\tilde{f}} &= |s_z| \left.\frac{|1+T(j2\pi f)|\cdot\frac{\partial|T(j2\pi f)|}{\partial f}}{|1+T(j2\pi f)|^2}\right|_{f=\tilde{f}} - |s_z| \left.\frac{(|T(j2\pi f)|-1)\cdot\frac{\partial|1+T(j2\pi f)|}{\partial f}}{|1+T(j2\pi f)|^2}\right|_{f=\tilde{f}} \\ &= |s_z| \left.\frac{\frac{\partial|T(j2\pi f)|}{\partial f}}{|1+T(j2\pi f)|}\right|_{f=\tilde{f}} \end{aligned} \tag{2.15}$$

which, based on the Euler's formula, can be simplified as follows (again using $|T(j2\pi\tilde{f})|\Big|_{f=\tilde{f}} \simeq 1$):

$$K_{\tilde{f}} = |s_z| \left.\frac{\frac{\partial|T(j2\pi f)|}{\partial f}}{\sqrt{2}\sqrt{1+\cos(\angle T(j2\pi f))}}\right|_{f=\tilde{f}} \tag{2.16}$$

In the case that the loop gain T is not known a priori, suitable approximation or estimations around the crossover frequency may be considered, like the assumption introduced below.

Assumption 2

The slope of $|T(j2\pi f)|$ and the phase of T around the crossover frequency (i.e., $\left.\frac{\partial|T(j2\pi f)|}{\partial f}\right|_{f=\tilde{f}}$, and $\angle T(j2\pi f)|_{f=\tilde{f}}$) are -20 dB/decade and 90 deg, respectively. These two estimations of the system behavior are considered to give a reasonable approximation of a second order stable system and do not have general validity. For example, if the approximated phase of T around the crossover frequency is assumed to be 60 deg instead 90 deg, based on (2.16), a difference of about 10% in the estimation of $K_{\tilde{f}}$ can be expected.

Different choices are possible to implement $G_{\tilde{f}}$, herein a pure integrator is considered and designed on the basis of the desired bandwidth of the frequency control loop $f_{c,\tilde{f}}$:

$$G_{\tilde{f}}(s) = \frac{2\pi f_{c,\tilde{f}}}{K_{\tilde{f}}}.\frac{1}{s} \tag{2.17}$$

giving a theoretic value of phase margin equal to $\pi/2+\text{phase}[\text{LPF}(j2\pi f_{c,\tilde{f}})]$, which results in generous margins in case $f_{c,\tilde{f}}$ is significantly lower than the cut-off frequency f_{lpf} of the low-pass filters. This design is actually a conservative option. Of course, if required, $f_{c,\tilde{f}}$ can be further increased; in this case, the phase margin of the MT loop should be evaluated and taken into account.

Finally, it is worth remarking that the response time of the proposed MT depends on the regulator $G_{\tilde{f}}$, which, in turn, depends on the actual system parameters (i.e., T). However, the stability of the MT can be ensured by choosing sufficiently wide stability margins for the frequency control loop. For validation purposes, the considered model has been evaluated in simulation considering a buck converter with the parameters listed in Section 2.6. A unitary step change has been applied to the injected perturbation frequency $\tilde{f}$ and the open loop step response of the amplitude difference $|s_y|-|s_x|$ has been observed. In these conditions, the variation in the value of $|s_y| - |s_x|$ presents about 5% error with respect to the estimated static gain $K_{\tilde{f}}$. Also, the observed rise-time matches, with a similar precision, the set value of bandwidth $f_{c,\tilde{f}}$. In the light of this the design of the regulators used in the experimental setup in Section 2.6 is performed.

2.3.3 Gain margin monitoring

The approach proposed in Fig. 2.2 to monitor the 0 dB crossover frequency f_c and the phase margin PM, can be easily extended to also monitor the gain margin. This extension shows merit in some control loops that might have a high phase

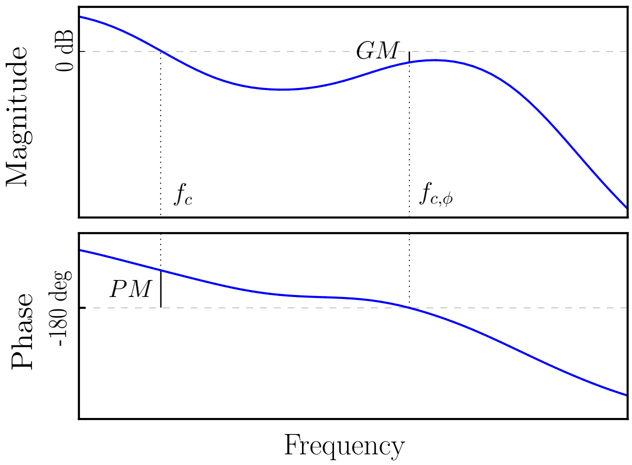

Fig. 2.3. A generic control loop with high phase margin and low gain margin.

margin, while the gain margin is poor, as demonstrated in Fig. 2.3. In this case, the phase margin monitoring is not enough, and the gain margin is also necessary to conduct a better stability assessment.

In order to monitor the gain margin, an additional regulator ($G_{\tilde{f}_\phi}$) must be added to the scheme presented in Fig. 2.2, whose input is the phase shift between s_x and s_y, i.e., $\angle s_x - \angle s_y$. The output of $G_{\tilde{f}_\phi}$ is the estimated 180 deg crossover frequency $\tilde{f}_\phi$. Design of $G_{\tilde{f}_\phi}$ follows the same logic presented above for the design of $G_{\tilde{f}}$. Thus, the injection signal s_z should be sum of two frequency components: $\tilde{f}$, and $\tilde{f}_\phi$. The injection frequency $\tilde{f}_\phi$, corresponds with the 180 deg crossover frequency $f_{c,\phi}$, if $\angle T(j\,2\pi\tilde{f}_\phi) = -180$. So, when:

$$\angle s_x(j\,2\pi\tilde{f}_\phi) = \angle s_y(j\,2\pi\tilde{f}_\phi), \tag{2.18}$$

then:

$$f_{c,\phi} = \tilde{f}_\phi \tag{2.19}$$

and

$$GM = \tilde{GM} = |T(j\,2\pi\tilde{f}_\phi)| = |\frac{s_y(j\,2\pi\tilde{f}_\phi)}{s_x(j\,2\pi\tilde{f}_\phi)}| \tag{2.20}$$

where GM and $\tilde{GM}$ indicate, respectively, the true, and the estimated value of gain margin.

2.3.4 Perturbation amplitude

As mentioned in Section 2.3, the choice of the small-signal perturbation amplitude $|s_z|$ does not affect the design of the frequency loop in Fig. 2.2. However, in order to maintain the effectiveness of the method $|s_z|$ should be chosen appropriately. In particular, the following aspects should be considered:

- Effect of the small-signal perturbation on the output signals. To evaluate this issue, we look at the effect of the perturbation on the bus voltage and the inductor current, because these signals are relevant to the loops considered in this work. Of course, in the case of having a power loop, the similar consideration can be made for the output power signal. Let us denote the effect of s_z on the bus voltage as s_{zv} and its effect on the inductor current as s_{zi}. Then, in the Laplace domain:

  $$s_{zv}(s) = G_{zv}(s)s_z(s), \quad s_{zi}(s) = G_{zi}(s)s_z(s) \tag{2.21}$$

  where $G_{zv}(s)$ is the transfer function from the perturbation signal to the bus voltage and $G_{zi}(s)$ is the transfer function from the perturbation signal to the inductor current. Then:

  $$G_{zv}(s) = \frac{v_{bus}(s)}{s_z(s)} = \frac{v_{bus}(s)}{s_x(s)}.\frac{s_x(s)}{s_z(s)} = \frac{G_{xv}(s)}{1+T(s)} \tag{2.22}$$

  where $T(s)$ is the open loop transfer function of the considered loop and $G_{xv}(s)$ is the transfer function from the perturbation point to the bus voltage, which can be analytically derived. The same process can be used to find $G_{zi}(s)$, too.

  For any system under study, $|s_z|$ must be large enough to obtain:

  $$|G_{zv}(\tilde{f})|.|s_z| \gg s_{nv}, \quad |G_{zi}(\tilde{f})|.|s_z| \gg s_{ni} \tag{2.23}$$

  where s_{nv} and s_{ni} are the noise levels on the bus voltage and on the inductor current, respectively. In this way, the minimum value of the perturbation amplitude is determined. For what concerns the maximum value, $|s_z|$ should be small enough to be considered as a small-signal value, so that the perturbation signal does not deteriorate the output signals.

- Effect of the small-signal perturbation on the dynamics of the frequency loop. The steady-state result of the frequency estimator does not depend on $|s_z|$, but its dynamics does (as shown in (2.14), (2.15), (2.16)).

2.4 Multiple converter scenario

When multiple, independent, paralleled converters with similar crossover frequencies perform stability monitoring at the same time, the injected perturbation signals combine and the accuracy of the unity-gain criterion (2.2) and (2.3) may reduce. Different solutions have been proposed to cope with similar issues [74,75]. The following paragraphs discuss this aspect, presenting a general approach, based on supervisory control, and a practical method for handling the issue in some cases of interest.

2.4.1 Non-simultaneous monitoring

In many practical applications, *simultaneous* stability monitoring is not strictly required. In these cases, different time slots for perturbation injection can be assigned to the converters and the stability monitoring in the converters activated sequentially without overlaps. The activation scheme can be defined, for example, by time division multiplexing algorithms, inspired by the telecommunication engineering solutions used in multi-antenna systems [76]. Here a supervisory control is adopted, which can be implemented in many ways, such as, the token ring technology [77]. In this way, a supervisory unit (as displayed in Fig. 2.1) issues an activation command to the converters for enabling the monitoring unit. The activation command is sequentially assigned to the converters according to predetermined criteria, such that they can activate their MT without overlaps in their monitoring times. Clearly, the rate at which the token is reassigned determines the time of convergence, which is an important aspect when the information provided by the monitoring tool is employed for controllers tuning.

2.4.2 Simultaneous monitoring

In less common but still realistic scenarios, the simultaneous stability monitoring of multiple converters is required. A relevant example can be the connection of additional converters to a distribution bus, which changes the bus impedance and so the stability margins of the other converters that may be initially connected. In this case, each converter must monitor its stability margins on-line, to make sure that the applied changes do not create additional instability issues. By referring to the proposed scheme discussed in the previous section, the simultaneous monitoring of stability margins at more than one converter is addressed below. For simplicity, in this part of the analysis a two-converter system is referred to; but

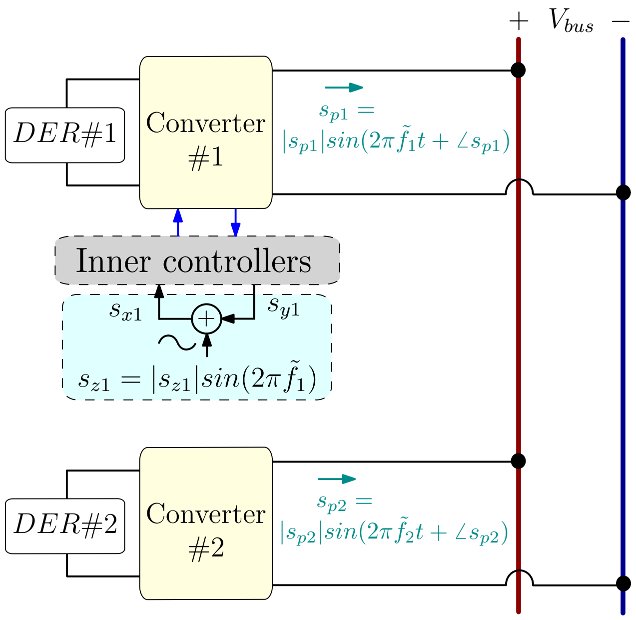

Fig. 2.4. Parallel connection of two DER converters to the dc bus, both equipped with the proposed MT. The small-signal perturbations s_{p1}, s_{p2} can also have similar frequencies.

the same discussion can be made also for systems with more converters. Fig. 2.4 represents this aspect by showing two converters, each injecting sinusoidal perturbations on the dc bus. In this case, we firstly observe that s_y in (2.5) can be modified in the following form (the same holds for s_x):

$$s_y = |s_{y1}|\cos(2\pi\tilde{f}_1 t + \angle s_{y1}) + |s_{y2}|\cos(2\pi\tilde{f}_2 t + \angle s_{y2}) \tag{2.24}$$

where subscript 1 refers to the first converter and subscript 2 refers to the second one. Based on the projection technique detailed in Fig. 2.2, the translation of each signal s_x, s_y along the sine term (or cosine term, similarly) of the estimated crossover frequency $\tilde{f}$ of each converter can be formulated. At converter #1, by exploiting the well-known trigonometric identities, it yields:

$$\begin{aligned} s_y(t)\sin(2\pi\tilde{f}_1 t) &= \{|s_{y1}|\cos(2\pi\tilde{f}_1 t + \angle s_{y1}) + |s_{y2}|\cos(2\pi\tilde{f}_2 t + \angle s_{y2})\}\sin(2\pi\tilde{f}_1 t) \\ &= \frac{|s_{y1}|}{2}\{\sin(4\pi\tilde{f}_1 t + \angle s_{y1}) - \sin(\angle s_{y1})\} + \frac{|s_{y2}|}{2}\{\sin(2\pi(\tilde{f}_1 + \tilde{f}_2)t + \angle s_{y2}) \\ &- \sin(2\pi(\tilde{f}_2 - \tilde{f}_1)t + \angle s_{y2})\} \end{aligned} \tag{2.25}$$

As discussed in Section 2.3-A, the cut-off frequency of the low-pass filters is significantly smaller than the crossover frequency; thus, the effect of the sinusoidal term at frequency $\tilde{f}_2 - \tilde{f}_1$ is negligible. As far as the two frequencies $\tilde{f}_1$ and $\tilde{f}_2$ are significantly different, (2.25) still approximates the dc term $s_y^I = -\frac{|s_{y1}|}{2}\sin(\angle s_{y1})$

with a good precision (a similar consideration holds for s_y^R). This means that the proposed scheme allows multiple converters to monitor their stability margins simultaneously and independently. Because, in each converter the effect of other converters with different perturbation frequencies is discarded, thanks to the orthogonality property.

However, it might be possible that at least two converters with similar crossover frequencies need to perform the monitoring simultaneously. In this case, (2.25) after low-pass filtering can be written as:

$$\begin{aligned} s_y(t)\sin(2\pi\tilde{f}_1 t) = -\tfrac{|s_{y1}|}{2}\sin(\angle s_{y1}) - \\ G_{LPF}(j2\pi(\tilde{f}_2-\tilde{f}_1))\tfrac{|s_{y2}|}{2}\sin(2\pi(\tilde{f}_2-\tilde{f}_1)t+\angle s_{y2}) \end{aligned} \tag{2.26}$$

in which $\tilde{f}_1 \simeq \tilde{f}_2$. The sinusoidal term at frequency $\tilde{f}_2 - \tilde{f}_1$ makes the extraction of the dc term s_y^I more difficult with respect to the case of single perturbation and leads, accordingly, to an error in the amplitude estimation. Of course, this issue worsens as the number of such converters increases.

The solution proposed herein is to modify the design of the LPFs used; in particular, by significantly decreasing the cut-off frequency of the LPF, or by changing its structure (e.g., increase the filter order). So doing, the effect of the term $\tilde{f}_2 - \tilde{f}_1$ can be better reduced, thanks to the higher filtering properties, achieving a better amplitude estimation. Clearly, this improvement comes at the price of a correspondingly slower response time of the monitoring process, that is a trade-off between accuracy and speed to be taken depending on the application.

2.5 Application to droop-controlled converters

The droop control is proposed in the literature to address various needs of dc microgrids, such as, bus voltage regulation, power sharing among sources, management of storage units, and islanded operation [18, 19]. The droop control scheme considered in this work is shown in Fig. 2.5. The inductor current i_L is sensed and used in the droop loop to produce the reference output voltage v_{ref} needed for the inner voltage loop:

$$v_{ref} = V_{sp} - k_d \cdot i_L \tag{2.27}$$

where V_{sp} is the dc bus voltage set-point and k_d is the droop coefficient. This allows bus voltage regulation and an automatic sharing of the power needs of the microgrid. Notably, due to the buck converters topology, the inductor current and

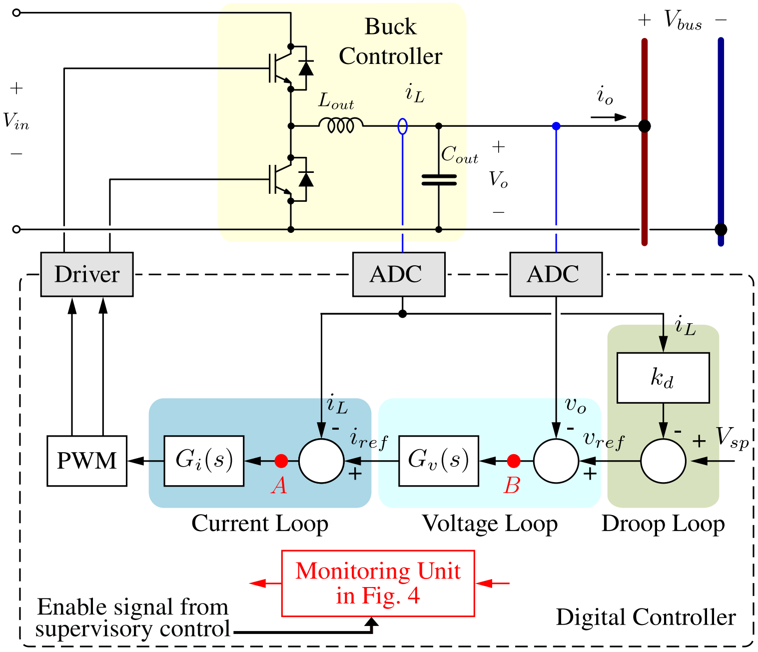

Fig. 2.5. Droop-controlled converter equipped with the proposed stability monitoring unit, that can be activated by an enable signal from supervisory controller.

the output current are equal in the steady-state conditions, thus no additional sensing is required.

The application of the proposed monitoring tool to the droop-controlled converters operating in dc microgrids is investigated in this work. Specifically, three different loops are considered: the inner inductor current control loop, the output voltage control loop, and the droop control loop, as shown in Fig. 2.5. When the monitoring unit is inserted at point A, while the other loops are open, the stability margins of the current loop is monitored. By inserting the monitoring unit at point B, while the droop loop is open, the stability margins of the voltage loop is monitored. The perturbation is inserted in point B for the droop loop too, but having all the other loops closed. The regulators parameters for the current and voltage loops can be designed based on standard procedures, as discussed, for example, in [39].

2.6 Simulation and experimental results

The prototype considered in this work is shown in Fig. 2.6, which emulates an islanded dc microgrid [1]. The parameters of this setup are listed in Table 2.1. It

---

[1] The experimental validations presented in this work are carried out on the same prototype as in [78]. The contribution of Eng. Guangyuan Liu in this development is highly appreciated.

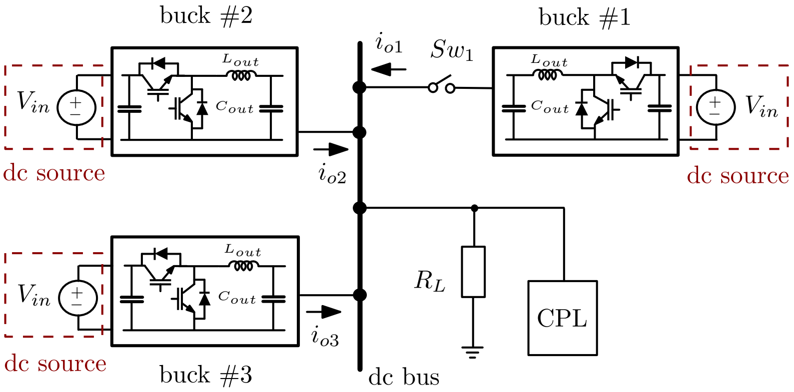

Fig. 2.6. Dc microgrid prototype under study including three buck converters, each converter implementing the control structure displayed in Fig. 2.5.

Parameter	Symbol	Value
Input voltage	V_{in}	380 V
Nominal bus voltage	V_{bus}	200 V
Nominal power	P^{nom}	3 kW
Output side inductance	L_{out}	1.6 mH
Output side capacitance	C_{out}	110 µF
Switching frequency	f_{sw}	12.5 kHz
Load Resistance	R_L	150 Ω
Rated power of the CPL	P_{CPL}	3 kW

Table 2.1: Parameters of the setup shown in Fig. 2.6

consists of three droop-controlled buck converters, a converter behaving as CPL, and a resistive load, all connected to a common dc bus. The three buck converters implement the same hardware and the same control structure which is shown in Fig. 2.5. Table 2.2 lists the regulators parameters, notably, converters #1 and #2 use the same parameters values, which are different from those of converter #3. During this work, the switch Sw_1 is always closed, apart from the case concerning the transient behavior of the system.

The technique is firstly developed and analyzed by simulation models in Matlab/Simulink. Then, the designed regulators, together with the proposed monitoring technique, have been deployed in the digital controller of the prototype, which is based on a Texas Instrument DSP (TMS320F2810) operating at 150 MHz. To this end, the analog-to-digital converter (ADC) of the DSP samples the output voltage and the inductor current once per switching period (i.e., $f_{sampling} = f_{sw} = 12.5\,\text{kHz}$), with a resolution of 12 bit. In the DSP code, the MT in Fig. 2.2 is performed first; then, the converters controllers are implemented to obtain the new value of the duty cycle; finally, the drive signals are generated by means of the

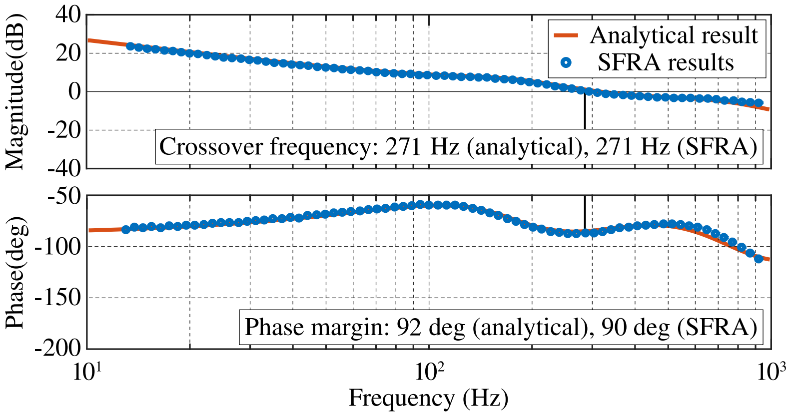

Fig. 2.7. Droop loop transfer function of converter #2 in Fig. 2.6: analytical versus experimental data.

PWM modules of the DSP. The measured total execution time of the implemented MT is 14.8 µs, without any specific code optimization.

In order to evaluate the performance of the proposed MT, the stability margin values monitored in the experimental model are compared to those represented by the actual transfer function of the experimental setup, which is acquired by means of the Sweep Frequency Response Analysis (SFRA) tool [79]. The analytical and the actual transfer functions of different control loops have been evaluated and compared. However, herein, for brevity, just the transfer functions related to the droop loop of converter #2 are reported in Fig. 2.7. Of course, the loop under study is affected by the other converters in the prototype, and this effect is included in the displayed transfer functions. The close matching between the transfer functions found analytically and those of the experimental setup measured by the SFRA tool, proves the correctness of the adopted models.

Parameter	Symbol	Value
	current loop	
Current regulator of all converters	G_i	$0.02 + 74.89/s$
	voltage loop	
Voltage regulator of buck #1, #2	$G_v^{\#1,\#2}(s)$	$0.21 + 544/s$
Voltage regulator of buck #3	$G_v^{\#3}(s)$	$0.1 + 272/s$
	droop loop	
Voltage set point	V_{sp}	200 V
Droop coefficient	k_d	1.33 V/A

Table 2.2: Regulators parameters of the converters in Fig. 2.6

In the following, the experimental results obtained by applying the stability monitoring tool to three different control loops are reported and discussed. In particular, the MT is applied to the single converter's inner current and voltage loops and to the droop loop of each of the three droop-controlled buck converters. As we are dealing with a multi-converter setup, the supervisory control described in Section 2.4 is adopted to activate the monitoring units of different converters sequentially and without overlaps.

The effect of the small-signal perturbation on the output signals is derived analytically in the previous Section. The amplitude of the sinusoidal perturbation is set in such a way that, after injecting the perturbation in any of the loops, the output current and voltage ripples due to perturbation injection are reasonably low in steady-state (in the case herein considered, less than two percent of the rated values). Still, the small signal perturbations on the output signals most be larger than the quantization error and the noise levels.

2.6.1 MT applied to the inner current and voltage loops

In this subsection, the MT is applied at point A in Fig. 2.5 (with the voltage and droop loops open) and at point B (with the droop loop open), to monitor the stability margins of the current and the voltage loops of a single buck converter, respectively.

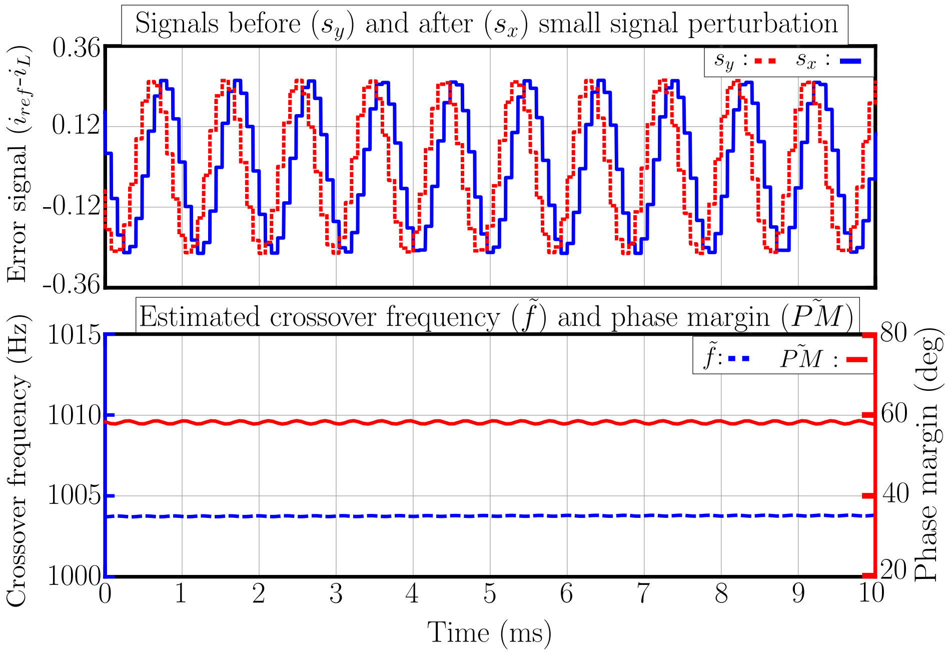

Fig. 2.8. Simulation results of the current loop stability monitoring. Parameters listed in Table 2.1 and Table 2.2.

The results obtained by the simulation models replicating the experimental setup are shown in Table 2.3. The MT results are close to those expected from the analytical models. Fig. 2.8 shows the detailed simulation results of the MT applied to the current loop. The resulting perturbation frequency of the two signals s_y and s_x is equal to the crossover frequency and the phase difference is equal to the phase margin, as expected from (2.2) and (2.4), respectively. The same good matching has been achieved considering the voltage loop (herein the results are skipped for brevity).

The experimental results of the monitoring tool applied to the current and voltage loops are shown in Fig. 2.9a and Fig. 2.9b, respectively. As reported in Table 2.3, on the basis of the transfer functions of the experimental setup found by the

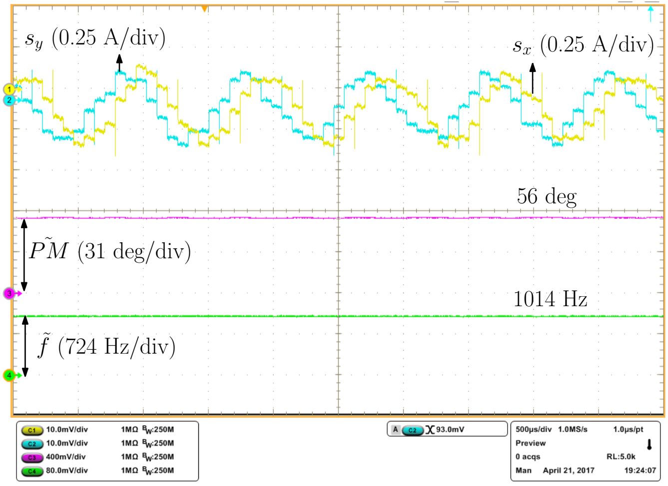

(a) Current loop stability monitoring. Time scale: 0.6 ms/div

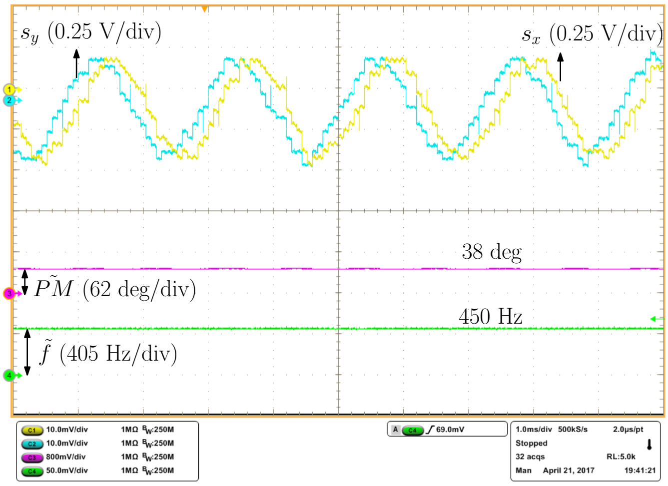

(b) Voltage loop stability monitoring. Time scale: 1 ms/div

Fig. 2.9. Experimental results of applying MT to the current and the voltage loops of a single buck converter.

SFRA tool, the expected values of the crossover frequency and phase margin for the current loop are 1000 Hz and 58 deg, respectively. The estimates from the MT shown in Fig. 2.9a are 1014 Hz, for the crossover frequency, and 56 deg, for the phase margin. As for the voltage loop, the expected crossover frequency and phase margin are 460 Hz and 41 deg, respectively; the estimates from the MT correspond to 450 Hz and 38 deg, as reported in Fig. 2.9b. The obtained results are consistent and show that the MT performs well in steady-state conditions, for both the current and voltage loops. From Fig. 2.9a and Fig. 2.9b it is also possible to notice that the amplitudes of the digital signals before and after injecting a small-signal perturbation (i.e., s_y, s_x) tend to be equal in steady-state, which corresponds to the condition stated in (2.2).

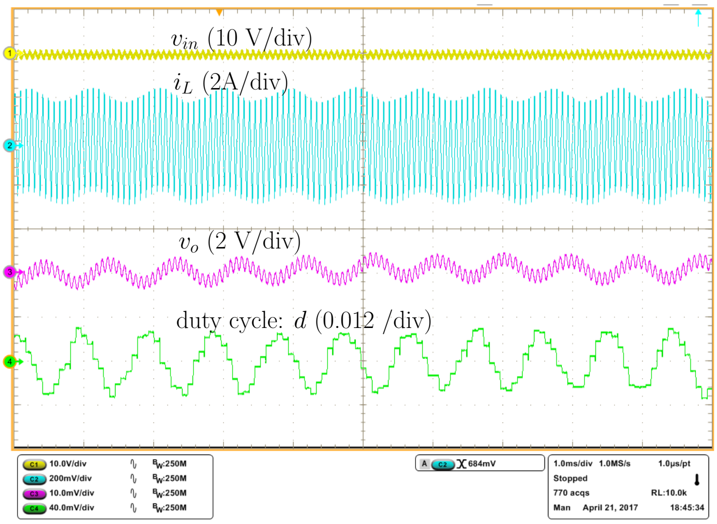

(a) Applying MT to the current loop

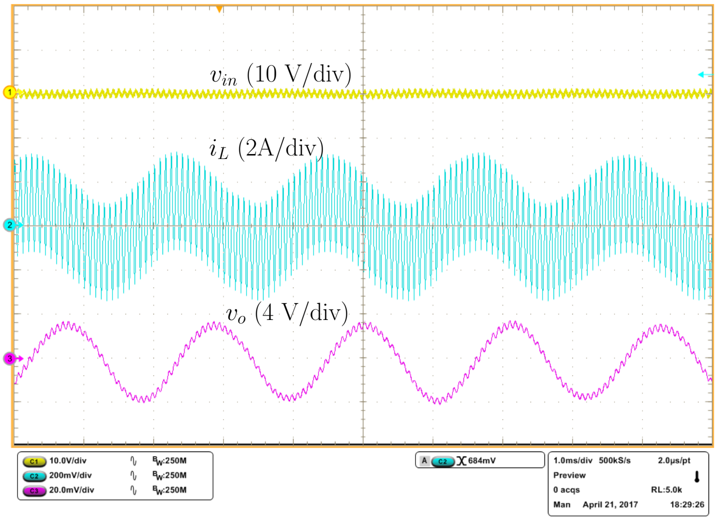

(b) Applying MT to the voltage loop

Fig. 2.10. Ripples in the input voltage v_{in}, output voltage v_o and inductor current i_L, in presence of small-signal perturbations coming from MT. Time scale : 1 ms/div.

Fig. 2.10 shows the ripples in the steady-state waveforms of the input and output voltages and the inductor current in presence of the small-signal perturbations injected for monitoring the current (Fig. 2.10.a) and voltage (Fig. 2.10.b) loops. In addition, the duty-cycle fluctuations for the case of current loop is also displayed in Fig. 2.10.a. It is possible to notice that the ripple stays within a reasonable range. In the case of the current loop, less than 0.5 V and 0.2 A ripple in the output voltage and the inductor current, respectively, are observed. In the case of the voltage loop, the measured ripples are slightly larger than the current loop case, but still low enough to not significantly affect the normal operation of the system.

2.6.2 MT applied to the droop loop

The application of the MT to converters implementing droop control, as discussed in Section 2.5, is investigated in this subsection. To analyze the stability of the droop loop for each of the converters in Fig. 2.6, the small-signal perturbation is injected at point B of Fig. 2.5. During this test, the three droop-controlled buck converters in Fig. 2.6 operate in parallel. As discussed in Section 2.4, multiple converters can monitor their stability margins either simultaneously or based on a time division multiplexing algorithm defined by the supervisory controller.

	crossover frequency	phase margin
current loop of a single converter		
Expected from transfer function (analytical model)	1000 Hz	60 deg
Expected from transfer function (SFRA results)	1000 Hz	58 deg
Monitored online (simulation)	1003 Hz	58 deg
Monitored online (experimental)	1014 Hz	56 deg
voltage loop of converter #2		
Expected from transfer function (analytical model)	460 Hz	40 deg
Expected from transfer function (SFRA results)	460 Hz	41 deg
Monitored online (simulation)	458 Hz	39 deg
Monitored online (experimental)	450 Hz	38 deg
droop loop of converter #2		
Expected from transfer function (analytical model)	271 Hz	92 deg
Expected from transfer function (SFRA results)	271 Hz	90 deg
Monitored online (simulation)	272 Hz	89 deg
Monitored online (experimental)	271 Hz	91 deg

TABLE 2.3: Expected values of the stability margins, and the MT results

Fig. 2.11 shows the simulation results of the MT applied to the droop loop of the three converters shown in Fig. 2.6, in both simultaneous and non-simultaneous cases. The expected margins for the droop loop of converter #1 are similar to those of converter #2, which are reported in Table 2.3; differently, the analytically expected stability margins for converter #3 are 195 Hz and 102 deg, for the crossover frequency and phase margin, respectively. As can be seen in Fig. 2.11, the stability margins monitored on-line in the non-simultaneous case are very close

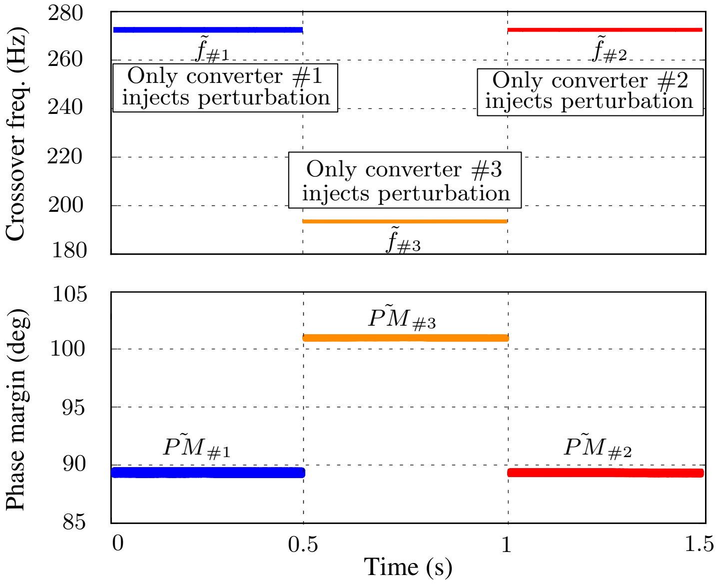

(a) Non-simultaneous monitoring (assigning a monitoring window to each converter)

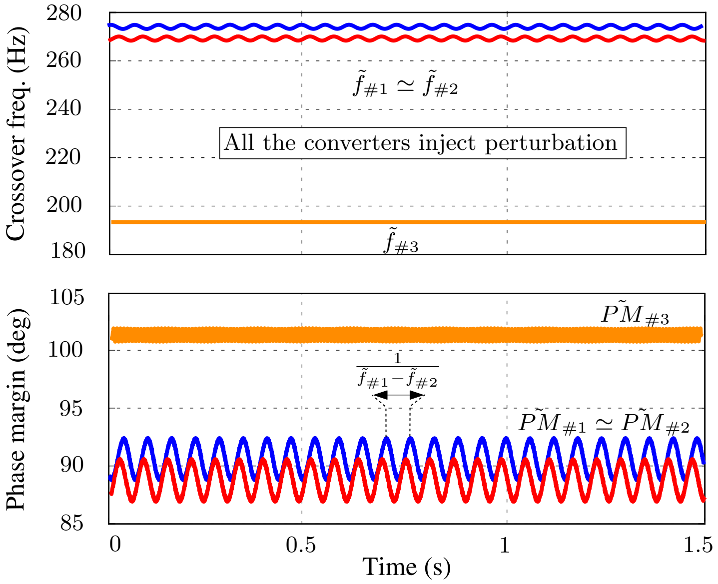

(b) Simultaneous monitoring (decreasing the LPF cut-off frequency)

Fig. 2.11. Simulation results of applying MT to the droop loop of the converters in Fig. 2.6.

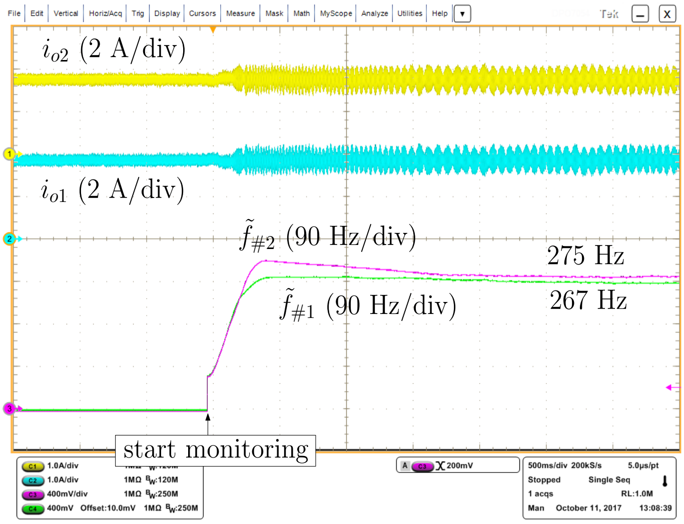

Fig. 2.12. Experimental results of the simultaneous monitoring of the droop loops of converters #1 and #2 in Fig. 2.6.

to those expected by the analytical models, reported in Table 2.3. However, in the case of simultaneous perturbations at similar frequencies, the precision slightly decreases, due to the effect of the $\tilde{f}_1 - \tilde{f}_2$ component, as explained while referring to (2.26). Here, f_{lpf} is set to 1 Hz, which leads to reasonable precision, namely, an error of about 1% for the phase margins and 0.4 % for the crossover frequency, as visible in Fig. 2.11. Another point worth remarking is that the perturbation coming from converter #3 has negligible effect on the monitored values of the other two converters, thanks to the orthogonality property among sinusoidal signals at different frequencies, as discussed in Section 2.4.B. The experimental confirmation of this point is reported in Fig. 2.12. In this figure, only the estimated crossover frequencies of converter #1 and converter #2 are shown, which show a small error (around 1%), with respect to the expected value (271 Hz). The same accuracy is observed for the phase margins, which are not herein reported. For simplicity, in the rest of this chapter, the monitored stability margins of just one converter (i.e., converter #2) are reported. According to Table 2.3 and Fig. 2.7, on the basis of the transfer function measured by SFRA tool for the droop loop of converter #2, the expected crossover frequency and phase margin are 271 Hz and 90 deg, respectively. The values monitored on-line are 271 Hz and 91 deg, reported in Fig. 2.13. This close matching between the estimated and the monitored values proves the effectiveness of the proposed MT applied to the droop control loop. In addition, Fig. 2.13 shows the ripples in the output voltage and current of the converter that performs the stability monitoring, these ripples measure less than 0.5% of the nominal voltage and 3% of the nominal current. This small effect on the output signals is allowed by choosing the perturbation amplitude $|s_z|$ according to the appendix. By the reported method, values of $|s_z|$ can be identified that are

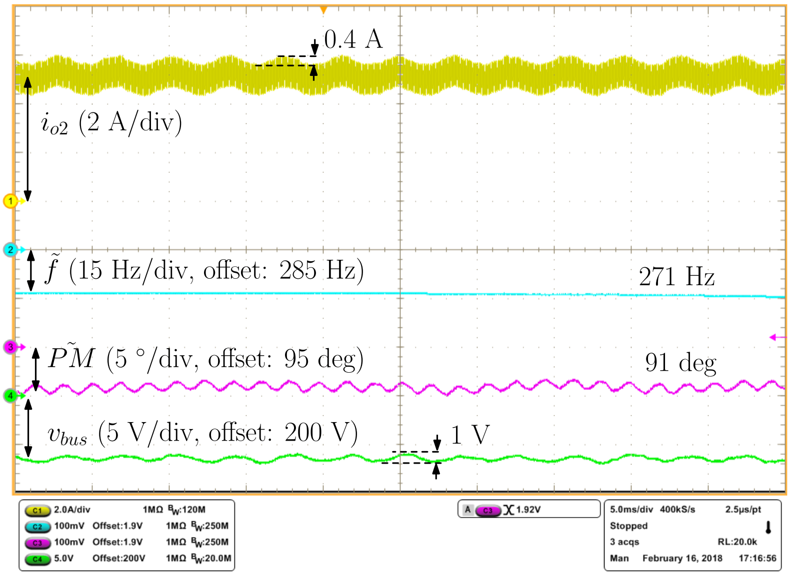

Fig. 2.13. Experimental results of applying MT to the droop loop of converter #2 in Fig. 2.6. Time scale : 5 ms/div.

small enough to produce negligible perturbations on the system's operating point but still significantly higher than the noise and the analog-to-digital quantization levels.

As discussed in Section 2.3-A, the LPFs used in Fig. 2.2 have the task to reject the ripple at twice the perturbation frequency. Therefore, their cut-off frequency should be chosen significantly lower than the expected crossover frequency of the loop under investigation. Different attenuation levels, obtained by changing the cut-off frequency or the order of the filter, result in different estimation accuracies. In order to show the effect of different LPF choices on the estimated stability margins, the previous experiment (i.e., droop loop of converter #2) is repeated with three different values of cut-off frequency f_{lpf}. The results are reported in Fig. 2.14. As can be noticed, the choice of f_{lpf} does not affect the average values of the obtained estimates, but it affects the superimposed sinusoidal fluctuation at $2\tilde{f}$, as highlighted also in (2.8) and (2.9). Fig. 2.14 shows that higher values of f_{lpf}, bring to larger estimation errors—however, the amount of this effect on $\tilde{PM}$ is different from the effect on $\tilde{f}$, due to different signal processing paths: $\tilde{f}$, for example, benefits from the additional filtering action of the integration block $G_{\tilde{f}}$, as described in Fig. 2.2. In a nutshell, f_{lpf} can be decreased in order to reduce the estimation error, but as addressed in Section 2.3-B, it should not be so small to also affect the design of the frequency regulator $G_{\tilde{f}}$.

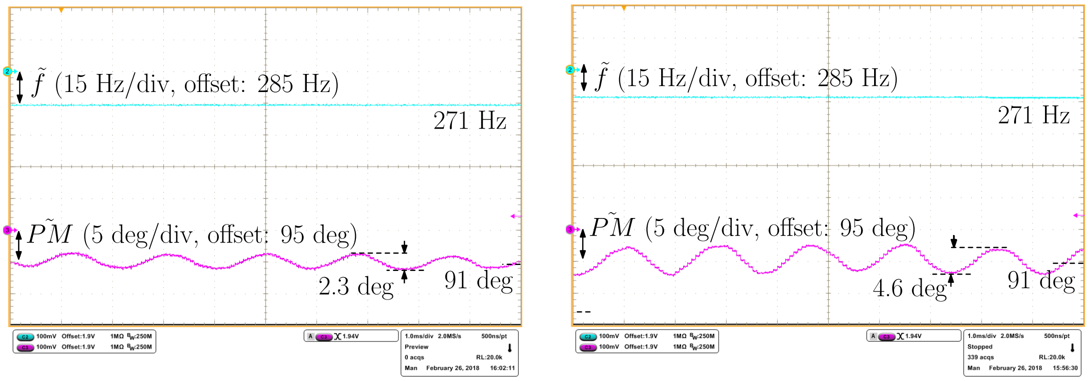

(a) f_{lpf} = 5 Hz (b) f_{lpf} = 10 Hz

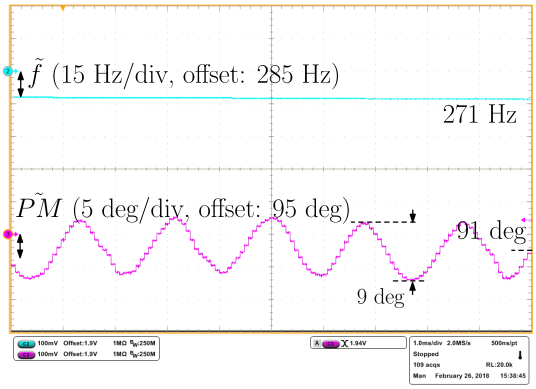

(c) f_{lpf} = 20 Hz

Fig. 2.14. Effect of the LPF cut-off frequency on the monitored crossover frequency ($\tilde{f}$) and phase margin ($\tilde{PM}$). Time scale : 1 ms/div.

2.6.3 Dynamic behavior of the MT

In previous experiments, the stability monitoring tool was tested in steady-state conditions. In order to further assess the applicability of the proposed MT in dc microgrids, the performance of the method under three different dynamic conditions is evaluated and reported in this subsection.

(i) The first transient is applied to the considered dc microgrid prototype by opening the switch Sw_1 in Fig. 2.6. The load is initially shared among the three buck converters, but after disconnecting converter #1, the load has to be shared among the remaining converters, that are converters #2 and #3, as shown in Fig. 2.15a. As expected from the discussion in Section 2.5, the droop technique allows to achieve an equal load sharing and bus voltage regulation along the considered test case. As the transfer functions of the droop loop of converter #2 before and after the transient are different, and the monitored stability margins are expected to show the corresponding

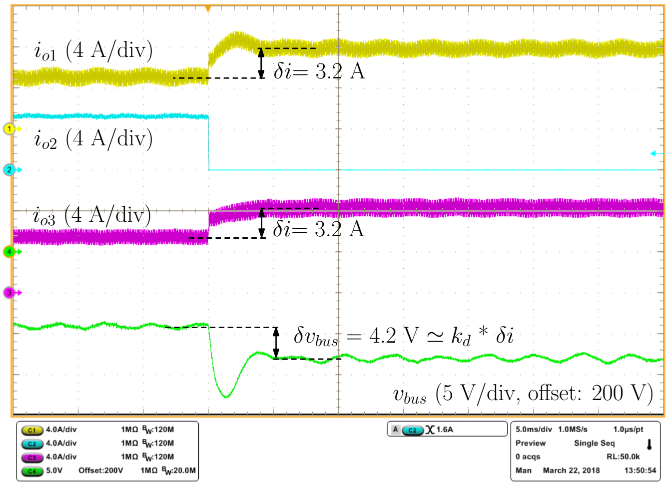

(a) Performance of the droop control loop implemented in the converters of Fig. 2.6

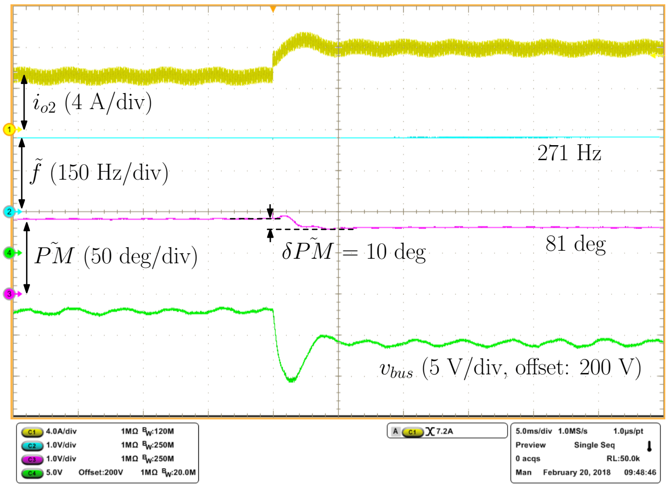

(b) Performance of the stability monitoring unit applied to the droop loop of converter #2

Fig. 2.15. Experimental results under transient: opening the switch Sw_1 in Fig. 2.6. Time scale : 5 ms/div.

changes. After opening the switch Sw_1 in Fig. 2.6, based on the SFRA results, the phase margin of the droop loop of converter #2 decreases by about 10 deg, while the crossover frequency remains approximately unchanged (i.e., variations $< 3\,$Hz). This is confirmed by the experimental results displayed in Fig. 2.15b, which reports the MT applied to the droop loop of converter #2, under the the considered transient. Fig. 2.15b also highlights the response time of the MT, which is less than 5 ms, if measured from 10% to 90% of the total variation. This fast achievement of the stability margins, together with the simple implementation, make this approach practical for dc mcirogrid applications.

(ii) The second transient is applied to the system shown in Fig. 2.6, when the

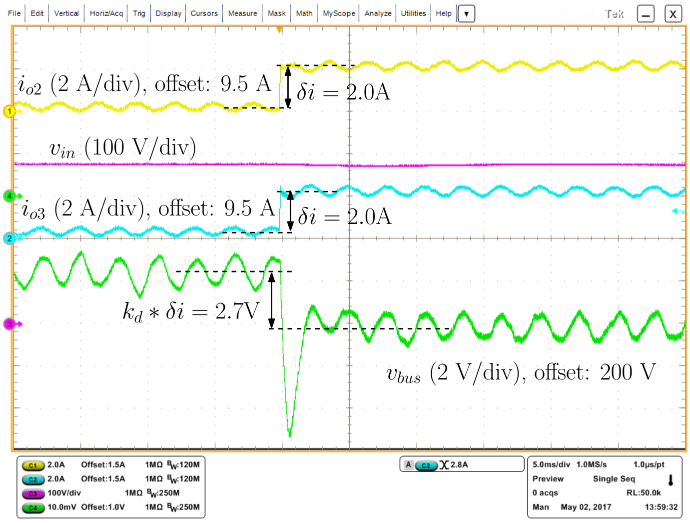

(a) Performance of the droop control loop implemented in the converters of Fig. 2.6. Time scale : 5 ms/div.

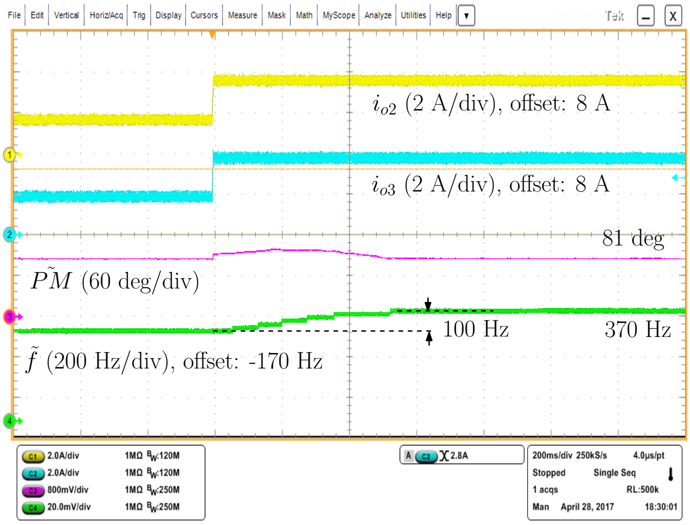

(b) Performance of the stability monitoring unit applied to the droop loop of converter #2. Time scale : 200 ms/div.

Fig. 2.16. Experimental results under transient: $R_L \rightarrow \frac{R_L}{2}$. During this experiment, the switch Sw_1 is still open.

switch Sw_1 is still open, i.e., the load is shared between the converters #2 and #3. For this case, the load R_L is decreased by a factor of two. Similarly to the previous case, the two operating points (before and after the transient) have different transfer functions, so the crossover frequency and the phase margin will change. As shown in Fig. 2.16b, the crossover frequency increases almost 100 Hz and the phase margin decreases. Even though, the change in phase margin is not easily visible in the figure due to the unfavorable scale of the oscilloscope. Moreover, by looking at Fig. 2.16b and Fig. 2.16a, it is possible to notice that the droop controller is effective in obtaining equal

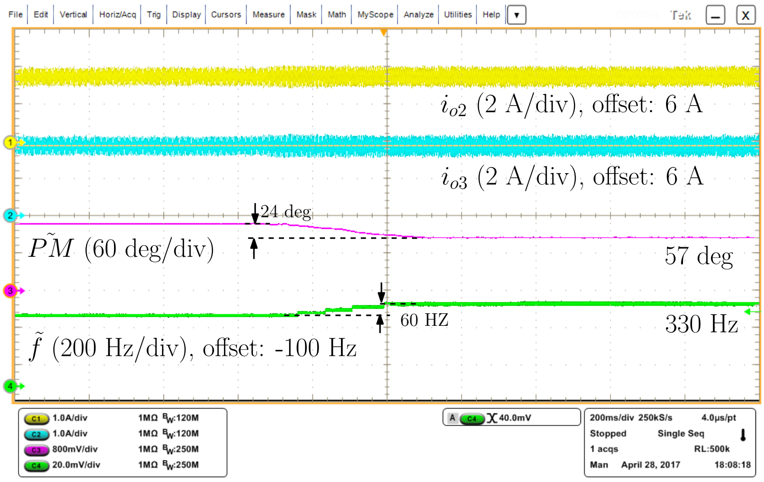

Fig. 2.17. Stability monitoring and the load sharing under transient: increasing a control parameter (the integral gain of the voltage regulator in this case). Time scale : 200 ms/div. During this experiment, the switch Sw_1 is still open.

load sharing, bus voltage control, and increasing stability. The change in the output currents (about 2 A) multiplied by the droop coefficient (1.33), gives us the same value of the output voltage variations.

(iii) The third transient is applied to the setup shown in Fig. 2.6, when the switch Sw_1 is still open, i.e., the load is shared between the converters #2 and #3. In this case, a control parameter is changes and the system performance is observed under this transient. In particular, the integral gain of the voltage regulator k_{int} of the converter in which the injection is applied, is increased as: $\frac{k_{int}}{2} \rightarrow k_{int}$. Then, the currents of both converters #2 and #3, as well as the monitored stability margins are shown in Fig. 2.17. Even in this case, the proposed stability monitoring tool shows a proper operation in transient as well as in steady state conditions. About 60 Hz change in the crossover frequency and 24 deg change in the phase margin, is what we expect due to the change in the operating point.

2.7 Summary

An on-line stability monitoring technique for power converters operating in dc microgrids is presented in this chapter. The technique is inspired by the Middlebrook's injection method, and allows to estimate and monitor the stability margins of any control loop under consideration (e.g., current, voltage, or droop control loops). The proposed monitoring technique is described in details, also discussing the possible design choices and trade-offs. Since this work targets the application of the method in a multiple-converter environment, which is not specifically addressed in the current literature, the presence of multiple perturbations coming from the monitoring units of several converters is also investigated. In particular a time division multiplexing is considered for the general scenarios, and a small modification is applied in the MT for some particular cases where there is a strict need for simultaneous monitoring of some converters. An experimental setup composed of three buck converters, a constant power load, and a resistive load is implemented to emulate a dc microgrid. The current, the voltage and the droop loops are tested, reporting a close match between the obtained experimental results from the monitoring unit and the values expected from the measured transfer functions. The accuracy obtained in the estimates of the stability margins, in both steady-state and transient conditions, validates the effectiveness of the proposed approach. The reported results also show that the bus voltage and the inductor current are not significantly affected by the small-signal perturbations injected for stability monitoring purposes if the provisions discussed in this chapter are applied. In conclusion, the proposed scheme is fast, accurate, and simple, and represents a promising candidate for adaptive control and auto-tuning of power converters within dc microgrids.

Chapter 3

Autotuning of DC microgrid power converters

3.1 Introduction

Different approaches are reported in the literature to adaptively tune the control parameters of power converters during their normal closed-loop operation. In many works [40, 46, 49, 50, 80–83], the entire frequency response of the loop under study is identified and the proportional-integral-derivative (PID) gains of the controller are adjusted to achieve the desired behavior for that loop. Identification of the frequency response is performed by either narrow-band injections, such as sine sweep [40], or wide-band injections, such as pseudo-random binary sequences (PRBSs) [46,80–82]. Other system identification techniques are reported in [49,50,83], that address different methods to estimate the loop transfer function, followed by tuning and correction tasks. The above-mentioned methods, however, require to capture long sequences of data and perform to Fourier Transform, needing, thus, an auxiliary processor in the implementation.

Some other tuning approaches are proposed in [69, 84], that bring with less computational effort, as they do not require capturing long sequences of data and performing Fourier Transform. In these methods, some limit-cycle oscillations are created in the system, for example, by introducing a perturbations on the output voltage during the converter soft-start. The oscillation frequency is then measured and used for proper placement of the zeros of PID compensator. The iterations continue till the oscillation frequency equals the desired crossover frequency. Also, a low-pass filter is applied to force the desired phase margin at the reference crossover frequency. However, these limit-cycle-based methods, also called as relay-feedback methods, have less identification capabilities with respect to the frequency response measurement methods. Also, based on the relay-feedback approach, a relatively large oscillation can be induced in the output of the converter, although for a short period of time.

Extension of the Middlebrook's analog injection technique [51], to the digitally-controlled power converters, is the basis of some other studies [85]. The concept of these methods is to firstly, find the crossover frequency and phase margin of a control loop, and then to tune the PID parameters of that loop, in order to make the crossover frequency and phase margin follow some given references. More specifically, in this technique, a small-signal perturbation is injected into the converters control loops, and the loop gain at the injection frequency is measured. Then, the injection frequency is adjusted (with an additional PI regulator) to find the unity-gain frequency, i.e., the crossover frequency. At this frequency, the phase-shift between the signals before and after perturbation point, gives the phase margin. This technique requires an effectively low signal processing effort, and it is able to perform accurately even in presence of load transients. and it gives the possibility to control the perturbation amplitude. However, continuous monitoring of the stability margins needs to adjust the injection frequency with an additional regulator, whose design and digital implementation would require some further steps.

Some model reference-based tuning approaches are proposed in [67, 68]. In this techniques, a perturbation with constant frequency—equal to the desired crossover frequency—is assumed; removing, thus, the need to the above-mentioned regulation of the injection frequency. The small-signal perturbation is injected into a generic loop, and by processing the signals right before, and right after the injection point, the desired crossover frequency and phase margins is obtained based on continuously changing the PID parameters.

This chapter applies a similar concept as [68] to on-line tuning of dc microgrid power converters. Two simple signal processing algorithms are presented to auto-tune a generic control loop within power converters. Both approaches are based on injecting a perturbation at the reference crossover frequency in the feedback path of the loop under study. In addition, this work takes account for the situation in which an unfeasible phase margin is desired. This can happen when the applied PI or PID provides its maximum allowable phase to compensate a generic loop, at the reference crossover frequency; but, still the phase margin of that loop is less than the desired reference phase margin. To tackle this issue, an additional loop is added to the autotuning block, which adjusts the reference crossover frequency based on the error between maximum reachable phase margin and the reference phase margin. Hence, the loop under study, is able to always work at its maximum allowable bandwidth. To summarize, the proposed techniques:

- are simple and require a short execution time.
- allow the loop under study to achieve the reference phase margin at the maximum achievable bandwidth.
- are robust to noise and perturbations coming from the other converters connected to the common dc bus. Thus, these techniques allow multiple converters to auto-tune their regulators, simultaneously and independently.

The remainder of this chapter is arranged as follows. Section 3.2 presents the main concept of the proposed autotuning techniques for dc microgrid power converters. Section 3.3 describes the proposed signal processing algorithm and different design aspects. In Section 3.4, an experimental prototype of a dc microgrid is implemented, in which, one of the proposed autotuning techniques is tested.

3.2 Concept Description

Fig. 3.1 shows the basis of unity-loop-gain measurement and tuning, without interrupting the feedback path. The technique is based on the fact that, the ratio between the signals before and after perturbation, gives the loop gain: $T = -s_y/s_x$. So, a small-signal perturbation, at the reference crossover frequency, is injected into a generic loop T, in order to stimulate and acquire the system behavior at that frequency. Then, the signals s_x, s_y are being processed, and used to update the PID parameters, to achieve certain performance for the loop T.

To have a clearer insight on the main idea of this technique, let us remind that, by definition [51], a control loop transfer function shows unity gain at the crossover frequency f_c:

$$|T(j\,2\pi f_c)| = |\frac{-s_y(j\,2\pi f_c)}{s_x(j\,2\pi f_c)}| = 1 \tag{3.1}$$

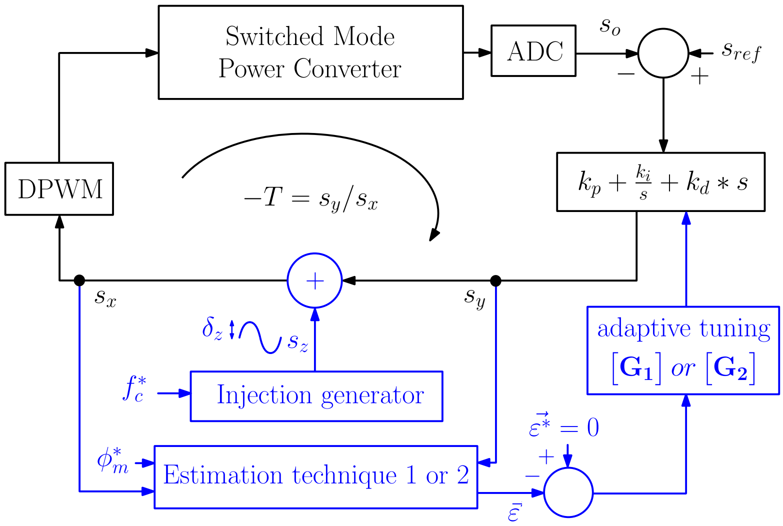

Fig. 3.1. Autotuning of a generic control loop T of digitally-controlled power converters. The compensator gains (k_p, k_i, k_d) are tuned by the matrix $\mathbf{G_1}$ (or $\mathbf{G_2}$) to reach zero error $\vec{\varepsilon}$, i.e., to achieve reference stability margins (f_c^*, ϕ_m^*). The error $\vec{\varepsilon}$ can be defined either based on the estimation technique 1 in 3.3.1, or based on the estimation technique 2 in 3.3.2.

At this frequency, the phase shift between the two signals s_x and s_y is the phase margin:

$$\phi_m = 180 + \angle T(j\,2\pi f_c) = \angle s_y(j\,2\pi f_c) - \angle s_x(j\,2\pi f_c) \tag{3.2}$$

Then, the goal of autotuning is to adaptively update the compensator gains appropriately, in such a way that:

1. the crossover frequency of the considered loop T reaches the desired reference value: $f_c \to f_c^*$, then: $|T(j\,2\pi f_c^*)| = |s_y(j\,2\pi f_c^*)/s_x(j\,2\pi f_c^*)| \to 1$.
2. the phase margin of T converges to the reference phase margin: $\phi_m \to \phi_m^*$, then: $\angle s_y(j\,2\pi f_c^*) - \angle s_x(j\,2\pi f_c^*) \to \phi_m^*$.

In order to meet the two requirements mentioned above, different signal processing methods can be considered [67, 68]. Regardless of the way to process, the two signals s_y and s_x need to have a phase-shift equal to ϕ_m^* at the desired crossover frequency f_c^*.

Hence, as long as there exist a unity loop gain frequency f_c (i.e., $|T(j2\pi f)| > 1$ for some frequencies), these techniques are able to tune the PID gains in order to make f_c equal to the injection frequency f_c^*. Unlike [85], in which the injection frequency needs to be regulated with an additional PI.

3.3 Proposed tuning techniques

In the following two possible ways are proposed to define the tuning error vector $\vec{\varepsilon}$. The obtained $\vec{\varepsilon}$ based on estimation technique 1 is processed by $\mathbf{G_1}$ to tune k_p, k_i, k_d, and the obtained $\vec{\varepsilon}$ based on estimation technique 2 is processed by $\mathbf{G_2}$. In both cases, enforcing $\vec{\varepsilon}$ to converge to zero, will imply the successful achievement of the reference crossover frequency and the reference phase margin.

3.3.1 Estimation technique 1

As shown in Fig. 3.2, the first proposed technique to obtain $\vec{\varepsilon}$ is based on two principles: a) the difference between the amplitudes of s_x and s_y shows the convergence to the reference crossover frequency. b) the difference between the phases of s_x and s_y shows the convergence to the reference phase margin.

To better explain the estimation technique 1 in Fig. 3.2, let us assume that a sine small-signal perturbation s_z of amplitude δ_z, with frequency equal to the desired crossover frequency f_c^* is injected into a generic control loop of the power converter.

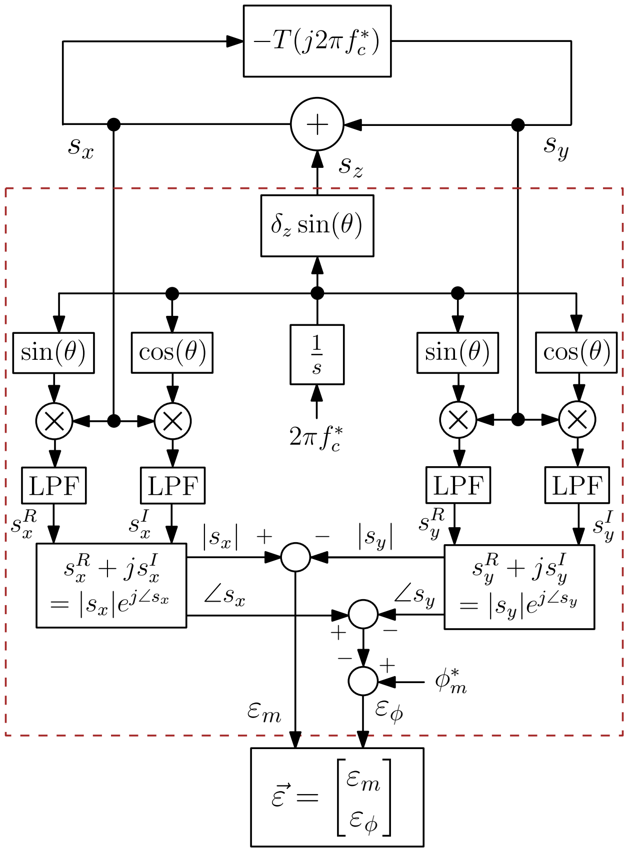

Fig. 3.2. Estimation technique 1.

This results in a perturbation with the same frequency f_c^* in the signals s_x, s_y.

$$s_x = |s_x| \cos(2\pi f_c^* t + \angle s_x), \quad s_y = |s_y| \cos(2\pi f_c^* t + \angle s_y) \tag{3.3}$$

These sinusoidal signals can be projected into a common reference frame defined by the in-phase (i.e., sin) and the quadrature (i.e., cos) components of the reference crossover frequency. The obtained projections can be represented in any two-dimensional reference frame, like, for example, the complex plane. Herein, the projections are performed through multiplication by sin and cos terms of the reference crossover frequency [72]. For example, projection of s_x gives:

$$s_x(t) \sin(2\pi f_c^* t) = -\frac{|s_x|}{2} \sin(\angle s_x) + \frac{|s_x|}{2} \sin(4\pi f_c^* t + \angle s_x) \tag{3.4}$$

$$s_x(t) \cos(2\pi f_c^* t) = \frac{|s_x|}{2} \cos(\angle s_x) + \frac{|s_x|}{2} \cos(4\pi f_c^* t + \angle s_x) \tag{3.5}$$

The same can be written for s_y. According to the basic trigonometric rules, after multiplication of two *sin* terms with similar frequency f_c^*, we obtain a dc value plus a high frequency component (at twice f_c^*). The dc values give the imaginary and the real components of the signal s_x at f_c^* (similarly for s_y). In order to remove the high-frequency component at $2f_c^*$, some first-order low-pass filters (LPFs) are used, as shown in Fig. 3.2. If the cut-off frequency of the LPFs f_{lp} is much lower than $2f_c^*$, then, the high frequency components in (3.4) and (3.5) can be discarded. This implies an accurate estimation of the real and imaginary components of s_x: $s_x^I = -\frac{|s_x|}{2} \sin(\angle s_x)$, $s_x^R = \frac{|s_x|}{2} \cos(\angle s_x)$. These values can then be used to find the magnitude and the phase of s_x: $s_x^R + j s_x^I = |s_x| e^{j\angle s_x}$. Similarly, one can derive s_y^R, s_y^I, than can be represented in the polar form: $s_y^R + j s_y^I = |s_y| e^{j\angle s_y}$.

Based on $|s_x|$, $|s_y|$, $\angle s_x$ and $\angle s_y$, the error vector $\vec{\varepsilon}$ can be defined as follows:

$$\vec{\varepsilon} = \begin{bmatrix} \varepsilon_m \\ \varepsilon_\phi \end{bmatrix} = \begin{bmatrix} |s_x| - |s_y| \\ \phi_m^* - (\angle s_x - \angle s_y) \end{bmatrix} \tag{3.6}$$

Then, as mentioned above, $\mathbf{G_1}$ is used to appropriately tune the PID gains k_p, k_i, k_d, so that both components of the error vector $\varepsilon_m, \varepsilon_\phi$ can effectively converge to zero. Reaching the zero error $\vec{\varepsilon} = 0$, means to achieve the reference crossover frequency f_c^* and reference phase margin ϕ_m^* for the loop T.

3.3.2 Estimation technique 2

In the second proposed estimation technique shown in Fig. 3.3, $s_x(j\,2\pi f_c^*)$ is shifted by $\phi_m^*/2$ and $s_y(j\,2\pi f_c^*)$ is shifted by $-\phi_m^*/2$, so that a phase-shift of ϕ_m^* is enforced between the two signals s_x and s_y at f_c^* [86].

Scheme of the proposed signal processing technique to derive the error vector $\vec{\varepsilon}$ is shown in Fig. 3.3. Similarly to the previous case, the real and imaginary components of s_x and s_y can be found: s_x^R, s_x^I and s_y^R, s_y^I. Then, s_x is shifted by $\phi_m^*/2$, using the complex-domain multiplication, and s_y is shifted by $-\phi_m^*/2$. Finally, the phase-shifted vectors are subtracted to define the error vector $\vec{\varepsilon}$ that can be represented in any two-dimensional reference frame, like, for example, the complex plane:

$$\vec{\varepsilon} = \varepsilon^R + j\varepsilon^I = s_x e^{j\phi_m^*/2} - s_y e^{-j\phi_m^*/2} \tag{3.7}$$

That can be expressed in terms of s_x and s_y:

$$\begin{gathered}\vec{\varepsilon} = (s_x^R + js_x^I) * \big(cos(\phi_m^*/2) + jsin(\phi_m^*/2)\big) \\ -(s_y^R + js_y^I) * \big(cos(-\phi_m^*/2) + jsin(-\phi_m^*/2)\big)\end{gathered} \tag{3.8}$$

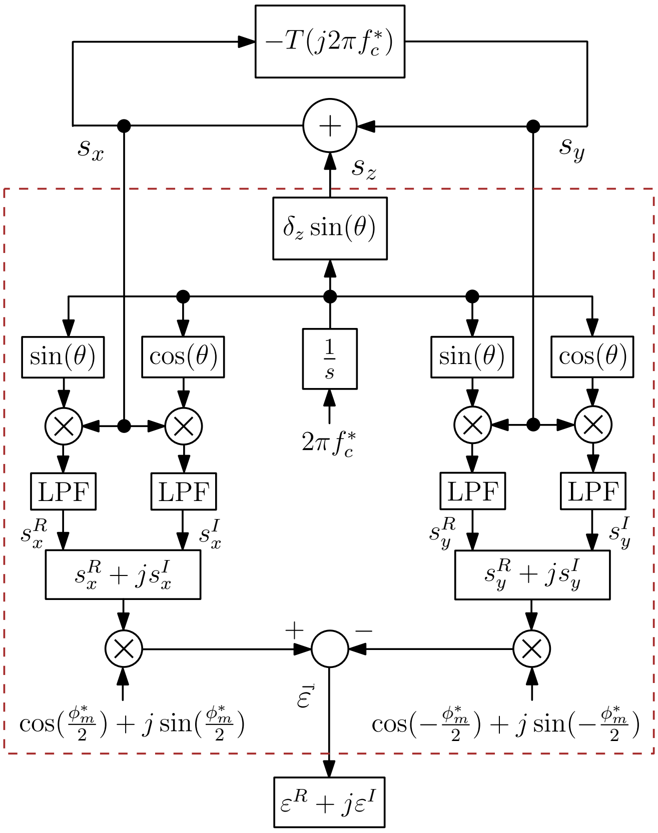

Fig. 3.3. Estimation technique 2.

According to (3.8), the complex components of the error vector $(\varepsilon^R, \varepsilon^I)$ can be expressed as follows:

$$\varepsilon^R = \big(s_x^R cos(\phi_m^*/2) - s_x^I sin(\phi_m^*/2)\big) - \big(s_y^R cos(-\phi_m^*/2) - s_y^I sin(-\phi_m^*/2)\big) \quad (3.9)$$

$$\varepsilon^I = \big(s_x^R sin(\phi_m^*/2) + s_x^I cos(\phi_m^*/2)\big) - \big(s_y^R sin(-\phi_m^*/2) + s_y^I cos(-\phi_m^*/2)\big) \quad (3.10)$$

At this point, the $\mathbf{G_1}$ is applied to appropriately tune the PID gains k_p, k_i, k_d, so that the real and imaginary components of the error vector $\varepsilon^R, \varepsilon^I$ both can effectively converge to zero. Reaching the zero error $\vec{\varepsilon} = 0$, means to reach the reference crossover frequency f_c^* and the reference phase margin ϕ_m^* for the loop T.

Notably, in both techniques of Fig. 3.3 and Fig. 3.2, the projection of the signals s_x, s_y along sine and cosine terms of a given crossover frequency f_c^*, leads to the rejection of any other frequency component that is different from f_c^*. Therefore, this approach is robust to noise and perturbations coming from other converters, connected to the common dc bus. This is because, at each converter, the effect of other converters with different perturbation frequencies—different values of f_c^*—is discarded, thanks to the orthogonality property. Similarly to [72], the LPFs can be further slowed down, in order to make the approach valid for the case of multiple converters, that their injection frequencies are very close to each others. More details on this can be found in [72].

3.3.3 Design of the tuning loop

To process the error vector $\vec{\varepsilon}$ that is obtained in the estimation technique 1, a tuning matrix $\mathbf{G_1}$ is applied. Similarly, $\vec{\varepsilon}$ obtained based on the estimation technique 2, is processed by $\mathbf{G_2}$. In general, design of $\mathbf{G_1}$ or $\mathbf{G_2}$ requires a model of the MIMO plant (from the PID gains up to the error vector). However, due to the system non-linearities, and possible changes in the system configuration, a rigorous modeling of this MIMO loop is not trivial and would require further information. Instead, herein, some simplifying assumptions are used, which allow to approximate the MIMO plant, and to design the tuning matrix. For brevity, herein, just the design aspects of $\mathbf{G_2}$ are described. Of course, similar reasoning and assumptions can be used in the case of $\mathbf{G_1}$, as well.

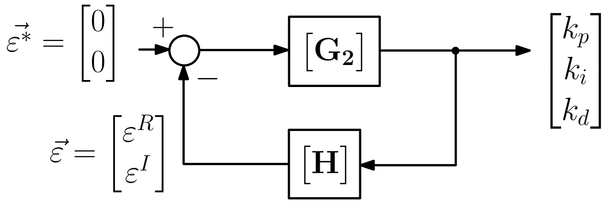

Fig. 3.4. MIMO feedback system resulting from the tuning scheme shown in Fig. 3.1.

Let us assume that, $\mathbf{G_2}$ consist of only some integral terms:

$$\mathbf{G_2(s)} = \begin{bmatrix} g_1/s & g_4/s \\ g_2/s & g_5/s \\ g_3/s & g_6/s \end{bmatrix} \tag{3.11}$$

in which, the terms g_1-g_6 are designed based on the desired behavior for the multi-input multi-output (MIMO) feedback system shown in Fig. 3.4.

Assumption 1

Dynamics of the tuning loop is mostly determined by the LPFs used in Fig. 3.3, with a transfer function G_{lp}. As explained above, the cut-off frequency of the LPFs f_{lp} must be significantly smaller than $2f_c^*$ to have a precise estimation of real and imaginary components of s_x, s_y. Based on this condition, and since the rest of the estimation process is much faster than the low-pass filtering part, assumption 1 represents a reasonable approximation of the system dynamics. Hence, the MIMO open-loop gain under study can be defined as: $\mathbf{H} = \mathbf{G_{lp}} * \mathbf{K^h}$; being, $\mathbf{K^h}$, a 2-by-3 static gain matrix from the PID gains up to the error vector:

$$\mathbf{K^h} = \begin{bmatrix} k_1^h & k_3^h & k_5^h \\ k_2^h & k_4^h & k_6^h \end{bmatrix} = \left. \begin{bmatrix} \frac{\partial \varepsilon^R}{\partial k_p} & \frac{\partial \varepsilon^R}{\partial k_i} & \frac{\partial \varepsilon^R}{\partial k_d} \\ \frac{\partial \varepsilon^I}{\partial k_p} & \frac{\partial \varepsilon^I}{\partial k_i} & \frac{\partial \varepsilon^I}{\partial k_d} \end{bmatrix} \right|_{\mathbf{f=f_c^*}} \tag{3.12}$$

By referring to Fig 3.3, it is possible to write:

$$s_x(j2\pi f) = \frac{1}{1+T(j2\pi f)} s_z(j2\pi f) \tag{3.13}$$

$$s_y(j2\pi f) = -\frac{T(j2\pi f)}{1+T(j2\pi f)} s_z(j2\pi f) \tag{3.14}$$

Then, by substituting (3.13) and (3.14) in (3.7), we can get:

$$\begin{aligned} k_1^h + jk_2^h = \frac{\partial \vec{\varepsilon}(j2\pi f)}{\partial k_p}\bigg|_{f=f_c^*} &= \frac{\partial\big(s_x(j2\pi f)e^{j\phi_m^*/2} - s_y(j2\pi f)e^{-j\phi_m^*/2}\big)}{\partial k_p}\Bigg|_{f=f_c^*} \\ &= s_z(j2\pi f)\,\frac{\partial}{\partial k_p}\Big(\frac{e^{j\phi_m^*/2} + T(j2\pi f)e^{-j\phi_m^*/2}}{1+T(j2\pi f)}\Big)\Bigg|_{f=f_c^*} \end{aligned} \quad (3.15)$$

that can be derived based on the differentiation identities, as:

$$\begin{aligned} k_1^h + jk_2^h &= s_z(j2\pi f)\,\frac{\big(1+T(j2\pi f)\big)\cdot e^{-j\phi_m^*/2}\frac{\partial T(j2\pi f)}{\partial k_p}}{\big(1+T(j2\pi f)\big)^2}\Bigg|_{f=f_c^*} \\ &- s_z(j2\pi f)\,\frac{\big(e^{j\phi_m^*/2} + T(j2\pi f)e^{-j\phi_m^*/2}\big)\cdot\frac{\partial T(j2\pi f)}{\partial k_p}}{\big(1+T(j2\pi f)\big)^2}\Bigg|_{f=f_c^*} \\ &= -j2s_z(j2\pi f)sin(\phi_m^*/2)\,\frac{\frac{\partial T(j2\pi f)}{\partial k_p}}{\big(1+T(j2\pi f)\big)^2}\Bigg|_{f=f_c^*} \end{aligned} \quad (3.16)$$

in which, we can consider a zero angle for the injection signal s_z, thus: $s_z(j2\pi f_c^*) \simeq \delta_z$. Because, as mentioned above, the common reference frame—to which the signals s_x, s_y are projected—is defined by the reference crossover frequency. At this point, if the loop gain T is not known a priori, some approximations around reference crossover frequency may be considered, such as the assumption introduced below.

Assumption 2

The magnitude, and the phase of T around reference crossover frequency (i.e., $|T(j2\pi f_c^*)|$, and $\angle T(j2\pi f_c^*)$) are about 0 dB , and $\phi_m^* - 180$ deg, respectively. This assumption is considered based on the behavior of the tuning loop around the steady-state point. In order to find the rate of change in T with respect to changes in the proportional gain, we can assume a generic plant transfer function G_{pl}, then:

$$\begin{aligned} \frac{\partial T(j2\pi f)}{\partial k_p}\bigg|_{f=f_c^*} &= \frac{\partial\Big(G_{pl}(j2\pi f)\cdot(k_p + \frac{k_i}{j\,2\pi f} + k_d * (j\,2\pi f))\Big)}{\partial k_p}\Bigg|_{f=f_c^*} \\ &= G_{pl}(j2\pi f_c^*) \end{aligned} \quad (3.17)$$

in which, $G_{pl}(j2\pi f_c^*)$ can be found by using Assumption 2, and based on the fact that $T(j2\pi f_c^*) = G_{pl}(j2\pi f_c^*) \cdot \big(k_p + \frac{k_i}{j\,2\pi f_c^*} + k_d \cdot (j\,2\pi f_c^*)\big) \simeq 1e^{j(\phi_m^* - 180)}$.

$$G_{pl}(j2\pi f_c^*) = \frac{1e^{j(\phi_m^* - 180)}}{k_p + \frac{k_i}{j\,2\pi f_c^*} + k_d \cdot (j\,2\pi f_c^*)} \tag{3.18}$$

Thus, by using (3.18) in (3.17) and replacing the result in (3.15), it is possible to find k_1^h, k_2^h. Therefore, the design of the tuning loop is not limited to the cases that a complete model of the system is available.

Similarly, the other components of the matrix $\mathbf{K^h}$ can be found:

$$k_3^h + jk_4^h = \left.\frac{\partial \vec{\varepsilon}(j2\pi f)}{\partial k_i}\right|_{f=f_c^*}, \quad k_5^h + jk_6^h = \left.\frac{\partial \vec{\varepsilon}(j2\pi f)}{\partial k_d}\right|_{f=f_c^*} \tag{3.19}$$

Hence, one can find the MIMO plant transfer function around the operating point (the reference crossover frequency and the reference phase margin). Accordingly, the tuning loop can be designed.

3.3.4 Unfeasible reference phase margin

In order to investigate the feasibility of the tuning goal $\phi_m \to \phi_m^*$ at the reference crossover frequency f_c^*, let us write the phase margin of T in terms of the plant transfer function and the compensator phase, at f_c^*:

$$\begin{aligned}\phi_m(j\,2\pi f_c^*) = 180 + \angle T(j\,2\pi f_c^*) = 180 + \angle G_{pl}(j\,2\pi f_c^*) \\ + \angle\Big(k_p + \frac{k_i}{j\,2\pi f_c^*} + k_d * (j\,2\pi f_c^*)\Big)\end{aligned} \tag{3.20}$$

Thus, the PID gains must be chosen so as to provide the required phase compensation: $\phi_m^* - 180 - \angle G_{pl}(j\,2\pi f_c^*)$. It can happen that, the applied PID provides its maximum allowable phase θ_{max}, but still $\phi_m(j\,2\pi f_c^*)$ is less than ϕ_m^*. In other words, the desired ϕ_m^* is not feasible at the requested crossover frequency f_c^*.

Let us assume that the voltage control loop of a buck converter—that works in parallel with another similar converter—is being tuned. Theoretically, we expect that a certain ϕ_m^* is achievable when both converters are connected to the dc bus; while, when the second is disconnected, ϕ_m^* is no longer feasible at the requested crossover frequency f_c^*. For the estimation technique 1, the infeasibility can be understood from non zero angle difference: $\varepsilon_\phi \neq 0$. In the case of estimation technique 2, the infeasibility can be understood either from non zero real or imaginary component of the error signal: $\varepsilon^R \neq 0$ or $\varepsilon^I \neq 0$. Fig. 3.5 shows an example

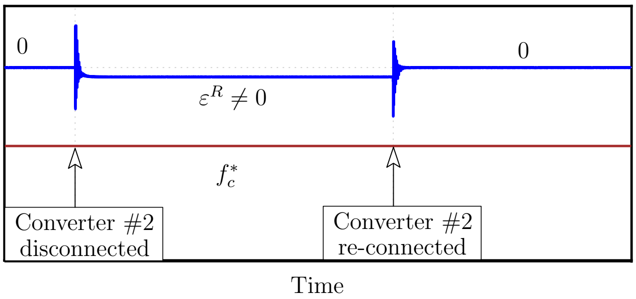

Fig. 3.5. Simulation results of the tuning technique 2 in Fig. 3.3, applied to the voltage loop of a buck converter (converter #1), that works in parallel with a similar converter (converter #2).

of implementing the tuning technique 2 in the voltage loop of converter #1. The control structure and parameters detailed in Section 3.4. As can be seen, ε^R is zero when the two converters work in parallel., and it becomes non-zero when converter #2 is disconnected, showing thus the infeasibility of ϕ_m^* for a single converter case.

This issue can be tackled in several ways. One possibility is to detect the unfeasible phase margin based on the non-zero error vector ($\varepsilon_\phi \neq 0$ in the tuning technique 1 and $|\vec{\varepsilon}| \neq 0$ in the technique 2). As shown in Fig. 3.6, $|\vec{\varepsilon}|$ is processed by an additional regulator (herein just an integral part $k_{ex,1}/s$) to decrease the reference crossover frequency f_c^* up to point at which the reference phase margin is then achievable. This additional loop should be much slower than the tuning loop. It can also happen that the reference phase margin is less than the maximum

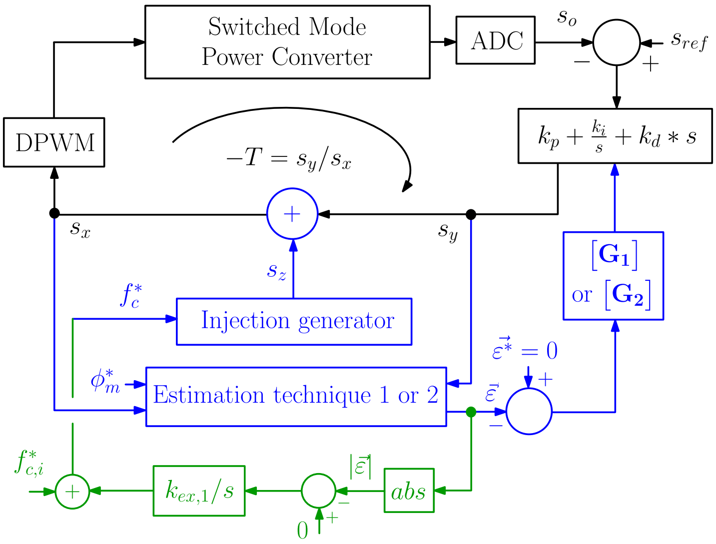

Fig. 3.6. Modified version of the tuning scheme shown in Fig. 3.1, allowing to decrease the reference crossover frequency in order to always reach the reference phase margin.

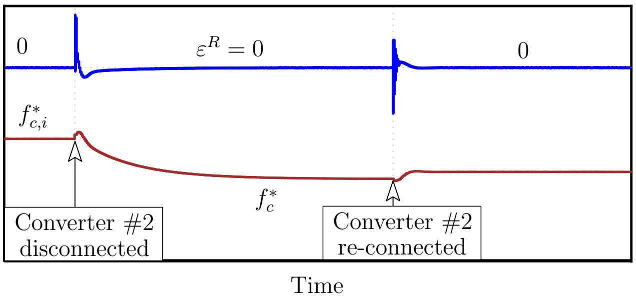

Fig. 3.7. Simulation results of applying the modified tuning technique shown in Fig. 3.6 to the voltage loop of a buck converter (converter #1), that works in parallel with a similar converter (converter #2).

achievable phase margin in a given bandwidth. In this case, ideally, the algorithm should allow to increase the reference bandwidth frequency to an upper bound. This is, however, not possible based on the approach of Fig. 3.6. For the same example in Fig. 3.5, the method shown in Fig. 3.6 is applied, and the results are shown in Fig. 3.7. As can be seen, although this additional loop successfully decreases the initial reference $f^*_{c,i}$ to make ϕ^*_m achievable at f^*_c, but, when the converter #2 is reconnected again to the bus, the system fails to retrieve the initial f^*_c. This issue can be solved by looking also at the angle of the error vector $\angle\vec{\varepsilon}$. Then, f^*_c can be either increased or decreased based on the sign of $\angle\vec{\varepsilon}$. This is similar to the common-practice of maximum power point tracking techniques addressed in the literature [87], that, however, bring with some non-linearities.

Herein, we propose to use the scheme shown in Fig. 3.8 in order to tackle the issue

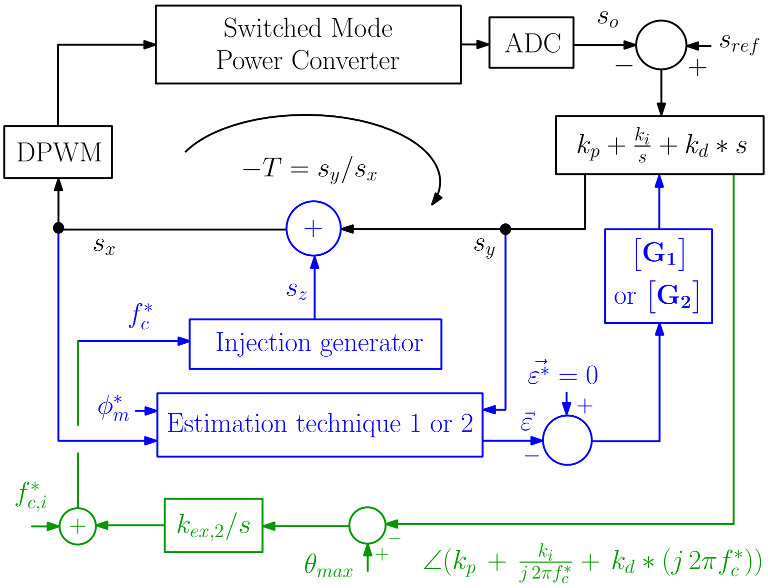

Fig. 3.8. Modified version of the tuning scheme shown in Fig. 3.1, allowing to track maximum reachable bandwidth, under achievement of the reference phase margin.

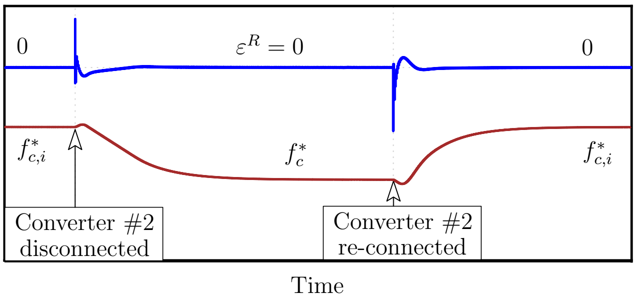

Fig. 3.9. Simulation results of applying the modified tuning technique shown in Fig. 3.8 to the voltage loop of a buck converter (converter #1), that works in parallel with a similar converter (converter #2).

of unfeasible reference phase margin. Based on this method, f^*_c can be properly adjusted (by including an integral part $k_{ex,2}/s$), in order to allow the loop T to always achieve the desired phase margin ϕ^*_m. To better clarify this aspect, let us consider two possible cases: i) when the maximum achievable phase margin is less than ϕ^*_m, then f^*_c will be decreased to make the reference phase margin feasible, ii) when the maximum achievable phase margin is more than the reference ϕ^*_m, then f^*_c will increase to a given upper bound. Thus, the loop under study will operate at its maximum allowable bandwidth, under achievement of the reference phase margin. It is also worth mentioning that, this external loop must be much slower than the tuning loop so that f^*_c can be almost constant during the transient of tuning loop. For the same example in Fig. 3.5, the tuning scheme shown in Fig. 3.8 is applied, and the results are shown in Fig. 3.9. As can be seen, when the converter #2 is disconnected, the initial reference $f^*_{c,i}$ is decreased so that ϕ^*_m is achievable at f^*_c. On the other hand, when the converter #2 is reconnected again to the bus, the system successfully retrieves the initial f^*_c, meaning that the loop T is always operating at its maximum allowable bandwidth, under achievement of the reference phase margin.

3.3.5 Application to the dc microgrid power converters

The DER converters operating in a dc microgrid usually involve multiple control loops. The proposed technique can be applied to the PID regulator of any loop within power converters, as long as that loop can be assumed as a linear time invariant (LTI) system. An example of DER converters operating in dc microgrid is shown in Fig. 3.10. As can be noticed, it includes the inductor current and the output voltage loops, that can be designed based on standard procedures, as described in the literature, for example, in [39]. In addition, the droop loop is used to address different needs of dc microgrids such as power sharing [18]. The

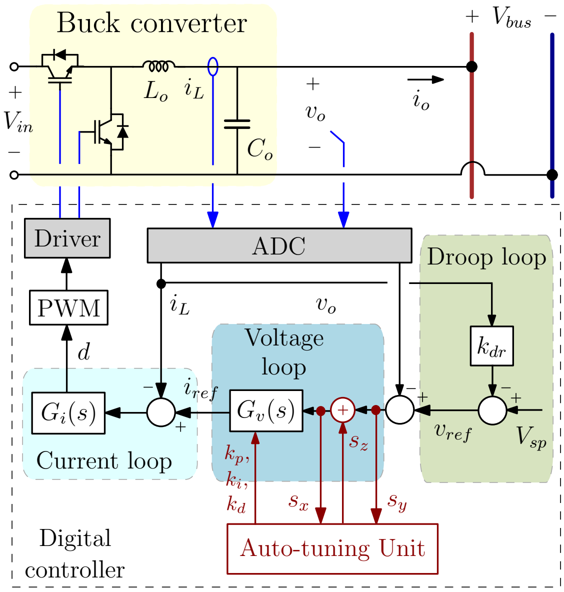

Fig. 3.10. Droop-controlled DER converter equipped with the proposed auto-tuning technique addressed in Fig. 3.8.

droop loop adopted here modifies the output reference voltage as:

$$v_{ref} = V_{sp} - k_{dr} \cdot i_o \tag{3.21}$$

where v_{ref} is the output voltage reference, V_{sp} is the dc bus voltage set point at no-load condition, k_{dr} is the droop coefficient, and i_o is the output current. In this case, due to the buck topology, the output current i_o can be replaced by the inductor current i_L, as they are equal in the steady state, and no additional sampling is needed. The droop coefficient and the voltage set point used in this work are chosen based on the well-known droop control design methods in the literature, such as [88], [89].

3.4 Case Study and Experimental Results

The prototype considered in this work is shown in Fig. 3.11, which emulates an islanded dc microgrid. It consists of three droop-controlled buck converters, each implementing the structure shown in Fig. 3.10, with system parameters listed in Table 3.1.

The converters have equal droop coefficients $k_{dr} = 1.33\,\mathrm{V/A}$, and the voltage set-point is $V_{sp} = 200\,\mathrm{V}$. Also, the current regulator $G_i(s)$ is the same for all the three converters (the proportional term=0.2, and the integral term=8). But, the voltage regulators $G_v(s)$ are chosen differently. In the voltage regulator of converter #2,

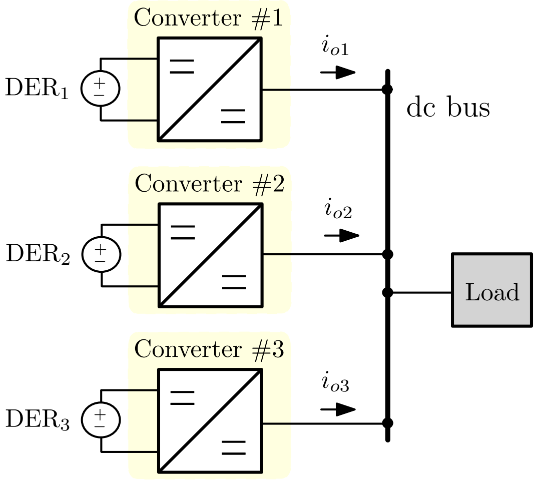

Fig. 3.11. The laboratory setup emulating an islanded dc microgrid. Each power converter implements the structure shown in Fig. 3.10.

the proportional term is 0.084, and the integral term is 870, while for converter #3 the proportional and the integral terms are 0.042 and 435, respectively. $G_v(s)$ of converter #1— in which the tuning technique is implemented— is a PID with the initial proportional, integral, and derivative terms equal to 0.084, 870, and 0.00001, respectively. In this work, for brevity, only the experimental validations of the estimation technique 2 (shown in Fig. 3.3) are reported.

The proposed adaptive tuning algorithm is used to tune the PID parameters of the voltage regulator $G_v(s)$ of converter #1 in the setup shown in Fig. 3.11, where the load is just a resistor $R_L = 150\,\Omega$. In this test, the tuning goal is to achieve $f_c^* = 500\,\text{Hz}$, and $\phi_m^* = 75$ deg, for the droop loop. The tuning matrix $\mathbf{G_2}$ is designed based on the assumptions and approximation mentioned in Section 5.5.C. In particular: $g_1, g_4, g_6 \simeq 0$, $g_2 = 2.5$, $g_3 = 6250$, $g_5 = 0.00023$. Experimental results of the real and imaginary components of the tuning-error vector are shown in Fig. 3.12. As can be seen, within a short time after starting the tuning, both ε^R,

Parameter	Symbol	Value
Input voltage	V_{in}	380 V
Nominal bus voltage	V_{bus}	200 V
Nominal power	P^{nom}	3 kW
Output side inductance	L_{out}	1.6 mH
Output side capacitance	C_{out}	110 µF
Switching frequency	f_{sw}	12.5 kHz
Load Resistance	R_L	150 Ω

Table 3.1: Parameters of the setup shown in Fig. 3.11

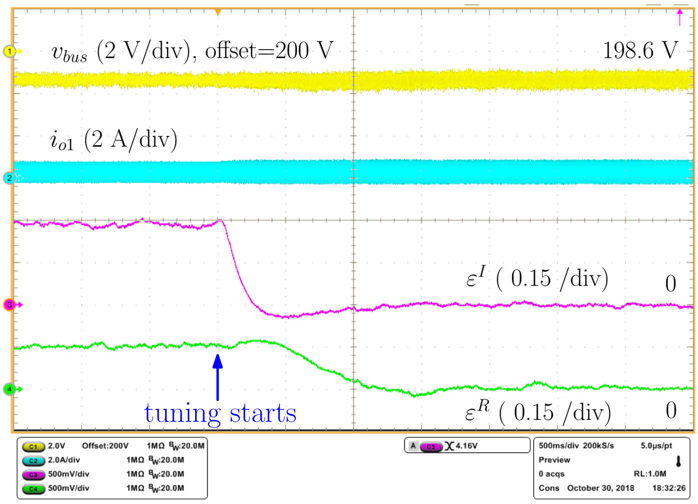

Fig. 3.12. Experimental results of tuning $G_v(s)$ of converter #1, showing the convergence of both ε^R, ε^I to zero, which means that the desired stability margins are achieved. Time scale: 0.5 sec/div.

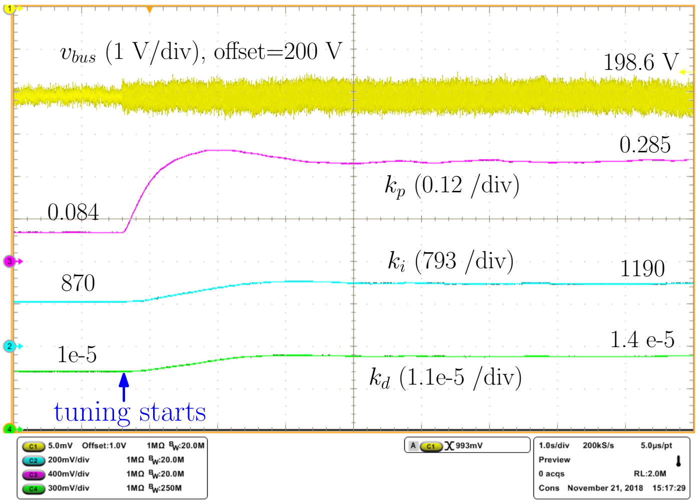

Fig. 3.13. Experimental results of tuning $G_v(s)$ of converter #1, showing the required changes in the PID gains in order to obtain the desired stability margins. Time scale: 1 sec/div.

ε^I converge to zero, confirming the correct achievement of the desired crossover frequency and phase margin. Fig. 3.13 shows the experimental results of the $G_v(s)$ gains of converter #1. As can be seen, the PID gains vary from the initial values mentioned above, to the final, steady-state values of 0.285, 1190, and 0.000014, respectively, for the proportional, integral, and derivative terms. It is also worth highlighting that, the bus voltage ripple, due to the tuning perturbation, stays within a reasonably small range (less than 0.2% of the nominal value). This means that, the small-signal perturbation amplitude δ_z is designed in such a way that the tuning process does not disturb the normal operation of the system (herein, $\delta_z = 0.4V$).

In order to evaluate the correctness of the achieved PID gains, the actual stability margins of the droop loop, before and after tuning, are found by means of the Sweep Frequency Response Analysis (SFRA) tool [79]. Based on SFRA, the droop loop of converter #1 in Fig. 3.11 is perturbed frequency-by-frequency. Then, by evaluating the Fourier Transform of the inputs and outputs, the frequency response is calculated, and used to find the stability margins.

The analytical model of the droop of converter #1 before tuning, compared with the experimentally-measured frequency response is shown in Fig. 3.14. Similarly, after tuning the $G_v(s)$ gains, the analytical model of the droop loop of converter #1 together with the experimental measurement results is shown in Fig. 3.15. In both cases, good matching between analytical models and experimental measurements can be observed, tha confirms the correctness of the performed analysis. It is also worth noticing that, the crossover frequency and phase margin of the droop loop, before applying the tuning are respectively, $f_c = 365\,\text{Hz}$, and $\phi_m = 65$ deg. After tuning, on the other hand, the calculated stability margins are $f_c = 530\,\text{Hz}$, and $\phi_m = 76$ deg, which are almost equal to the reference stability margins (in this experiment: $f_c^* = 500\,\text{Hz}$, and $\phi_m^* = 75$ deg). Hence, both of the conditions 1 and 2, mentioned in Section 3.2 are satisfied: $f_c \rightarrow f_c^*$, with around 5% error, and $\phi_m \rightarrow \phi_m^*$, with around 1% error.

In order to verify the performance the proposed tuning technique shown in Fig. 3.8, in the case that an unfeasible phase margin is desired, the same setup as Fig. 3.11 has been considered. To make the situation slightly different, the load subsystem is changed to a 1.5 kW CPL. The same tuning matrix $\mathbf{G_2}$ as the previous experiment is also used here. Experimental results of this test are shown in Fig. 3.16. As

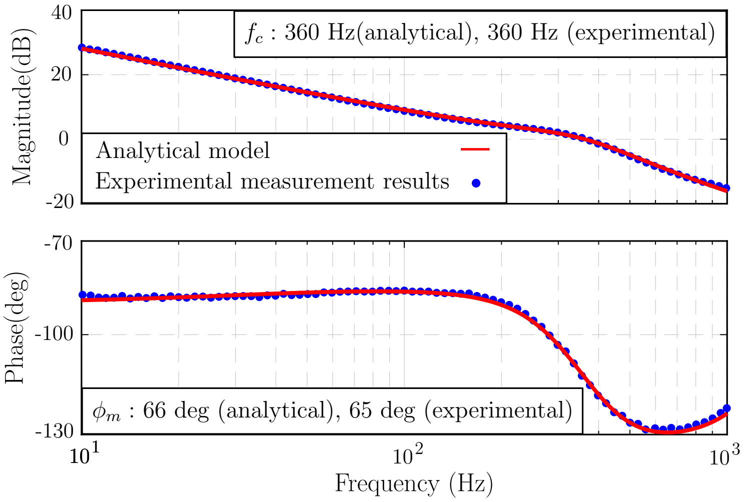

Fig. 3.14. Analytical model and experimentally-measured (SFRA) frequency responses of the droop loop of converter #1, before tuning $G_v(s)$.

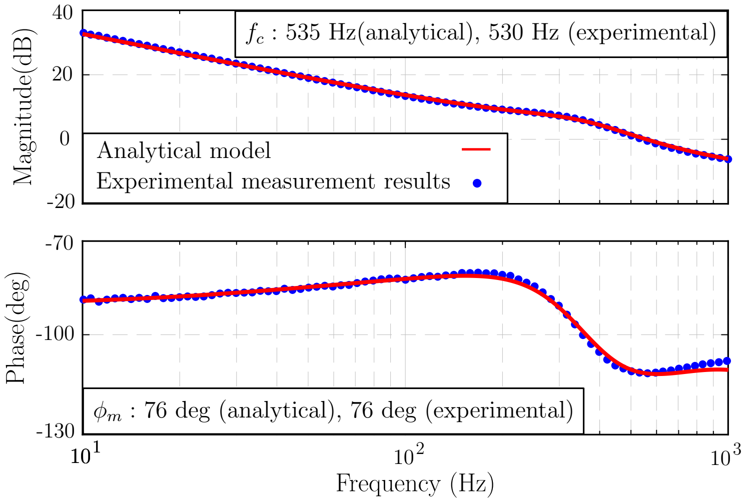

Fig. 3.15. Analytical model and experimentally-measured (SFRA) frequency responses of the droop loop of converter #1, after tuning $G_v(s)$.

can be seen, the error vector $\vec{\varepsilon}$ is initially non-zero; meaning that the desired phase margin for the droop loop ($\phi_m^* = 70$ deg) is not achievable at the reference crossover frequency $f_c^* = 600\,\text{Hz}$. In this case, because of the specific operation condition of the MIMO loop as addressed by (3.15), just the imaginary part of the error ε^I depends on the phase, and shows non-zero initial value. After activating the external loop in Fig. 3.8 to track the maximum allowable bandwidth, f_c^* is decreased to around 470 Hz, thus, allowing the droop loop to achieve the desired reference phase margin $\phi_m^* = 70$ deg.

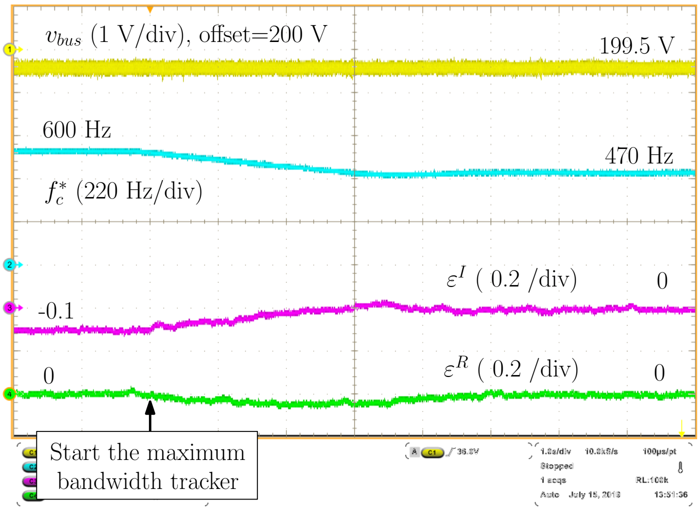

Fig. 3.16. Experimental results of the error vector and the reference crossover frequency, before and after activating the external loop in Fig. 3.8, that tracks the maximum allowable bandwidth. Time scale: 1 sec/div.

3.5 Summary

Two on-line tuning techniques for the dc microgrid power converters are discussed in this chapter. Based on these techniques, a small-signal perturbation at the desired crossover frequency is injected into a generic control loop of power converters. Then, the signals right before, and right after the perturbation point are processed to define an tuning error. The PID gains of the compensator are then tuned to make the error signal converge to zero, i.e. to reach the reference crossover frequency and phase margin. In addition, the situation of unfeasible reference phase margin at a given reference crossover frequency, is also taken into account. The proposed tuning method is applied to a laboratory setup composed of three droop-controlled converters. According to the reported experimental results, the voltage regulator parameters are adjusted appropriately, leading the tuning error reach to zero. Besides, the experimental frequency responses of the converter, before and after tuning show that, the desired stability margins for the droop loop are achieved with a good accuracy.

Chapter 4

Applying PRBSs for loop gain identification and adaptive tuning

4.1 Introduction

The stability monitoring and autotuning techniques described in Chapter 2 and Chapter 3 are very simple, do not need lengthy data measurements, and also do not need an auxiliary processor in the implementation. However, they just provide us with the control loop behavior around 0 dB crossing frequency and 180 deg crossing frequency (i.e., they just give us the stability margins). Although this can be enough for stability studies, but it does not provide us with the control performance of a generic loop over the entire bandwidth. An example of this issue can be a loop with multiple 0 dB crossover frequencies, which can be a limitation, or can add further complexity to stability monitoring addressed in Chapter 2. Thus, in order to have a full picture about the control performance of a generic loop over the entire bandwidth, we need to measure the whole frequency response of that loop.

As mentioned in Chapter 1, several approaches are proposed to measure the loop gains of digitally-controlled power converters. The existing methods are based on exciting the system either by the frequency sweep of a narrow-band signal, such as sine waves [40, 41], or by a wide-band signal, such as impulse [42], or PRBSs [43–45]. Consequently, the loop gain is obtained by applying the fast Fourier transform (FFT). The main advantage of wide-band perturbation is that, it can excite multiple frequency components at once, without needing the time consuming frequency sweep used in the narrow-band case. This significantly reduces the measurement time.

Among many possible wide-band injections [44], PRBS is interesting for switched-mode power supply (SMPS) applications, because of the frequency resolution, the short time required for identification, and the possibility of adjusting the injection bandwidth. Also, the peak factor is very low due to the binary nature, which makes it well-suited for sensitive systems that require a perturbation with small amplitude [37]. Furthermore, it can be generated simply, by means of feedback shift registers.

Details of PRBS-based identification techniques is given in the literature [43,83,90]. These studies assume a generic control loop of digitally-controlled power converters as an LTI system. Fig. 4.1 shows a generic loop T_s within a power converter, in which a small-signal PRBS u is injected in the feedback loop. For such an LTI system, the sampled behavior can be described based on the discrete-time convolution concept [91]:

$$s_{out}(n) = \sum_{i=1}^{\infty} h(i)u(n-i) + s_n(n) \tag{4.1}$$

where $s_{out}(n)$ is the sampled output signal, $u(i)$ is the sampled input perturbation signal (PRBS), $h(i)$ is the system impulse response, and $s_n(n)$ is the disturbance during that sampling period, that can be the switching and quantization noise.

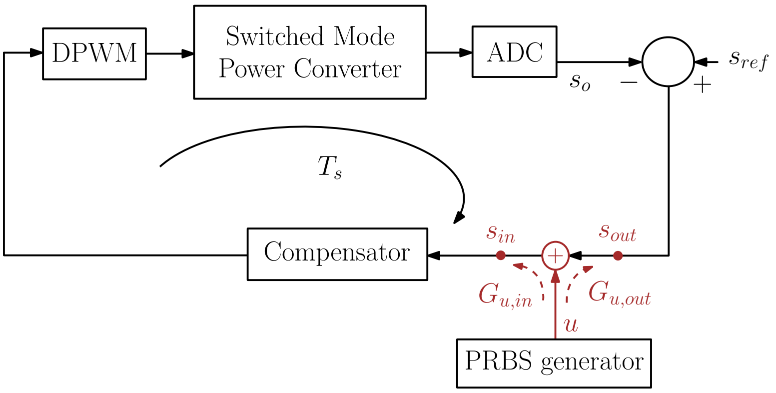

Fig. 4.1. Loop gain measurement by injecting a PRBS signal u at any point of the digital feedback loop, for example, before the compensator.

The cross correlation of the perturbation signal u and the output signal s_{out} can be defined as follows:

$$R_{u,out}(k) = \sum_{n=1}^{\infty} u(n)s_{out}(n+k) = \sum_{n=1}^{\infty} h(n)R_{u,u}(k-n) + R_{u,n}(k) \tag{4.2}$$

where $R_{u,u}(k)$ represents the autocorrelation of perturbation signal u, and $R_{u,n}(k)$ is the cross correlation of the perturbation signal u and the noise signal s_n. If the PRBS is a good approximation of the white noise, then the following two properties hold [90]:

$$R_{u,u}(k) \simeq \delta(m), \quad R_{u,n}(k) \simeq 0. \tag{4.3}$$

Of course, if the perturbation signal is a pure white noise, then the approximations in (4.3) become accurate. Fig. 4.2a shows a pure white noise between -1 and 1, and Fig. 4.2b shows a single period of PRBS. Their corresponding autocorrelation functions $R_{u,u}(k)$ are shown in Fig. 4.2c and Fig. 4.2d, respectively. As can be seen, the auto-correlation of a PRBS is very similar to a delta function. Thus,

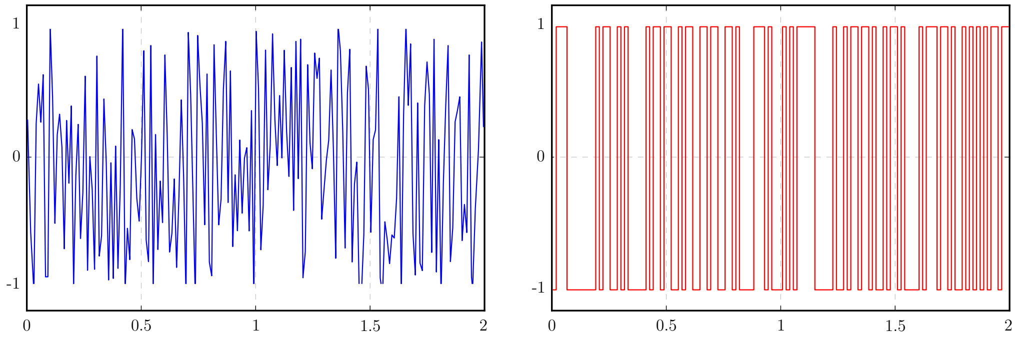

(a) A pure white noise

(b) Single period of a PRBS

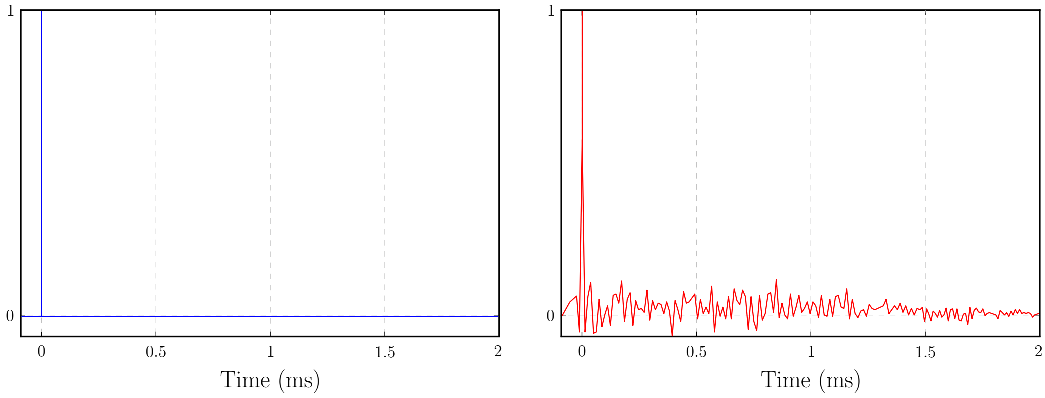

(c) Autocorrelation of the white noise

(d) Autocorrelation of the PRBS

Fig. 4.2. A pure white noise and a PRBS, together with their corresponding autocorrelations.

some of the probable errors in the results of PRBS-based identification will be due to the difference between autocorrelation of PRBS (Fig. 4.2d) and the ideal delta function (Fig. 4.2c). This figures report a continuous-time example. Similar conclusion can be made for the case of discrete-time [43].

By using (4.3) in (4.2), the cross correlation equation becomes the discrete-time impulse response of the system:

$$R_{u,out}(k) \simeq h(k). \tag{4.4}$$

Consequently, by evaluating the discrete Fourier transform (DFT) of the cross correlation results, we can transform the obtained impulse response to the frequency response of $G_{u,out}$ shown in Fig. 4.1.

$$G_{u,out}(jw) \simeq DFT\{R_{u,out}(k)\}. \tag{4.5}$$

Similarly, $G_{u,in}$ can also be found by calculating the DFT of the cross correlation between the perturbation signal u and the loop input signal s_{in}, as $G_{u,in}(jw) \simeq DFT\{R_{u,in}(k)\}$. Finally, the frequency response of the loop under study T can be evaluated as follows:

$$T(jw) = \frac{G_{u,out}(jw)}{G_{u,in}(jw)}. \tag{4.6}$$

An important property of PRBSs, which is less elaborated in the literature, is their controllable frequency content. In other words, it is possible to generate several PRBSs that each have different frequency components [92]. This feature is particularly interesting for multiple-input multiple-output (MIMO) system identification, where several orthogonal injections are required. Multiple orthogonal PRBS injection is discussed in some studies. For example, in [92] and [74], the stability of ac grid-connected systems is investigated by performing on-line measurements of dq domain grid impedance. To this end, two orthogonal PRBSs, are injected into d and q axes. Thus, the dq impedances are simultaneously measured in a single measurement cycle, and the operating conditions of the system remain effectively constant during the measurement. Similarly in [93], authors propose the use of periodic ternary sequences for dq grid-impedance measurements, considering the probable non-linearities involved in power-electronics systems. In [32], multiple orthogonal PRBSs are used to measure the converters output impedances in a multi-converter system to investigate the stability conditions based on impedance. However, the necessity and the application of multiple orthogonal PRBSs in simultaneous identification of several control loops within a DER converter are not specifically addressed.

This work aims to extend the same concept described in [37,46], from a single-loop identification to the simultaneous identification of multiple loops within dc microgrid power converters. When injecting the PRBS in a generic control loop, its amplitude must be properly set, based on the signal-to-noise ratio (SNR) in order to excite the dynamics of that loop over its entire bandwidth. Usually, the control loops of a multi-loop system, have different SNR levels, and different bandwidths. So, the injection amplitude at each loop, must be adjustable based on the SNR level of that loop, and independently from the other loops. To this end, multiple orthogonal PRBSs can be injected into different control loops, at the same time. This will allow to independently set the injection amplitudes and thus, gives the possibility to simultaneously identify several loops. As the injections excite the system at different frequency components, simultaneous identification of multiple loops can be performed, without the need for cross-correlation or other signal-processing steps, as discussed in [43]. Since all the identifications are achieved in only one measurement cycle, the overall measurement time is relatively low [92]. Besides, the system operating conditions remain effectively constant during the measurements, which is of paramount importance for accurate monitoring and tuning actions. To summarize, this work proposes to apply multiple orthogonal PRBS injections in simultaneous monitoring of several control loops within dc microgrid power converters. Besides, the necessity of having orthogonal perturbations for the simultaneous identification of several loops is experimentally shown. Finally, an adaptive tuning algorithm is presented to adjust the digital compensator based on the identification results, in order to reach certain dynamic performances.

The remainder of this chapter is organized as follows. Section 4.2 presents the basics of the orthogonal PRBS generation, and its application to dc microgrid power converters. Section 4.3 describes the system under study and the corresponding small-signal models. In Section 4.4, an experimental prototype of a dc microgrid is implemented, and the converters control loops are identified simultaneously, by using orthogonal PRBSs. The identification results are then used in adaptive tuning of the voltage regulator parameters, in order to reach a certain desired dynamic performance.

4.2 Simultaneous frequency response measurement of multiple control loops

This work aims to measure the frequency responses of multiple control loops, by simultaneous injection of orthogonal PRBSs. Although in some cases, there may be no strict need to multiple PRBSs, i.e., a single PRBS might be enough to identify several loops, depending on their specific transfer functions and their SNR levels. An example is the injection of a PRBS at the most external loop, and measuring several loops by separately choosing the input-output points of each loop, required for the FFT process. However, this is not always possible. In the outlined scenario, if the outer loop is much slower than the inner loops—which is normal in multi-loop systems—then, the amplitude of the PRBS injected at the most external loop is not enough to excite the inner loops at high frequency ranges. While, it successfully identifies the outer loop over its bandwidth. This aspect is further discussed in Section 4.4. Therefore, ideally, the PRBS amplitude should be adjustable depending on the loop under investigation, and independently from the other loops. In this context, presence of a separate PRBS at each loop, shows its merit.

4.2.1 Generating orthogonal excitations

Orthogonal PRBSs can be generated in different ways [94, 95]. Herein, the algorithm proposed in [94] is adopted, which is based on feedback shift registers, as can be seen in Fig. 4.3. The same algorithm is used in [92] for generating two orthogonal PRBSs. While, herein, the concept is extended to generate M orthogonal PRBSs, in the following three steps [96]:

(i) On top of Fig. 4.3, an N-bit-length shift register is used to generate a periodic PRBS. As described in [94], the initial state of the register can be any value except 0,0,. . . ,0. Then, by means of a feedback term, $2^N - 1$ possible combinations of the N-bit binary number are synthesized. The feedback term, herein, is built by using the XOR operation. Hence, the first sequence, PRBS_1, also known as maximum-length binary sequence (MLBS), is generated. A comprehensive list of possible feedback connections to produce MLBSs can be found in [94]. The generated MLBS is then, mapped between $-K_{MLBS}$ and K_{MLBS}, in order to produce a symmetrical signal, with an average close to zero. Based on the number of bits, the MLBS length can be written as:

$$l_{MLBS} = 2^N - 1 \tag{4.7}$$

The energy spectrum of MLBS is shown in Fig. 4.4. As can be noticed, the energy spectrum follow a $sinc^2$ function, in which the power drops to zero dB at the generation frequency of the sequences, which can be defined as follows:

$$f_{gen} = f_s / k_{gen} \tag{4.8}$$

where f_s is the sampling frequency at each loop, that herein, is considered equal to the switching frequency of the converters ($f_s = f_{sw}$). The factor k_{gen} is a positive integer defining the desired measurement bandwidth. Choice of k_{gen} is further detailed later in this Section. The r-th component of the MLBS spectrum is:

$$f_r^{MLBS} = \frac{f_{gen}}{2^N - 1} \cdot r, \qquad r = 1, 2, 3 \ldots \tag{4.9}$$

(ii) There are several ways to generate another PRBS, that is orthogonal to PRBS$_1$ [94]. For instance, in Fig. 4.3, a 2-bit shift register—whose initial value can be either 0,1 or 1,0— is used to produce the sequence 0,1,0,1, . . . , or 1,0,1,0, ... By adding the repeated sequence 0,1,0,1, . . . , to the original MLBS, we are actually doubling the MLBS, and inverting every

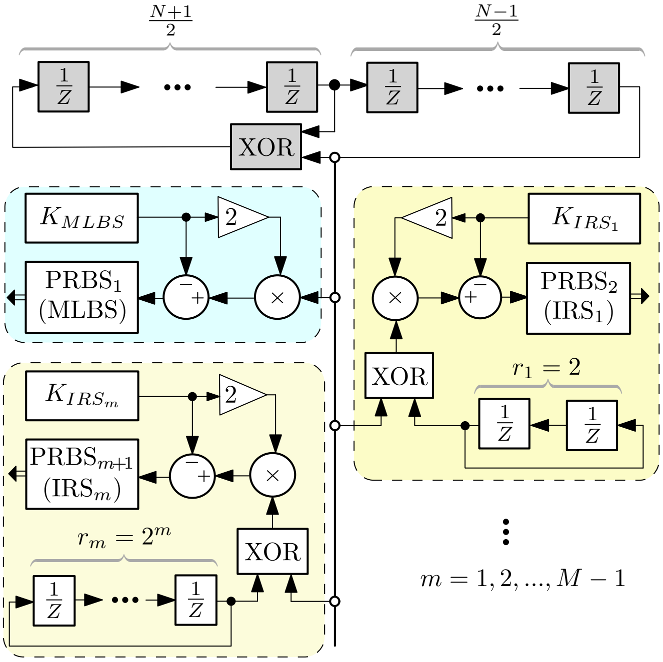

Fig. 4.3. Generating M orthogonal PRBS signals (including an MLBS and $M-1$ IRS signals), by using an N-bit feedback shift register. N is an odd integer in this example.

other digit of the doubled sequence. At the simplest case, for $N = 2$, a possible MLBS is the periodic sequence: 1,1,0,1,1,0, ..., which after XOR with 1,0,1,0, ..., creates the new sequence 0,1,1,1,0,0,0,1,1,1,0,0, ... As can be noticed, the new sequence is the double of MLBS, having inverted every other digit of it. So, the length of the new sequence, that is usually referred to as inverse-repeated sequence (IRS), is twice the length of the original MLBS. This, in frequency domain, is equivalent to excite the half of each frequency component of the original MLBS. Thus, and because of the inversion property [94], the new signal PRBS$_2$ does not have energy at same frequencies as PRBS$_1$, as shown in Fig. 4.4. In other words, IRS$_1$ (PRBS$_2$) is orthogonal to MLBS (PRBS$_1$). Finally, IRS$_1$ is mapped between $-K_{IRS_1}$ and K_{IRS_1}, in order to produce a symmetrical signal with an average close to zero.

(iii) Similarly, the sequence 0,0,1,1,0,0,1,1, ... can be added to the original MLBS in order to generate IRS$_2$ (PRBS$_3$), that is orthogonal to the two previous signals PRBS$_1$, PRBS$_2$. The same procedure can be repeated to generate an arbitrary number (M) of orthogonal PRBS signals (MLBS and $M-1$ IRS sequences). As can be noticed in Fig. 4.4, the produced PRBS sequences have power at different frequencies and, thus, they are uncorrelated over their common period, which is l_{IRS_m}. The length of each IRS sequence can be written as follows:

$$l_{IRS_m} = l_m * (2^N - 1), \qquad m = 1, ..., M-1 \tag{4.10}$$

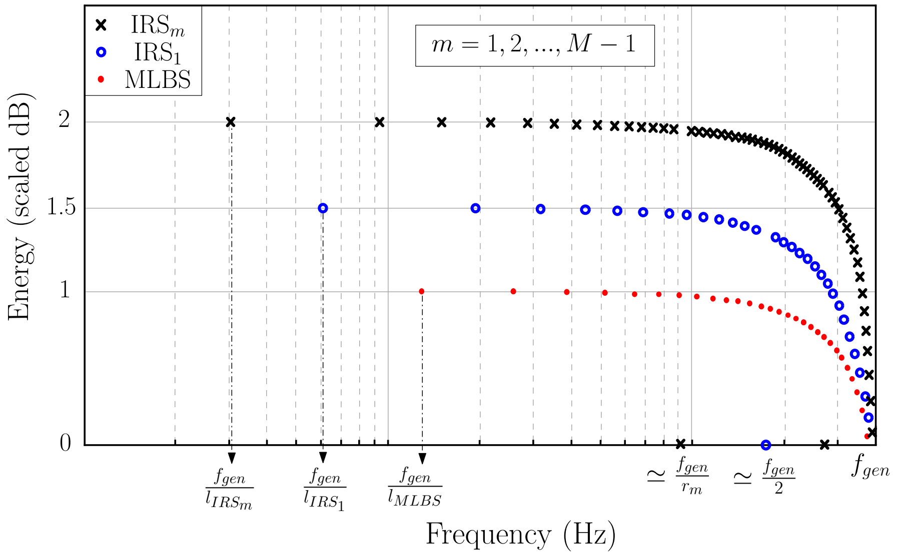

Fig. 4.4. Energy spectra of the PRBSs generated based on the algorithm shown in Fig. 4.3. The generated PRBSs are orthogonal over their common period l_{IRS_m}.

in which, $l_m = 2^m$. Based on Fig. 4.4, the r-th component of each IRS spectrum is:

$$f_r^{IRS_m} = \frac{f_{gen}}{l_{IRS_m}} \cdot (2r-1), \qquad r = 1, 2, 3, \ldots \tag{4.11}$$

Notably in (4.11), for any value of m and r, the frequency components of different PRBSs do not overlap each other.

It is worth mentioning that in Fig. 4.4, the power spectra of the IRS signals have an instant drop to zero at $\frac{f_{gen}}{r_m}$ and its harmonics.

A minor drawback of this algorithm is the fact that, when generating each new IRS signal that is orthogonal to all the existing PRBSs, we go down with a factor of two in the frequency domain, as can be seen in Fig. 4.4. This implies an increase in the identification time by a factor of two for each additional loop. This is, however, still much faster than performing one-by-one measurements of several loop gains [44].

Regarding the PRBS generation parameters, it is worth noticing that, *1*) choice of N is a tradeoff between the number of identified points, and the identification speed. A smaller N, according to (4.10) will lead to the shorter length of MLBS and IRS, thus a faster identification can be achieved. On the other hand, if we need a higher frequency resolution, according to (4.9), we should choose a higher N [92]. *2*) k_{gen} is chosen according to the desired measurement bandwidth. For identifying high-bandwidth loops, f_{gen} must be high, then based on (4.8), k_{gen} must be low. On the other hand, for the slow loops, k_{gen} should be high, so that, f_{gen} is low, and the first component of the identified frequency response (f_{gen}/l_{MLBS}) locates in a lower range. In addition, it is important to notice that k_{gen} must be at least two, to avoid aliasing. According to these three requirements, the value of k_{gen} should be chosen [92, 94]. *3*) In general, all the PRBS amplitudes are different ($K_{MLBS} \neq K_{IRS_1} \neq K_{IRS_m}$), because the perturbations are injected in multiple loops with different SNR levels. Thus, ideally, each amplitude must be adjustable, independently form the others. More details on the choice of perturbation amplitudes is given in Section 4.4.

4.2.2 Using orthogonal PRBSs in dc microgrid power converters

Let us suppose that, there exist M generic control loops within a DER converter operating in the dc microgrid. In this work, each loop is assumed as a linear time invariant (LTI) system. As mentioned above, this chapter proposes to use

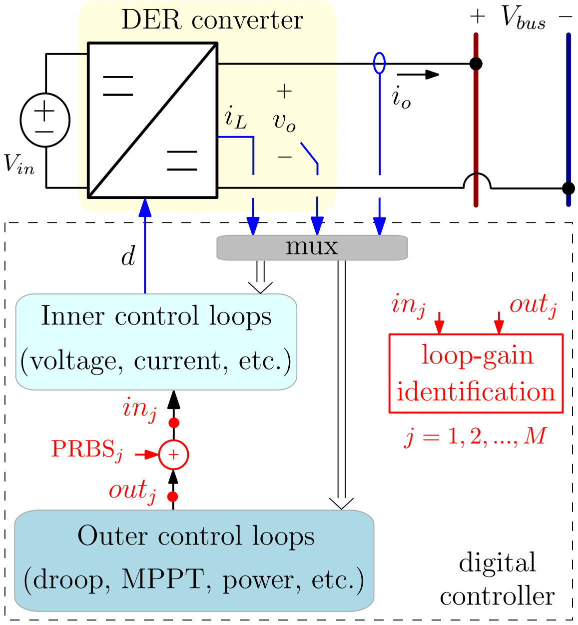

Fig. 4.5. Applying M orthogonal PRBSs to simultaneous identification of M control loops within a dc microgrid power converter.

M orthogonal PRBSs to monitor the frequency responses of all the loops within a dc microgrid power converter, simultaneously. The orthogonal PRBSs generated by the algorithm shown in Fig. 4.3, are applied to the multiple control loops of a DER converter, as displayed in Fig. 4.5. As can be noticed, in addition to the inner current and voltage loops, the DER converter can, in general, involve some outer control loops, such as the droop loop, the power loop, the virtual impedance loop, etc [26]. Therefore, the number of control loops within a dc microgrid power converter will determine M in Fig. 4.3 and Fig. 4.4. As mentioned above, the higher M leads to the higher measurement length, and thus, the higher identification time.

4.2.3 Loop gain measurement in multiple converters

As mentioned above, dc microgrid is a multi-converter environment. So, the perturbation injected in a certain converter can also have an effect on the other converters connected to the common dc bus [72]. Therefore, if several converters inject perturbations at the same time, the resulting perturbations on the dc bus can combine and lead to a reduction in the precision of the identified models, as discussed in chapter 2. This issue can be managed in various ways, depending on the application.

One possible way is to force the PRBSs of each converter to be not only uncorrelated to each others, but also uncorrelated to the PRBSs of the parallel converters. This, of course, means to have a primary assumption when setting up the monitoring units of the converters, or to have a communication between different converters. In addition, for high number of parallel converters, each identifying M control loops, the number of orthogonal sequences largely increases. This, as mentioned above, will highly increase the identification and processing time, that is not desirable.

Herein, a supervisory control is adopted based on which, different injection time slots can be assigned to different converters. Hence, the monitoring units of multiple converters are activated sequentially and without overlaps in their injection periods.

4.3 Case study

The islanded dc microgrid considered in this work is shown in Fig. 4.6. It consists of three buck converters with similar system parameters as listed in Table 4.1. The load subsystem, herein, consists of only a resistive part R_L. Each buck converter implements the structure shown in Fig. 4.7. As can be seen, three control loops are included: the inductor current loop, the output voltage loop, and the droop control loop. The current and the voltage regulators are designed based on standard procedures, as described in the literature, for example, in [39].

In particular, the current loop bandwidth is chosen around one-tenth of the switching frequency $f_{sw} = 12.5\,\text{kHz}$ (herein 1000 Hz). Then, the voltage loop bandwidth

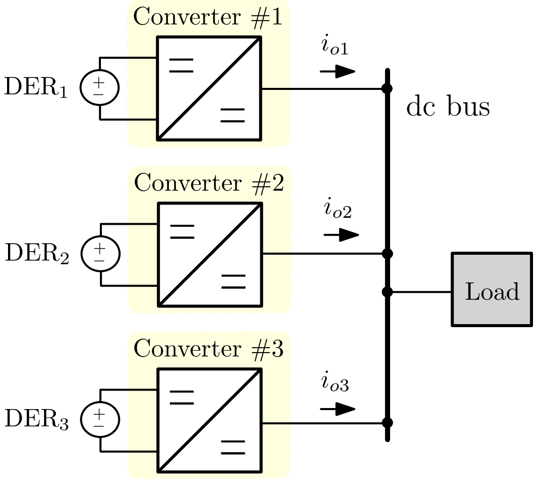

Fig. 4.6. The dc microgrid model under study.

Parameter	Symbol	Value
Input voltage	V_{in}	380 V
Nominal bus voltage	V_{bus}	200 V
Nominal power	P^{nom}	3 kW
Output side inductance	L_{out}	1.6 mH
Output side capacitance	C_{out}	110 µF
Switching frequency	f_{sw}	12.5 kHz
Load Resistance	R_L	150 Ω

Table 4.1: Parameters of the setup shown in Fig. 4.6

is set to around half of the current loop bandwidth. As listed in Table 4.2, all the converters have equal current regulators. But, the voltage regulator of converter #3 is different from those of converters #1 and #2, as it can happen in a real dc microgrid that different converters have different parameters.

The converters also implement the droop controller, which is widely used in the literature [17, 18] to address various needs of dc microgrids (e.g., bus voltage regulation and power sharing among different sources). The droop loop adopted in

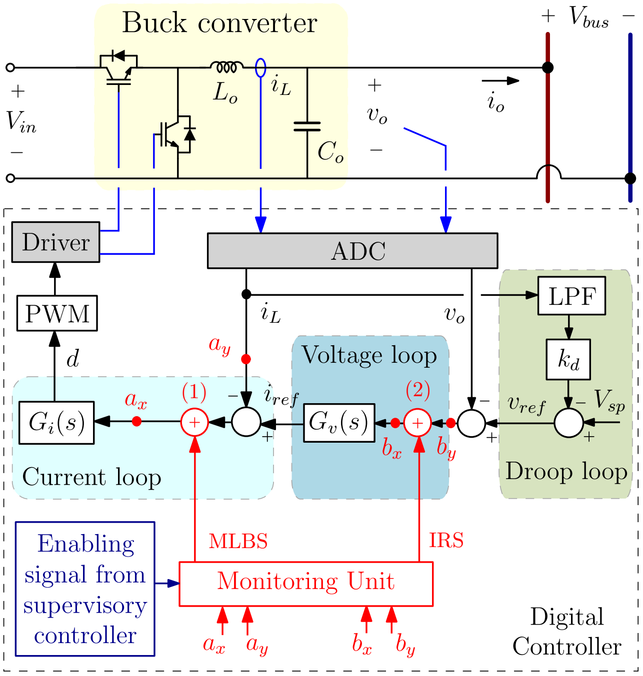

Fig. 4.7. Structure of the DER converters considered in Fig. 4.6. In this work, the current and the droop control loops (of converter #1) are simultaneously monitored.

this work modifies the output reference voltage as:

$$v_{ref} = V_{sp} - k_d \cdot i_o \tag{4.12}$$

where v_{ref} is the output voltage reference, V_{sp} is the dc bus voltage set point at no-load condition, k_d is the droop coefficient, and i_o is the output current. It is worth highlighting that, in the control scheme displayed in Fig. 4.7, the inductor current is sensed and used in the droop loop. Due to the buck converters topology, the inductor current and the output current are equal in steady-state, thus no additional sensing is required. The droop coefficient and the voltage set point used in this work are listed in Table 4.2. These parameters are chosen based on well-known droop control design methods in the literature, such as [88], [89]. Particularly, the voltage set point is designed at the nominal dc bus voltage V_{bus}. The droop coefficient is selected by considering the allowable voltage range Δv_o, and the nominal output current ($I_n = 15$), by considering: $k_d = \Delta v_o / I_n$. In this study, the droop loop also involves a first-order LPF with the cut-off frequency f_{lp} (see table Table 4.2) in order to eliminate the high frequency noise of the sampled signal [17].

Based on the structure shown in Fig. 4.7, at each converter, the small-signal representation, from the input a_x (or b_x) up to the output a_y (or b_y), can be derived as Fig. 4.8. According to Fig. 4.8a, the open current loop transfer function is:

$$G_C(s) = \frac{\hat{a}_y}{\hat{a}_x} = G_i(s) G_{del}(s) G_{id}(s) \tag{4.13}$$

where, the sign "ˆ" indicates the small-signal perturbations. The current regulator transfer function is shown by $G_i(s)$, and $G_{del}(s) = e^{-s\tau}$ approximates the delay

Parameter	Symbol	Value
	current loop	
Current regulator of all converters	G_i	$0.02 + 74.89/s$
	voltage loop	
Voltage regulator of buck #1, #2	$G_v^{\#1,\#2}(s)$	$0.21 + 544/s$
Voltage regulator of buck #3	$G_v^{\#3}(s)$	$0.1 + 272/s$
	droop loop	
Voltage set point	V_{sp}	200 V
Droop coefficient	k_d	1.33 V/A
LPF cut-off frequency	f_{lp}	25 Hz

TABLE 4.2: Regulators parameters of the converters in Fig. 4.6

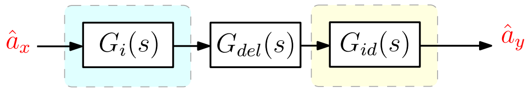

(a) Current loop $G_C(s)$.

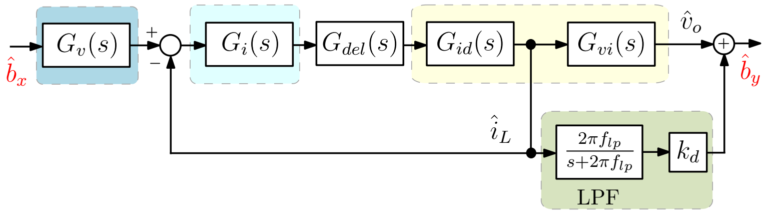

(b) Droop loop $G_D(s)$.

Fig. 4.8. Small-signal representation of the open loop gains under study.

due to digital control and PWM, where τ is in the scale of the switching period $T_{sw} = 1/f_{sw}$. $G_{id}(s)$ is the power-stage transfer function from the duty ratio to the inductor current [39]:

$$G_{id}(s) = \frac{\hat{i}_L}{\hat{d}} = \frac{V_{in}(sC_oZ_L(s)+1)}{s^2Z_L(s)L_oC_o + sL_o + Z_L(s)} \tag{4.14}$$

where C_o, L_o, and V_{in} are the buck capacitance, inductance, and input voltage, respectively. For a single converter, $Z_L(s)$ is equal to the resistive load seen from the converter terminal R_L. In case there is one (or more) additional converter(s) connected to the common dc bus, $Z_L(s)$ is the total impedance seen from the converter terminal, as explained in many studies, such as, [39, 97]. So, in the dc microgrid shown in Fig. 4.6: $Z_L(s) = R_L \parallel Z_o^{\#2}(s) \parallel Z_o^{\#3}(s)$, where $Z_o^{\#2}(s)$ and $Z_o^{\#3}(s)$ are the closed loop output impedances of the converter #2 and converter #3, respectively. More details on how to find the output impedance of a buck converter can be found in [39]. It is worth remarking that, in Fig. 4.7 the current loop—equation (4.13)— is chosen in such a way that the measurements are not affected by the voltage loop.

Similarly to the current loop, and based on the block diagram shown in Fig. 4.8b, the open droop loop transfer function can be written as follows:

$$G_D(s) = \frac{\hat{b}_y}{\hat{b}_x} = G_v(s)G_C^c(s)\left[G_{vi}(s) + k_dG_{lp}(s)\right] \tag{4.15}$$

where, $G_{lp}(s)$ represents the LPF transfer function and $G_{vi}(s)$ is the power-stage transfer function from the inductor current to the output voltage:

$$G_{vi}(s) = \frac{\hat{v}_o}{\hat{i}_L} = Z_L(s) \parallel \frac{1}{sC_o} \tag{4.16}$$

and $G_C^c(s)$ is the closed current loop transfer function:

$$G_C^c(s) = \frac{G_C(s)}{1 + G_C(s)} \tag{4.17}$$

A simulation model of the dc microgrid shown in Fig. 4.6 is developed in MATLAB/SIMULINK. The orthogonal PRBS generation algorithm shown in Fig. 4.3 is herein applied with $k_{gen} = 8$, $N = 7$. In this work, $M = 2$ (so $m = 1$, and $r_1 = 2$), because, herein, only the inductor current loop, and the droop loop are identified. Similarly, other orthogonal PRBS signals can also be generated and injected into the other loops that might exist in the DER converters. As shown in Fig. 4.7, the MLBS perturbation is injected at point (1) to excite the current loop and the IRS is injected at point (2) to excite the droop loop of one of the converters shown in Fig. 4.6 (e.g., converter #1). Then, the frequency response of the current loop $G_C(j\omega)$ is calculated by applying the superposition theorem with logarithmic averaging process [98]:

$$G_C(j\omega) = \left(\prod_{p=1}^{P} \frac{a_{y,p}(j\omega)}{a_{x,p}(j\omega)} \right)^{1/P} \tag{4.18}$$

where P is the total number of injected perturbation periods, and $a_{x,p}(j\omega)$ is the FFT of the measured input sequences at the excitation period p, where $p = 1, 2, \cdots, P$. Likewise, $a_{y,p}(j\omega)$ is the FFT of the measured output sequences at the excitation period p. The frequency response of the droop loop $G_D(j\omega)$, from the input b_x up to the output b_y can be computed, in a similar way.

Simulation results for simultaneous identification of $G_C(j\omega)$ and $G_D(j\omega)$ are reported in Fig. 4.9a and Fig. 4.9b, respectively, and are compared with the analytical models found in (4.13) and (4.15). As can be seen, within the measurable bandwidth, a precise identification of each loop gain is achieved. This simulation is performed without considering the noise effect, which will be more detailed in the next section. The frequency response of the droop loop is just plotted in the low frequency range, because its bandwidth is very low (compared to the one of the current loop), and the higher frequency behavior is not of specific interest for this study.

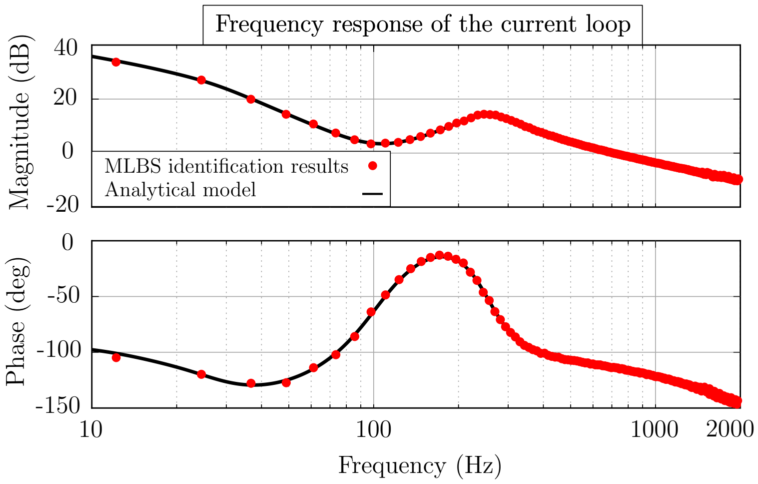

(a) $G_C(j\omega)$ identification based on injecting MLBS at point (1) of Fig. 4.7

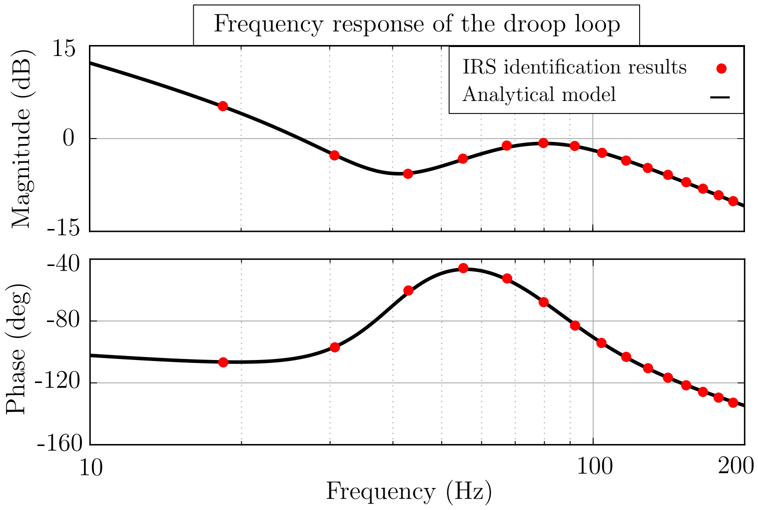

(b) $G_D(j\omega)$ identification based on injecting IRS at point (2) of Fig. 4.7

Fig. 4.9. Analytical model of the current loop, in (4.13), and the droop loop, in (4.15), compared with the simulation results of simultaneous multiple loop gain identification for converter #1.

4.4 Experimental validation

A laboratory prototype of the system shown in Fig. 4.6 is implemented to emulate an islanded dc microgrid. The same parameters as the simulation model, listed in Table 4.1, and Table 4.2 are used. The PRBS identification algorithm discussed in Section 4.2 is implemented in the digital control platform of the converters. In order to validate the correctness of the identification results, the experimental setup is tested by means of the Sweep Frequency Response Analysis (SFRA) tool [79]. Based on SFRA [40], the loop under study is perturbed frequency-by-frequency, then by evaluating the FFT of the inputs and outputs, the frequency response is calculated.

4.4.1 Simultaneous monitoring of two loop gains

When injecting the PRBSs, we must choose the perturbation amplitudes according to the two following conditions:

- Condition 1: Effects of the small-signal perturbations on the output currents and the bus voltage must be reasonably low in steady-state, so that they do not disturb the system operating point.
- Condition 2: Effects of the small-signal perturbations on the output currents and the bus voltage must be larger than the quantization errors and the noise levels.

The transfer function from the perturbation point to the bus voltage $G_{pv}(s)$, and the transfer function from the perturbation point to the inductor current $G_{pi}(s)$ can be analytically derived (or estimated to some extent). Then, for any system under study, K_{IRS} must be large enough to obtain:

$$|G_{pv}(f)| \cdot K_{IRS} \gg s_{nv}, \quad |G_{pi}(f)| \cdot K_{IRS} \gg s_{ni}, \tag{4.19}$$

where s_{nv} and s_{ni} are the noise levels on the bus voltage and the inductor current, respectively. By looking at different frequency ranges of the transfer functions above, the minimum value of the IRS perturbation amplitude can be determined. Similar discussion can be made for also the selection of K_{MLBS}.

In order to fulfill both Condition 1 and Condition 2, each PRBS amplitude must be adjustable based on the loop under study, and independently from the other loops. This can be achieved only if there exists a separate PRBS injection at each loop. In some cases, although, a single PRBS injection at the most external loop, with an appropriate amplitude is enough to excite two or more control loops, and measure their loop gains, as they might have similar SNR levels. However, this is not always the case.

To further address this issue, a small sinusoidal signal $s_p = K_p \cos(2\pi f_p t)$ is injected in the simulated model of the structure shown in Fig. 4.7. The aim is to understand if the inner (current) loop can be effectively excited through small-signal perturbation in the outer (droop) loop. The injection s_p is firstly inserted

f_p [Hz]	10	100	1000
When s_p, with amplitude $K_p = 0.08$ is inserted at point (1) of Fig. 4.7			
$\|a_x\|$	0.0005	0.05	0.175
When s_p, with amplitude $K_p = 3$ is inserted at point (2) of Fig. 4.7			
$\|a_x\|$	0.045	0.44	0.175

Table 4.3: Effect of small-signal perturbation in different loops on a_x

at point (1) of Fig. 4.7 (in converter #1), to directly perturb the current loop. This will lead to some perturbations with the same frequency (f_p), on a_x, and accordingly on the output signals. Then, s_p is inserted at point (2) of Fig. 4.7 to perturb the current loop through perturbations in the droop loop. In this case, as can be seen in Table 4.3, the perturbation amplitude K_p is significantly increased to reach the same value of a_x as the previous case, at high frequencies, which is important for the current loop. However, under this large K_p, the value of a_x at low frequencies becomes extremely larger than the case in which s_p was inserted at point (1). In particular, at 10 Hz, $|a_x| = 0.045$ which is 90 times higher than the value of a_x, when s_p was inserted at point (1). Of course, this is not desirable, because it will lead to a large ripple also on the output signals. So, in order for the Conditions 1 and 2 to be both met, an independent perturbation at each loop is required.

To verify this aspect also in the experiment, the following test is performed. Only the IRS signal is injected at point (2) of Fig. 4.7, in one of the three converters working in parallel (e.g., converter #1 in Fig. 4.6). This perturbation leads to small-signal variations on the inductor current and the output voltage. Then, the current loop and the droop loop are, respectively, identified by measuring a_x, a_y, and b_x, b_y, and averaging them over 32 excitation periods (P=32), to remove the noise effect. After calculating the FFT of the measured signals, the current loop gain is evaluated based on (4.18). Similarly the frequency response of the droop loop is also obtained.

The experimental identification results based on single IRS injection are reported in Fig. 4.10a and Fig. 4.10b. The identified loop gains are compared with the actual frequency responses of the loops found by SFRA. As can be noticed, the droop loop $G_D(j\omega)$ identification is achieved with a good accuracy. Because the IRS is actually injected at the droop loop, and its amplitude K_{IRS} is adjusted according to the SNR level of the droop loop (herein, $K_{IRS} = 0.2$). In other

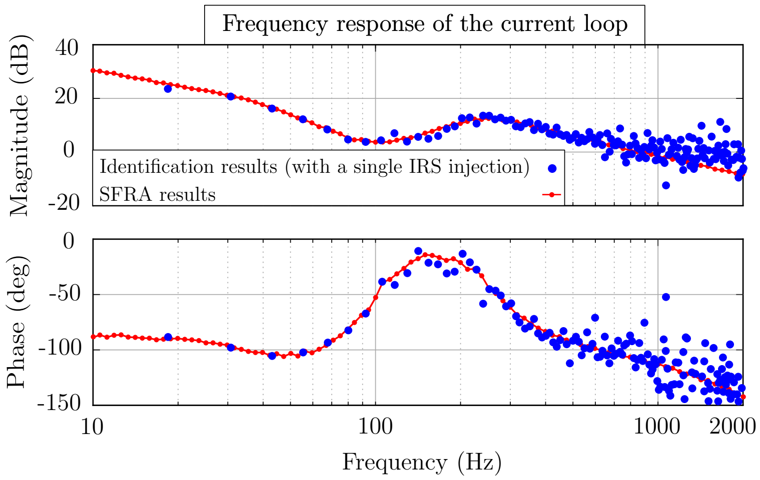

(a) $G_C(j\omega)$ identification

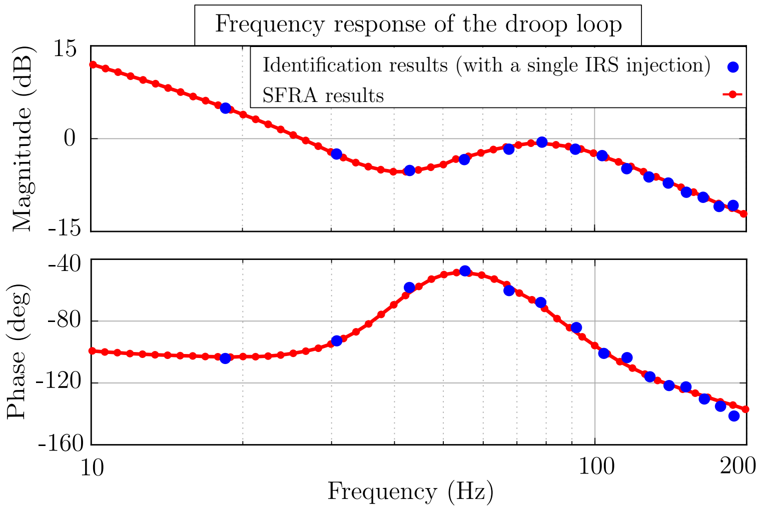

(b) $G_D(j\omega)$ identification

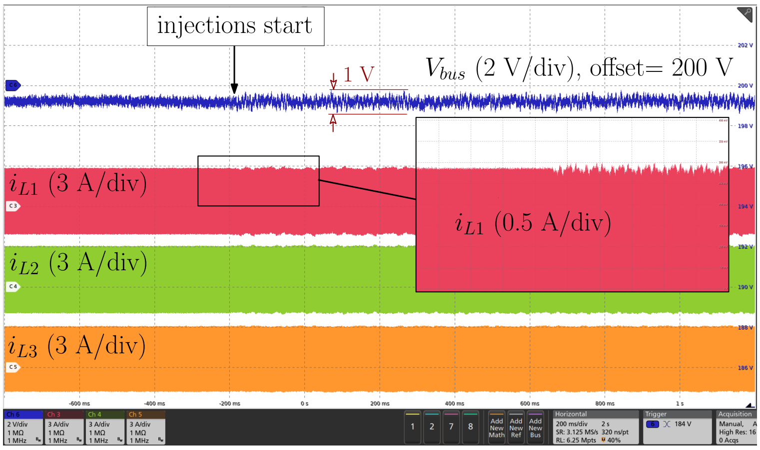

(c) Bus voltage, and inductor current ripples

Fig. 4.10. Experimental results when converter #1 is perturbed by only injecting IRS at point (2) of Fig. 4.7. The current loop identification is not accurate around the crossover frequency.

words, both Condition 1 and Condition 2 are satisfied for the droop loop. On the other hand, the current loop $G_C(j\omega)$ identification shows a large error, specially at high frequencies. This is because the effect of injecting IRS at point (2) of Fig. 4.7 on a_x and a_y is very low with respect to the noise level, as expected by Table 4.3. In other words, Condition 2 is not satisfied for the current loop. So, the information regarding the most interesting part of the current loop behavior, which is around its crossover frequency, is not provided. As discussed above, K_{IRS} cannot be extremely increased to solve this problem, otherwise Condition 1 will not be respected, and the system operating point might be disturbed. The ripples on the bus voltage and the inductor currents, introduced by the single IRS injection are shown in Fig. 4.10c. As can be seen, the bus voltage ripple does not exceed 1 percent of the nominal value. Also, the ripples on the inductor currents are very small with respect to the nominal values.

In order to perform simultaneous identification of the two control loops in an accurate way, both MLBS and IRS signals must be injected at the same time. The MLBS is injected at point (1) of Fig. 4.7, to identify the current loop of one of the three converters working in parallel (Fig. 4.6), and the IRS is injected at point (2), to identify the droop loop of the same converter. Herein, we assume that in a specific time-slot, only one of the converters is allowed to inject the small-signal perturbations (e.g., converter #1). MLBS and IRS injections lead to small-signal perturbations on the signals a_x, a_y, b_x, b_y. The effects of these two perturbations, however, are orthogonal and their combination does not cause inaccuracy in the identification. The signals a_x, a_y, b_x, b_y are measured and averaged over the same number of periods as the previous experiment (P=32), in order to remove the noise effect. Then, the FFT analysis is performed and the loop gains are found based on (4.18).

Fig. 4.11a and Fig. 4.11b report the experimental results of the MLBS-based current loop identification, and the IRS-based droop loop identification, respectively. The identification error of the current loop in Fig. 4.10a, is significantly improved over the bandwidth, as can be seen in Fig. 4.11a.The close matching between the actual frequency responses of the two loops found by SFRA, and those identified on-line, proves the performance of the adopted technique in rapid identification of multiple loop gains. The fact that each loop has a separate perturbation signal whose amplitude can be adjusted according to the SNR level of that loop, leads to more accurate results with respect to the previous experiment. It is also worth noticing that, the droop loop identification in Fig. 4.11b is performed with the same accuracy as Fig. 4.10b, because the presence of an uncorrelated perturbation signal does not affect the identification process. In this experiment, the perturbation amplitudes K_{MLBS} and K_{IRS} are set, respectively, to 0.08 and 0.2,

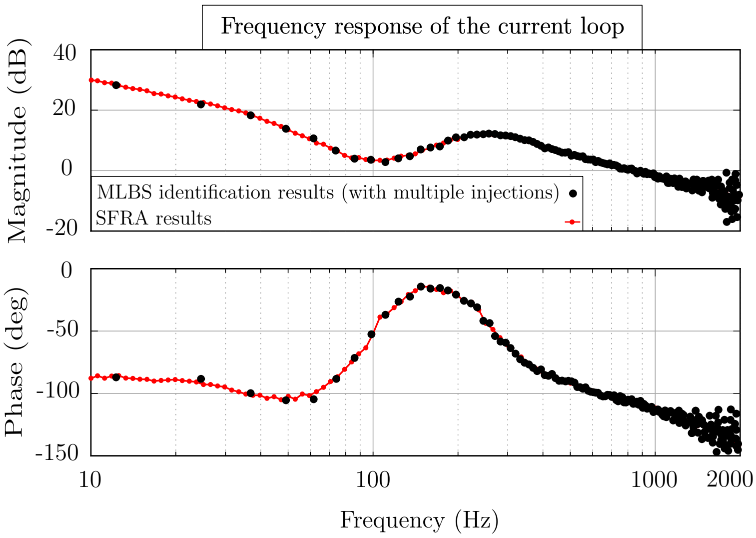

(a) $G_C(j\omega)$ identification

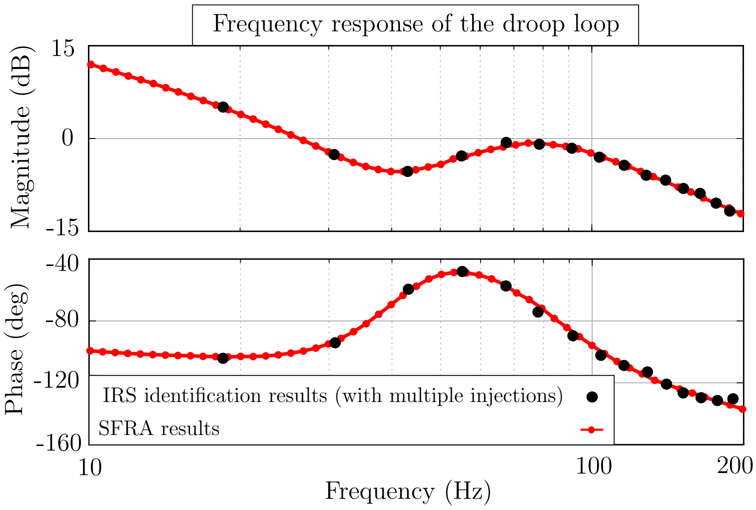

(b) $G_D(j\omega)$ identification

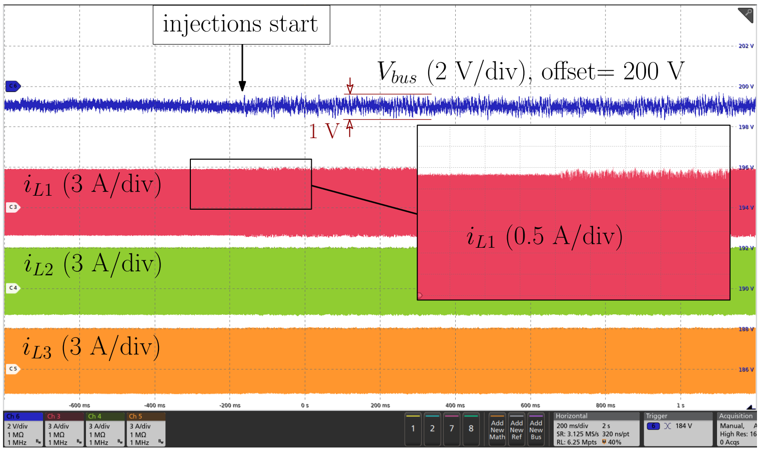

(c) Bus voltage and the inductor current ripples

Fig. 4.11. Experimental results when converter #1 is perturbed by two orthogonal PRBSs. The signals IRS, and MLBS are respectively injected at point (2), and point (1) of Fig. 4.7.

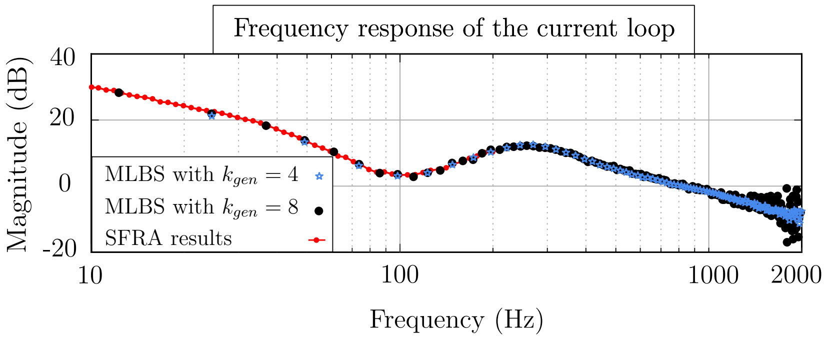

Fig. 4.12. Effect of increasing f_{gen} (decreasing k_{gen}) on the identification results.

which leads to almost the same perturbation on the output signals as the previous experiment, as shown in Fig. 4.11c.

Regarding Fig. 4.11, it is important to notice that, all the identifications are obtained in one measurement cycle. So, apart from being fast, the method also guarantees that the system operating conditions remain constant during the measurement. This is of paramount importance for accurate monitoring and further tuning actions, because, in some cases, the microgrid configuration can change rapidly [37].

The less accurate identification at high frequencies can be improved in several ways, such as cross-correlation, increasing the number of averagings, increasing the PRBS generation frequency f_{gen}, etc. [43,44]. As an example, the current loop identification in Fig. 4.11a is repeated with a higher f_{gen}, and the results (just magnitudes) are reported in Fig. 4.12. To this end, k_{gen} is decreased from 8 to 4, to change f_{gen}, based on see (4.8). This, as can be noticed in Fig. 4.12, leads to a better identification in higher frequency ranges, at the price of less frequency points.

4.4.2 An application of the identified models

After successfully identifying the frequency responses of different control loops, the digital compensator of each can be appropriately tuned to achieve desired dynamics, as done in many works such as [46,67,82,83]. For brevity, this work only reports the adaptive tuning of voltage regulator, which is performed to achieve the reference phase margin $\phi^*_{m,d}$ and the reference crossover frequency $f^*_{c,d}$ for the droop loop. Similar to the experiments discussed above, the three converters are working in parallel, but the PRBS-based identification and tuning is only performed in one of the converters (e.g., converter #1).

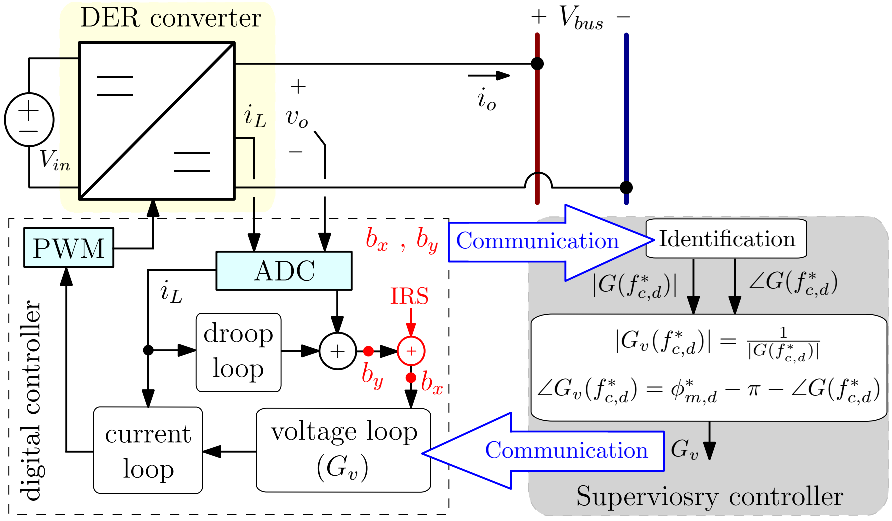

Fig. 4.13. Application of the proposed identification method in adaptive tuning. b_x, b_y are sent to the supervisory controller, where, *i*) the frequency response of G—that is the open loop gain without considering the compensator—at the reference crossover frequency $f^*_{c,d}$ is found: $G(f^*_{c,d})$ *ii*) the voltage regulator G_v is designed accordingly, to reach the reference phase margin $\phi^*_{m,d}$ and the reference crossover frequency for the droop loop $G_D = G \cdot G_v$. Finally, the updated G_v is sent back to the digital controller.

As displayed in Fig. 4.13, the digital controller sends b_x, b_y to the supervisory controller, through a communication interface. In this work, the supervisory control tasks are implemented by MATLAB which is running in parallel while the prototype is working. In MATLAB, b_x , b_y are averaged over the number of excitation periods P, then FFT analysis is done to identify the frequency response of the droop loop $G_D(j\omega)$. As the open loop gain without considering the compensator G_v can be found as $G = G_D/G_v$, the magnitude and phase of G, at the desired crossover frequency can be estimated: $|G(f^*_{c,d})|$, $\angle G(f^*_{c,d})$. At this point, the new G_v must be accordingly designed, so that G_D can have the crossover frequency and the phase margin, respectively, equal to $f^*_{c,d}$ and $\phi^*_{m,d}$. So:

- The magnitude of G_v, must be $|G_v(f^*_{c,d})| = \frac{1}{|G(f^*_{c,d})|}$, so that $G_D(f^*_{c,d}) = 1$.
- The phase of G_v, must be $\angle G_v(f^*_{c,d}) = \phi^*_{m,d} - \pi - \angle G(f^*_{c,d})$, so that $\angle G_D(f^*_{c,d}) = \phi^*_{m,d} - \pi$.

Similar adaptive tuning methods are used in [83,99–101]. Finally, the updated G_v is sent back to the digital controller, as shown in Fig. 4.13.

Assuming that the orthogonal PRBSs are injected periodically with the cycle T_p, as represented in Fig. 4.14. The perturbation time T_1 is the time required for all the excitation periods $T_1 = P * l_{IRS}/f_s$. Herein, a high number of averaging is

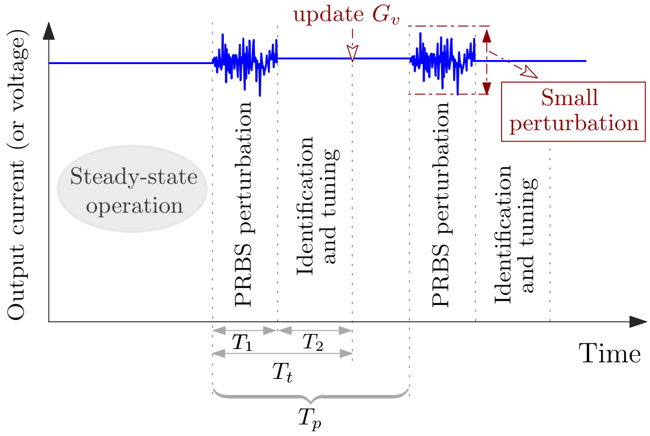

Fig. 4.14. Time schedule of the implemented adaptive tuning algorithm. The orthogonal PRBSs are injected periodically with the cycle T_p.

used (P=32) to remove the noise effect, so $T_1 \simeq 7\,\mathrm{s}$. But, in less noisy conditions T_1 can be much smaller. All the signal processing part, plus the time required for the communication (that depends on the Baud-Rate of the interface) is T_2, which in our case is less than 9 s. Therefore, in this experiment, the total perturbation, identification and tuning time T_t is less than 16 s. Hence, multiple orthogonal PRBSs are proposed to be injected periodically with cycle $T_P = 20\,\mathrm{s}$.

In this work, the proportional gain K_{pv} and the integral gain K_{iv} of the voltage regulator $G_v = K_{pv} + K_{iv}/s$, are updated to achieve the reference crossover frequency $f^*_{c,d} = 100\,\mathrm{Hz}$, and the reference phase margin $\phi^*_{m,d} = 85$ deg, for the droop loop $G_D(j\omega)$. Fig. 4.15 shows the G_v parameters (K_{iv}, K_{pv}), during the proposed tuning algorithm. As can be seen, after the first cycle of perturbation and identification, the G_v gains are increased to provide the larger bandwidth for the droop loop. The phase margin is also kept high to ensure a stable operation.

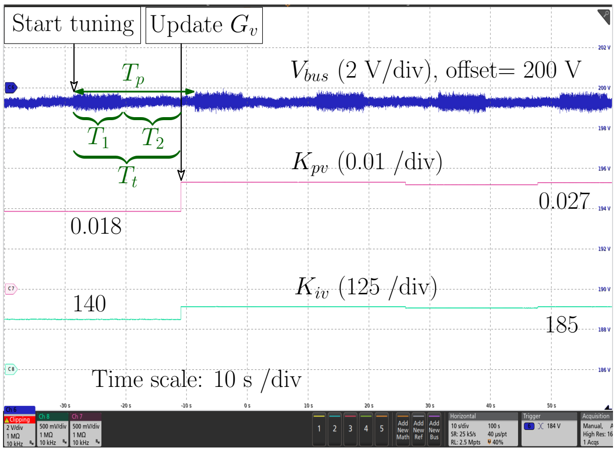

Fig. 4.15. Experimental results of tuning the G_v parameters (K_{iv}, K_{pv}), based on PRBS identification results.

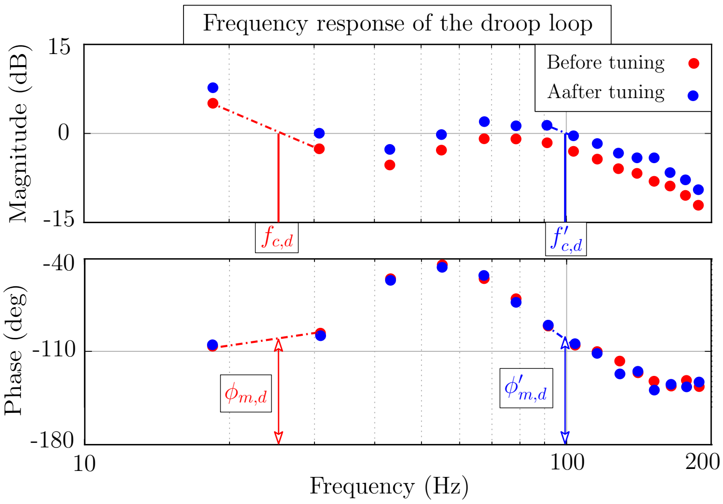

Fig. 4.16. PRBS-based experimental identification results of the droop loop, before and after tuning G_v. The desired crossover frequency and phase margin are successfully achieved.

For the next cycles, K_{iv} and K_{pv} stay almost constant, because the system is in steady-state. Although, in case of any change in the microgrid, the G_v gains will be again tuned to reach the above-mentioned stability margins. To show the effectiveness of the implemented tuning algorithm in reaching the the desired dynamics, the two experimentally-found frequency responses of the droop loop identification (before and after tuning G_v) are shown in Fig. 4.16. As can be seen, the estimated crossover frequency and phase margin of the droop loop after tuning ($f'_{c,d}$, $\phi'_{m,d}$), converge to the desired reference values ($f^*_{c,d}$, $\phi^*_{m,d}$).

4.5 Summary

This chapter proposes to use simultaneous injection of multiple orthogonal PRBSs into different control loops of SMPS converters, for on-line loop gain identification. Based on this approach, the frequency responses of the loops under study can be measured in a single experiment, thus, providing a rapid loop gain monitoring. A laboratory prototype of the dc microgrid composed of three droop-controlled converters is implemented, and discussed. The current loop and the droop loop of one of the converters are simultaneously identified by a) injecting a single PRBS in the most external loop, b) injecting two orthogonal PRBSs in the two loops under study, at the same time. In the second case, the identification results show a good matching with the actual transfer functions of the experimental setup, found by the SFRA tool. Therefore, the necessity of having multiple excitations to perform multiple loop gain identification is experimentally confirmed. Finally, a tuning algorithm is implemented to achieve desired dynamics for the droop loop, based on the identification results. To conclude, the good accuracy of the identified models, the short identification time, and the fact that this technique can be extended to all the control loops within DER converters, makes it practical for dc microgrid applications.

Chapter 5

Using the monitored loop gains for dc bus impedance estimation and damping

5.1 Introduction

Monitoring a generic control loop within dc microgrid converters can provide us with the stability and performance of that loop, by also takes account for the effect of other converters connected to the same dc bus. However, the loop gain information of some loops might not give a comprehensive and microgrid-level assessment of the stability. In this context, this chapter aims to provide a system-level stability criteria, that in this work, is obtained based on the information of some DER converter loop gains.

An example of dc microgrid is shown in Fig. 5.1, in which, each power converter usually has multiple control loops. As can be seen, a multi-converter system can be divided in a source-side subsystem and a load-side subsystem. Interaction stability

---

Most parts of this Chapter are carried out in the power electronics group at the University of South Carolina, SC, USA. The kind support of prof. Enrico Santi during this work is highly appreciated.

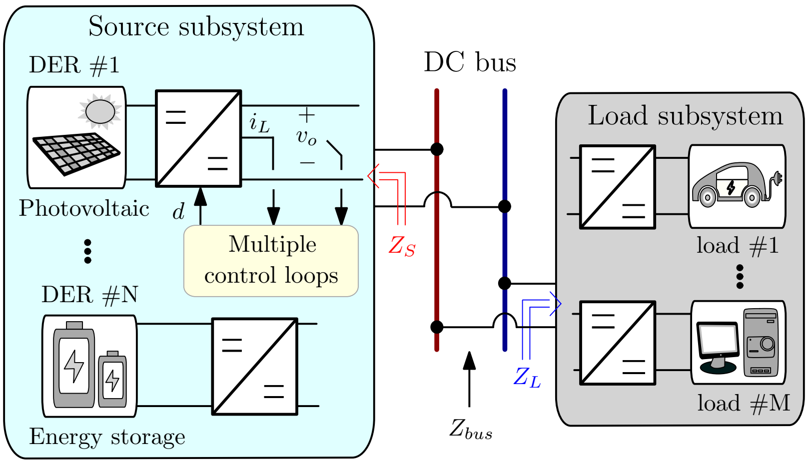

Fig. 5.1. An example of dc microgrid with several power electronic converters, each having multiple control loops. The whole system is divided into a source subsystem, and a load subsystem

of such a system has been typically investigated in many publications following the approach proposed by Middlebrook in [34]. To this end, the source subsystem equivalent impedance (shown as Z_S in Fig. 5.1) and the load subsystem equivalent impedance (shown as Z_L in Fig. 5.1) must be calculated. Fig. 5.2a shows the equivalent Thèvenin model of the dc microgrid composing of the source and the load subsystems, which are each modeled through their equivalent impedances. Then, the configuration shown Fig. 5.2 will be closed-loop stable if and only if the Nyquist plot of Z_S/Z_L for all the frequencies does not encircle the point $(-1, 0)$ (or it encircles $(-1, 0)$ as many times anticlockwise as Z_S/Z_L has right-half plane (RHP) poles) [34, 102].

The above-mentioned Middlebrook criterion limits the impedance ratio Z_S/Z_L—that is also called minor loop gain—into the unity circle on the complex plane. This is a restrictive condition that is not always easy to meet, and it can sometimes lead to the need for bulky input filters [103]. Some less restrictive forbidden regions

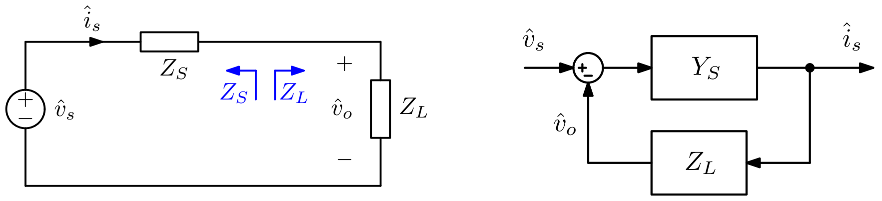

(a) Equivalent Thèvenin model of an interconnected system composing of the source and the load subsystems.

(b) The feedback system associated with Fig. 5.2a.

Fig. 5.2. Impedance-based representation of an interconnected power converter system.

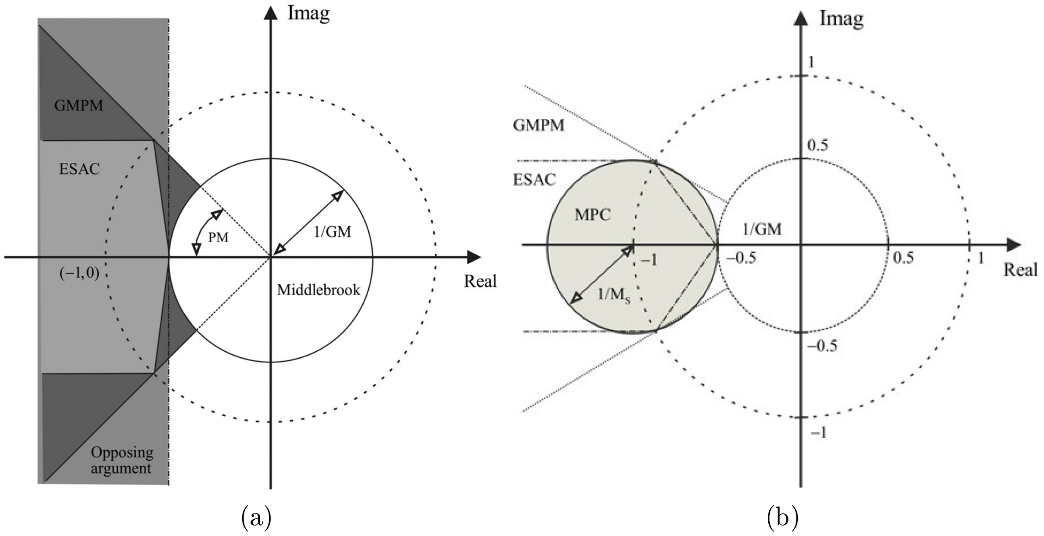

(a) (b)

Fig. 5.3. Some examples of different forbidden regions for the minor loop gain, that are less conservative than the Middlebrook criterion (unity circle) [104].

for the minor loop gain are proposed in the literature [60,104–107]. Fig. 5.3 shows some of these forbidden regions.

The impedance-based method is shown to be an effective tool for small-signal stability analysis, since it features the property of modularity by dividing the whole interconnected system into source and load subsystems. Besides, all the physical components and control parts of the power converter are intrinsically considered in the measured impedances. So, both source and load subsystems can be regarded as “black boxes”, thus, eliminating the need to prior knowledge about their internal structures and parameters.

Impedance-based stability analysis, however, has some limitations, such as sensitivity to the component grouping and power flow direction [61]. To tackle these issues, the passivity-based stability criterion (PBSC) has been proposed in the literature [62]. This criterion, together with the allowable impedance region (AIR) criterion [63], assesses the stability of an interconnected power converter system by only looking at the dc bus impedance. As shown in Fig. 5.1, the dc bus impedance (Z_{bus}) can be defined as the parallel combination of the source subsystem output impedance (Z_S) and the load subsystem input impedance (Z_L). PBSC and AIR allow us to not only assess the stability of an interconnected system, but also investigate its dynamic performance, and design some stabilization control, if needed [63].

So far, different bus impedance-based stabilization techniques have been proposed in the literature. One approach is to augment the controller of the load-side

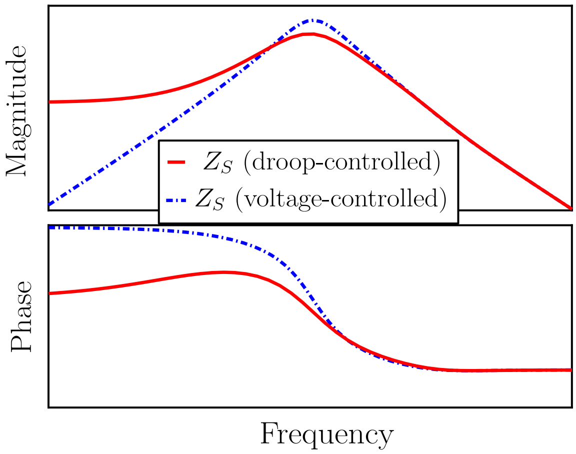

Fig. 5.4. Typical output impedance Z_S of droop-controlled and voltage-controlled DER converters.

converter, for instance, by adding a positive feed-forward controller [63, 64, 108], in order to eliminate the high peak of the bus impedance amplitude. A second approach is to damp the high-peak resonance of the bus impedance by acting on the source-side converter. This can be done by either updating the existing controller gains [46], or by adding a damping term in the control, as done for example, in [32].

The above-mentioned bus stabilization methods are all based on bus impedance measurement, which requires long data sequences, and Fourier Transform to be performed, requiring, thus, an auxiliary processor for implementation. However, it turns out that one can use data available inside the digital controller of the source converter to effectively estimate the peak value of bus impedance, thus eliminating the need for direct impedance measurement. Usually, in the output impedance Z_S of both voltage-controlled and droop-controlled DER converters, a peak appears in the mid frequency range [32, 109], as shown in Fig. 5.4. Assuming the commonly-used proportional-integral-derivative (PID) controllers, the peak of Z_S usually occurs around the bandwidth frequency of the voltage (or droop) control loop [32, 97, 109–114]. If this peak is high enough, it can interact with the load subsystem impedance Z_L, thus, creating a resonance in the bus impedance at the same frequency range.

By assuming that the bus impedance resonance is around the bandwidth frequency of the voltage (or droop) loop, this work proposes to use the phase margin of the voltage (or droop) loop, in order to estimate the peak value of the bus impedance. The online phase margin monitoring of a generic control loop within dc microgrid power converters is addressed in [73]. The concept is based on the extension of Middlebrook's analog injection technique [51] to the digitally controlled power converters. To this end, a small-signal perturbation is injected in a generic control loop during its normal operation, and the injection frequency is adjusted until it reaches the unity loop gain frequency (i.e., crossover frequency). At this frequency, the phase shift between the signals before and after perturbation yields the phase margin. This research shows that the obtained phase margin can be effectively used to estimate the peak value of bus impedance. This peak is subsequently damped by autotuning the controller gains of the voltage loop, so as to satisfy PBSC and AIR requirements.

In brief, the proposed monitoring and stabilization technique

- removes the need for impedance measurement, and thus, for an auxiliary processor.
- is simple and has low implementation complexity.
- is robust to noise and perturbations that might come from other converters connected to the common dc bus.

The remainder of this chapter is organized as follows. Section 5.2 briefly explains the PBSC and AIR based on dc bus impedance. Section 5.3 provides small-signal representation of the source converter loop gain, by including the load subsystem effect as a separate term. These equations are then used to re-write the bus impedance equation as a function of the source converter loop gain., and then to estimate the peak value of bus impedance based on the source converter phase margin. Section 5.4 extends the bus impedance estimation to a system with two (or more) source converters, which is of particular interest for dc microgrid applications. Section 5.5 presents the proposed online bus impedance monitoring and damping approach. Section 5.6 describes the considered case study and presents experimental validation of the technique.

5.2 Interaction stability based on bus impedance

Recently, the interaction stability of an interconnected power converter system, as shown in Fig. 5.1, has been studied based on dc bus impedance [62]. Bus impedance Z_{bus} is defined as the parallel combination of the source subsystem impedance Z_S, and the load subsystem impedance Z_L:

$$Z_{bus} = Z_S||Z_L = \frac{Z_S Z_L}{Z_S + Z_L} \tag{5.1}$$

In order for PBSC to be satisfied, *a*) Z_{bus} should not contain any right-half-plane (RHP) poles; *b*) For all frequencies, the real component of Z_{bus} must be positive ($Re\{Z_{bus}(j\omega)\} \geq 0 \forall \omega$). This is equivalent to have the phase of bus impedance confined withing the −90 deg, +90 deg sector [115].

The PBSC gives general insight on stability of the system under study; however, it does not give information regarding dynamic performance. For example, as shown in Fig. 5.4, in the mid frequency range the magnitude of Z_S exhibits a peak that can be comparable with the magnitude of Z_L (while the phases have around 180 deg difference). This, according to (5.1), results in a resonant peak in the bus impedance. Even though this resonance may not be large enough to violate the PBSC, it can cause an oscillatory behavior for the bus voltage, thus deteriorating the system dynamic performance.

To overcome this limitation, the AIR has been introduced [63]. In particular, a simplified representative function of the bus impedance, with one large resonance in the mid frequency range is considered [32].

$$Z_{bus} = Z_{bus,0} \frac{s\omega_o}{s^2 s\omega_o / Q_{bus} + \omega_o^2} \tag{5.2}$$

where $Z_{bus,0}$ is the characteristic value of bus impedance, ω_o is the resonance frequency, and Q_{bus} is the Q-factor. In order for AIR to be satisfied, the normalized bus impedance ($\frac{Z_{bus}}{Z_{bus,0}}$) must be confined within a semi-circle in the right half-plane, centered at (0,0), with a radius equal to the maximum allowable peak factor Q_{max} [32]. Fig. 5.5 shows this concept by plotting the allowable region for the normalized bus impedance.

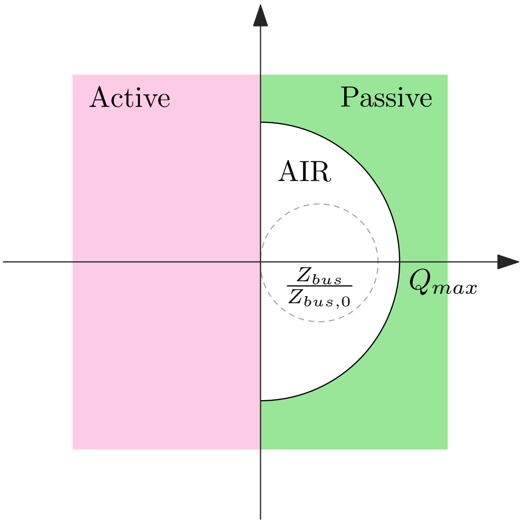

Fig. 5.5. PBSC together with AIR requiring the Nyquist contour of the normalized bus impedance to be confined within an allowable region.

As explained above, the high-peak resonance in the bus impedance shows the dynamic performance and stability condition of the interconnected power converter system. In order to damp the mentioned high peak of the bus impedance, it is necessary to either decrease the peak value of the source output impedance [32], or increase the magnitude of the load input impedance [63, 64] around ω_o. This will guarantee an improved performance on the bus. In both cases, however, the bus impedance measurement and re-design needs the frequency response measurement of both source and load impedance. This, of course, needs long data sequences, and Fourier Transform to be performed, requiring, thus, an auxiliary processor for implementation. To tackle these issues, in this Chapter we aim to estimate the bus impedance based on some loop gains measured locally, inside the digital control platform of a generic DER converter. However, this estimation, and the resulting stability analysis is based one some assumptions as detailed in Section 5.3. Therefore, although it simplifies all the process, but it is not a comprehensive and rigorous analysis tool. To do such a complete and general analysis, one should refer to the bus impedance measurement discussed above [32].

5.3 Representation of bus impedance in terms of loop gain

In this section, firstly, an expression for the source converter loop gain is derived, in which, the effect of all the other source and load converters connected to the bus, is taken into account. Then, (5.1) is re-written to provide a representation of bus impedance based on voltage (or droop) loop gain.

5.3.1 Loop gain of the source converter

The typical multi-loop control structure of a generic DER converter is shown in Fig. 5.6. In particular, inductor current i_L and output voltage v_o control loops are considered. When the switch Sw is open, a constant reference voltage is considered ($v_{ref} = V_{sp}$). However, for power sharing among parallel DERs [18], the switch Sw can be closed, enabling thus the droop loop ($v_{ref} = V_{sp} - k_d \cdot i_o$); where k_d is the droop coefficient and i_o is the output current. The inductor current and output voltage regulators $G_i(s)$, $G_v(s)$ are usually designed for the nominal load, and are based on well-known control design approaches in the literature [39]. However, in a dc microgrid environment, where several source and load converters are connected to the dc bus, the dynamic behavior of some loops can vary from the designed performance. To clarify this aspect, herein, we indicate as Z_T the overall

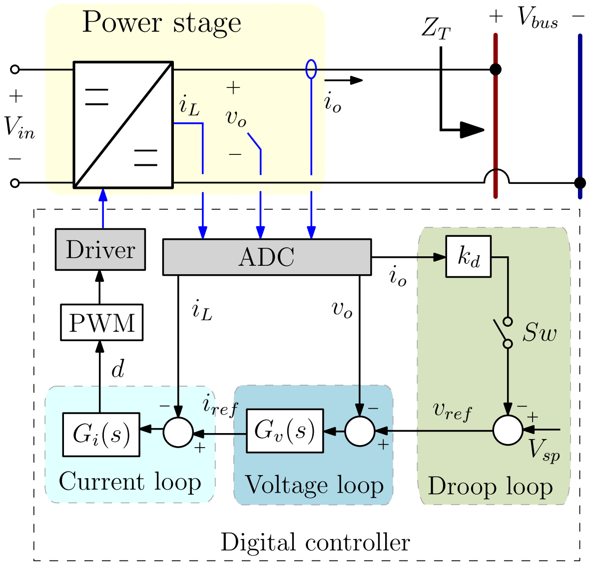

Fig. 5.6. A generic droop-controlled or voltage-controlled DER converter.

impedance seen from a converter terminal looking into the dc bus, as shown in Fig. 5.6.

A block diagram of the converter in Fig. 5.6 is shown in Fig. 5.7, where the rest of the microgrid is represented by the equivalent impedance Z_T. For simplicity, herein, we refer to the voltage-controlled case. The power-stage transfer functions $G_{id}(s)$, $G_{ii}(s)$, $G_{vi}(s)$, and $G_{i_ov}(s)$, respectively stand for the transfer function from duty ratio to inductor current, from output current to inductor current, from inductor current to output voltage, and from output current to output voltage. Their specific expressions for different converter topologies are well documented in the literature, for example in [39].

Fig. 5.7 can be further simplified in the form of Fig. 5.8a, and then Fig. 5.8b. According to Fig. 5.8a, the transfer function from output current to output voltage, with only current loop closed (i.e., output impedance of the current-controlled

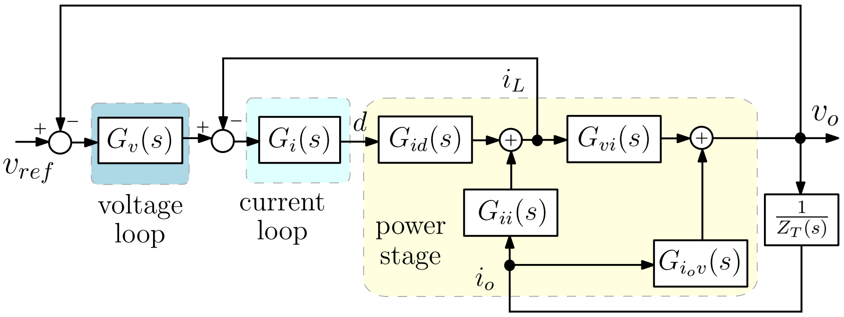

Fig. 5.7. Small-signal representation of the voltage-controlled DER converter (Fig. 5.6, when the switch Sw is open).

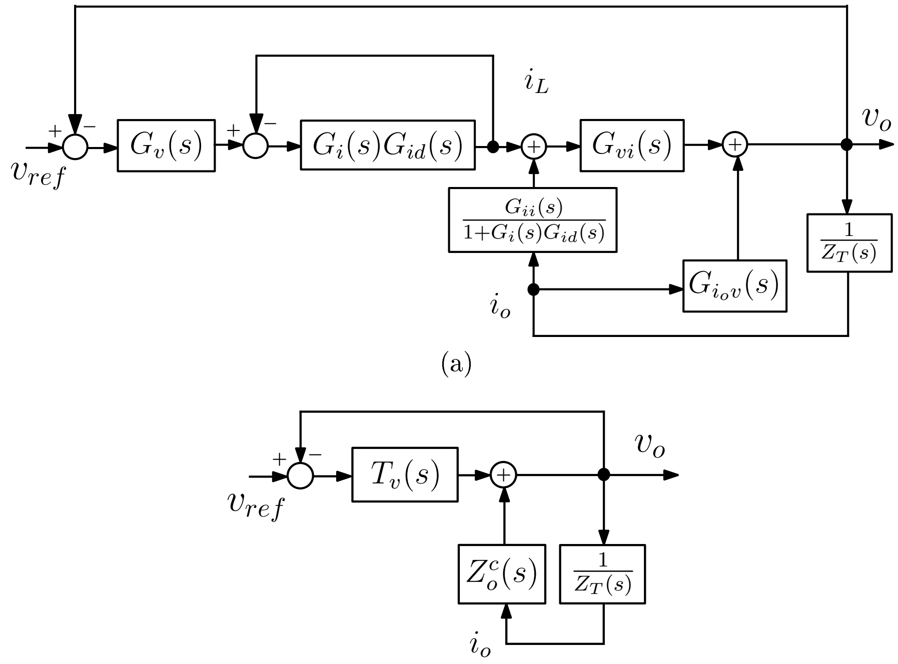

(a)

(b)

Fig. 5.8. Simplified versions of the small-signal model in Fig. 5.7.

converter), can be expressed as follows.

$$Z_o^c(s) = G_{i_ov}(s) + \frac{G_{ii}(s)G_{vi}(s)}{1 + G_i(s)G_{id}(s)} \tag{5.3}$$

The open voltage loop transfer function, with no load, is:

$$T_v(s) = G_v(s)G_{vi}(s)\frac{G_i(s)G_{id}(s)}{1 + G_i(s)G_{id}(s)} \tag{5.4}$$

Expressions (5.3) and (5.4) are independent of other load and source converters connected to the dc bus.

According to Fig. 5.8b, the closed loop output impedance of the source converter is:

$$Z_S(s) = \frac{Z_o^c(s)}{1 + T_v(s)} \tag{5.5}$$

By considering the effect of the rest of the system on a generic source converter through equivalent impedance Z_T, the new voltage loop gain can be written as follows.

$$T_{v,l}(s) = T_v(s).\frac{1}{1 + \frac{Z_o^c(s)}{Z_T(s)}} \tag{5.6}$$

Combining (5.5) and (5.6), one can re-write the voltage loop gain:

$$T_{v,l}(s) = T_v(s).\frac{1}{1+\frac{Z_S(s)}{Z_T(s)}(1+T_v(s))} \tag{5.7}$$

Let us assume that (5.7) represents the loop gain of a generic DER converter, connected to a certain number of source and load converters. Now, if a new source converter is connected to the dc bus, the only change in (5.7) will be in Z_T, where the previous value must be combined in parallel with the output impedance of the new source converter.

As mentioned above, the bus impedance resonance, usually, appears in the mid frequency range, where the magnitude of the source output impedance Z_S is comparable with the magnitude of the load input impedance Z_L (with 180 deg phase shift due to the negative incremental impedance of the feedback controlled load converter). This conclusion can also be reached using (5.7). To show this, we must notice that, if the load-subsystem is all that we see from the terminal of a source converter, then Z_T is equal to the input impedance of the load Z_L. Thus, in (5.7), if $Z_S(j\omega) \to -Z_T(j\omega)$, for some $\omega = \omega_o$, then $T_{v,l}(j\omega_o) \to -1$, meaning that the loop gain crosses 0 dB at ω_o, with approximately zero phase margin, therefore at the edge of instability. This example shows the equivalence between loop gain and bus impedance in detecting the interaction stability issues. However, a detailed analytical equivalence between the two approaches is presented in the next subsection.

5.3.2 Bus impedance estimation

Representation of bus impedance in terms of the voltage loop gain, can be simply found by combining (5.1) and (5.7):

$$Z_{bus}(s) = \frac{Z_T(s)\big(T_v(s) - T_{v,l}(s)\big)}{T_v(s)\big(1+T_{v,l}(s)\big)} \tag{5.8}$$

In order to obtain a simpler relationship between $Z_{bus}(s)$ and $T_{v,l}(s)$, let us focus on the mid frequency range, i.e., around the resonant frequency ω_o. By writing (5.8) in the polar form, we get:

$$k_b e^{j\theta_b} = \frac{k_T e^{j\theta_T}\big(|T_v(j\omega_o)|e^{j\angle T_v(j\omega_o)} - |T_{v,l}(j\omega_o)|e^{j\angle T_{v,l}(j\omega_o)}\big)}{|T_v(j\omega_o)|e^{j\angle T_v(j\omega_o)}\big(1+|T_{v,l}(j\omega_o)|e^{j\angle T_{v,l}(j\omega_o)}\big)} \tag{5.9}$$

where, $k_b = |Z_{bus}(j\omega_o)|, \theta_b = \angle Z_{bus}(j\omega_o)$, $k_T = |Z_T(j\omega_o)|, \theta_T = \angle Z_T(j\omega_o)$. Further simplification is possible if we consider that the 0 dB crossing of the loop gain typically occurs around ω_o:

Assumptions

It is assumed that the bus impedance resonance appears at a frequency close to the crossover frequency of the voltage loop, for both cases of with and without load effect:

$$|T_v(j\omega_o)| \simeq 1 \tag{5.10a}$$

$$|T_{v,l}(j\omega_o)| \simeq 1 \tag{5.10b}$$

The validity of these assumptions is discussed in the next subsection.

Using the assumptions (5.10a) and (5.10b), the absolute value of (5.9) can be written as follows:

$$k_b \simeq \frac{k_T|e^{j\angle T_v(j\omega_o)} - e^{j\angle T_{v,l}(j\omega_o)}|}{|1 + e^{j\angle T_{v,l}(j\omega_o)}|} \tag{5.11}$$

which can be simplified as:

$$k_b \simeq \frac{k_T\sqrt{1 - \cos\big(\angle T_v(j\omega_o) - \angle T_{v,l}(j\omega_o)\big)}}{\sqrt{1 + \cos\big(\angle T_{v,l}(j\omega_o)\big)}} \tag{5.12}$$

According to (5.12), the peak value of bus impedance can be obtained, internally, inside a source converter, by only measuring the phase margin of the voltage loop, and the magnitude of the impedance seen from the terminal of the source converter. Needless to mention, $\angle T_v(j\omega_o)$ is already known, because the initially designed phase margin of the voltage loop is known ($\phi_m = 180 \text{ deg} + \angle T_v(j\omega_o)$). Based on Taylor series of the square root function, one can obtain some approximations for (5.12). For example, herein, we limit the initially designed phase margin of the voltage loop ϕ_m, to a reasonable range, e.g., from 40 deg to 65 deg. Then:

$$k_b \simeq \frac{0.5k_T}{|\sin\big(\angle T_{v,l}(j\omega_o)\big)|} \tag{5.13}$$

5.3.3 Validation of the bus impedance estimation

A question that needs to be addressed is the accuracy of the estimated bus impedance formula (5.13), and of the assumptions (5.10) used to derive it. This is done through a literature search (for the assumptions), and a simulation-based investigation (for the assumptions and the estimation formula).

A literature review of papers addressing multi-converter dc bus stability shows that the peak value of source converter impedance Z_S occurs close to the voltage loop bandwidth. If the peak of Z_S is comparable with the magnitude of Z_L, then, according to (5.1), it results in a resonant peak in the bus impedance around the voltage loop bandwidth. Results of the literature search are summarized in Table 5.1. For brevity only a relatively small number of papers is included [32, 97, 109–114], all reporting cases where the peak value of Z_S in either voltage-mode or droop-mode operation, occurs around the voltage loop bandwidth.

In a simulation model, the accuracy of the estimation in (5.13), and the assumptions in (5.10) is evaluated by considering a system with a single buck converter as the source and a CPL as the load. The output inductance, output capacitance, nominal power, and nominal voltage of the source converter are, respectively, 1.5 mH, 110 µF, 3 kW, and 200 V. The source converter has a current loop designed at 1200 Hz bandwidth, and a voltage loop, supposed to have different bandwidths f_c from 100 Hz to 300 Hz. The voltage loop is designed with a good phase margin (e.g.,$\phi_m = 60$ deg), for the nominal resistive load. However, when it is connected to a 2.85 kW CPL (thus, $k_T = 14\,\Omega$), the phase margin $\phi_{m,l} = 180$ deg $+\angle T_{v,l}(j\omega_o)$ decreases, as shown in Fig. 5.9a. For different values of $\phi_{m,l}$, the peak value of bus impedance $\tilde{k}_b$ is estimated using (5.13). Table 5.2 summarizes the $\tilde{k}_b$ estimates, compared with the values read from Fig. 5.9b, i.e., $k_b = |Z_{bus}(j\omega_o)|$.

Reference	system under study	discussion
[32]	multi-converter dc power distribution system	a resonance terms is added to the conventional PI voltage regulator to damp the peak value of source output impedance, which is close to the voltage loop bandwidth
[109]	multi-converter dc power distribution system	nonlinear droop control is proposed to flatten the source output impedance, which has a peak around the voltage loop bandwidth
[111, 112]	dc power distribution system with single source and multiple load converters	different specifications are discussed to avoid the interaction between load subsystem impedance and source output impedance, which has a peak around the voltage loop bandwidth
[110, 113]	cascaded dc system composed of a source and a load converter	impedance interaction between the two converters is avoided by reducing the peak value of the source impedance, that appears around the voltage loop bandwidth
[97, 114]	dc microgrid with multiple source and load converters	frequency-dependent droop coefficients are proposed to shape the source output impedance and remove the mid frequency peak that occurs near the voltage loop bandwidth

TABLE 5.1: Some examples for the assumption that peak value of Z_S occurs close to the voltage loop bandwidth.

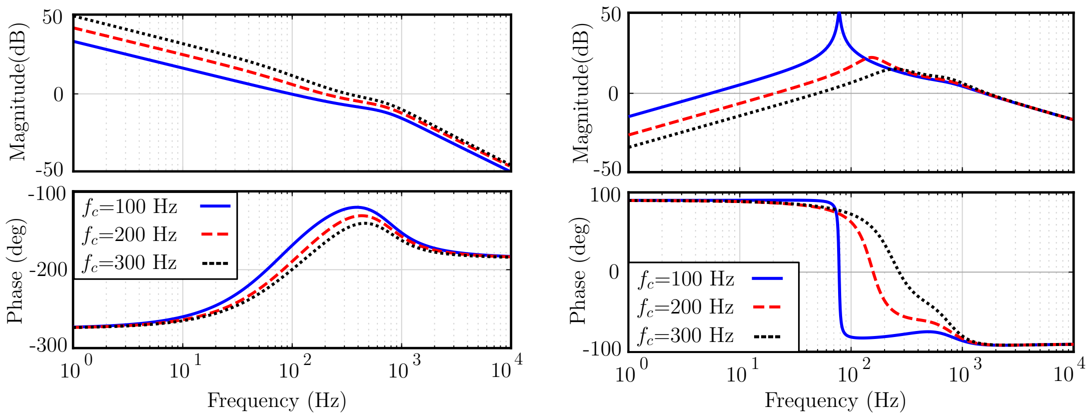

(a) Voltage loop gain of the source converter

(b) Bus impedance

Fig. 5.9. Loop gain $T_{v,l}$ and bus impedance Z_{bus}. The phase margins read from Fig. 5.9a, and the peak values of bus impedance read from Fig. 5.9b, are listed in Table 5.2.

As can be seen, the estimations are accurate, and can be relied on, for online monitoring and tuning actions. Another point, worth noticing regarding Fig. 5.9 and Table 5.2 is that, for higher peaks of the bus impedance, the phase margin is lower. This confirms the equivalence between bus impedance and loop gain for the stability assessment of an interconnected power converter system. Table 5.2 also reports the resonance frequency ω_o, and the load-affected voltage loop bandwidth $f_{c,l}$. As can be noticed, in all the cases, ω_o is close to the voltage loop bandwidth (i.e., $2\pi f_c \simeq \omega_o$), with a good approximation, verifying thus, the assumption in (5.10a). Besides, since in all the cases $2\pi f_{c,l} \simeq \omega_o$, the second assumption (5.10b) is also reasonable. However, for a different system with several source converters the second assumption might be less valid. To make sure that this will not significantly affect the estimation, herein, we consider $0.8 \leq |T_{v,l}(j\omega_o)| \leq 1.2$, and calculate (5.9) with such an approximation. It turns out that the final result of k_b has at most 10 % error with respect to the case when we consider $|T_{v,l}(j\omega_o)| \simeq 1$. Hence, the assumption in (5.10b) will lead to a good approximation in different cases, as well.

f_c	$f_{c,l}$	$\frac{\omega_o}{2\pi}$	$\phi_{m,l}$ (Fig. 5.9a)	$\tilde{k}_b$	$k_b = \lvert Z_{bus}(j\omega_o)\rvert$ (Fig. 5.9b)
100 Hz	92 Hz	78 Hz	1.5 deg	49 dB	49.8 dB
200 Hz	194 Hz	165 Hz	29 deg	23 dB	22.4 dB
300 Hz	290 Hz	240 Hz	45 deg	19.9 dB	19 dB

TABLE 5.2: Bus impedance estimation based on (5.13)

It is worth remarking that the above estimation method for the peak value of bus impedance may not hold for rare cases, where the bus impedance resonance does not appear around the voltage loop bandwidth frequency. This can be the case for non-PID controlled converters, or when the bandwidth of the voltage loop is not much lower than the bandwidth of the current loop.

5.4 Extension to the case of multi-source system

As mentioned in Section 5.3, the expression in (5.7) is also valid for the situation in which, several DER converters are connected in parallel. In this case, the term Z_T in (5.7) is the load input impedance in parallel with the output impedances of the other source converters. This is another way to explain the definition of Z_T, which was described as the equivalent impedance seen from a source's terminal looking into the dc bus. For a simple case, where there are two DER converters in parallel, the voltage loop gain of source converter #1 can be found by rewriting (5.7) as follows:

$$T_{v,l}^{\#1}(s) = T_v^{\#1}(s).\frac{1}{1+\frac{Z_S(s)}{Z_T(s)}(1+T_v^{\#1}(s))} = T_v^{\#1}(s).\frac{1}{1+\frac{Z_S(s)}{Z_L(s)||Z_s^{\#2}(s)}(1+T_v^{\#1}(s))} \tag{5.14}$$

where $Z_s^{\#2}$ stands for the output impedance of source converter #2, and $T_v^{\#1}$ is the open voltage loop transfer function of source converter #1 in no load condition. Likewise, the loop gain of source converter #2 ($T_{v,l}^{\#2}$), by taking account for the output impedance of source converter #1 can also be found. Then, by following a similar procedure as the case of single source converter, the bus impedance estimation can be presented as:

$$k_b \simeq \frac{0.5k_T}{|\sin\left(\angle T_{v,l}^{\#1}(j\omega_o)\right)|} = \frac{0.5(k_l||k_s^{\#2})}{|\sin\left(\angle T_{v,l}^{\#1}(j\omega_o)\right)|} \tag{5.15}$$

where k_l is the magnitude of load input impedance, and $k_s^{\#2}$ is the magnitude of $Z_s^{\#2}$.

To validate the estimation in (5.15), a similar model as Section 5.3.3 is considered. A similar buck converter is added to the source subsystem. In this case, to achieve current sharing, the droop loop is also considered by closing the switch Sw in Fig. 5.6 (the droop coefficient $kd = 2.6$ V/A). The current regulators of the two converters are the same. The voltage loop bandwidth of source converter #2 is fixed at $f_c^{\#2} = 200\,\text{Hz}$, while the one of source converter #1 is supposed to have different bandwidths $f_c^{\#1}$ from 100 Hz to 300 Hz. For these values the phase margin

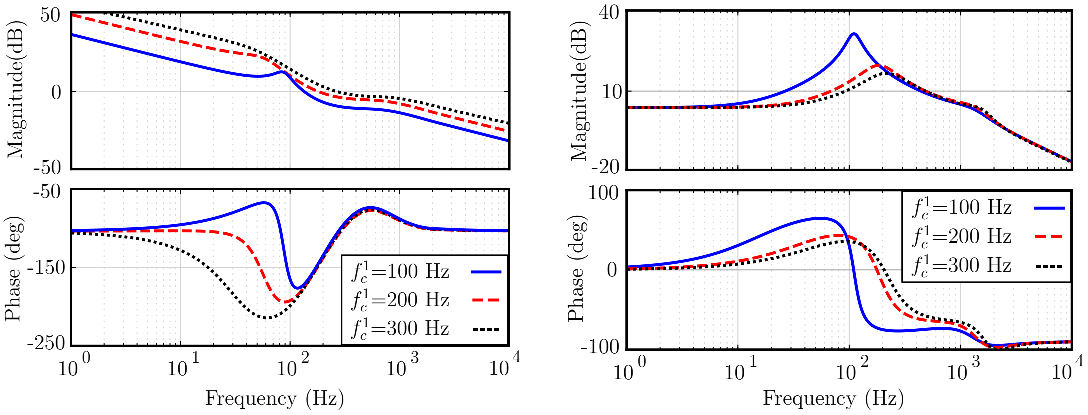

(a) Voltage loop gain of source converter #1

(b) Bus impedance

Fig. 5.10. Loop gain $T_{v,l}^{\#1}$ (when the droop loop is also closed), and bus impedance Z_{bus}. The phase margins read from Fig. 5.10a, and the peak values of bus impedance read from Fig. 5.10b, are listed in Table 5.3.

of source converter #1 $\phi_{m,l}^{\#1}$ changes, as shown in Fig. 5.10a. Also, the peak value of bus impedance $\tilde{k}_b$ will have different estimated values based on (5.15). Table 5.3 summarizes the $\tilde{k}_b$ estimates, compared with the values read from Fig. 5.10b, i.e., $k_b = |Z_{bus}(j\omega_o)|$. As can be seen, the estimations are accurate, and can be relied on, for online monitoring and tuning actions. It also can be noticed that the bus impedance resonance appears close to the crossover frequency of the source converter with lower voltage loop bandwidth. These results also show that overall stability of the system with two source converters is improved compared to the case of a single source. This, can be noticed in peak bus impedance, and phase margin which have respectively, lower and higher values with respect to the case of single-source (Table 5.3). The same accuracy in the bus impedance estimation can be achieved based on the phase margin of converter #2 ($\phi_{m,l}^{\#2}$), which is herein skipped for brevity.

It is worth mentioning that, the similar process can be followed for an arbitrary number N of parallel source converters. Based on the phase margin of the voltage

$f_c^{\#1}$	$f_c^{\#2}$	$\frac{\omega_o}{2\pi}$	$\phi_{m,l}^{\#1}$ (Fig. 5.10a)	$\tilde{k}_b$	$k_b =$ $\lvert Z_{bus}(j\omega_o)\rvert$ (Fig. 5.10b)
100 Hz	200 Hz	110 Hz	12 deg	29 dB	31 dB
200 Hz	200 Hz	190 Hz	38 deg	19.7 dB	19.5 dB
300 Hz	200 Hz	220 Hz	50 deg	17.8 dB	17 dB

TABLE 5.3: Bus impedance estimation based on (5.15)

(or droop) loop of each of the parallel DER converters, a good approximation of the peak bus impedance can be achieved. Thus, the stability situation (or the damping level of the dc bus) can be somehow estimated from the voltage (or droop) loop gain of each DER converter that works in parallel with many other converters.

$$k_b \simeq \frac{0.5k_T}{|\sin\left(\angle T_{v,l}^{\#1}(j\omega_o)\right)|} = \frac{0.5(k_l||k_s^{\#2}||\ldots||k_s^{\#N})}{|\sin\left(\angle T_{v,l}^{\#1}(j\omega_o)\right)|} \tag{5.16}$$

where $k_s^{\#N}$ is the magnitude of the output impedance of source converter #N (Z_s^N).

5.5 Proposed online monitoring and tuning technique

As concluded in the previous section, phase margin of the voltage loop $\phi_{m,l}$ can be effectively used to estimate the peak value of the bus impedance $\tilde{k}_b$. In order to find the phase margin of a generic control loop, without measuring the entire frequency response of that loop, some approaches have been proposed in the literature [52, 72]. These approaches are based on extending the Middlebrook's analog injection technique [51] to the digitally-controlled power converters. The main idea is to inject a small-signal perturbation into a control loop during its normal operation, and to regulate the injection frequency until the unity loop gain frequency (i.e., the crossover frequency) is reached.

$$|T_{v,l}(j\,2\pi\tilde{f}_{c,l})| = |v_y(j\,2\pi\tilde{f}_{c,l})|/|v_x(j\,2\pi\tilde{f}_{c,l})| \rightarrow 1 \tag{5.17}$$

At this frequency, the phase shift between the signals before and after perturbation (v_y and v_x) provides the phase margin.

$$\tilde{\phi}_{m,l} = 180 + \angle T_{v,l}(j\,2\pi\tilde{f}_{c,l}) = \angle v_y(j\,2\pi\tilde{f}_{c,l}) - \angle v_x(j\,2\pi\tilde{f}_{c,l}) \tag{5.18}$$

As can be seen, the first step is to calculate the magnitude of the loop gain $|v_y|/|v_x|$, at the injection frequency. The error compared to 1 (unity loop gain) is processed by an additional regulator, whose output is the injection frequency. According to [72], $|v_y|$ and $|v_x|$ can be found by multiplying each signal by the sine and cosine terms of the injection frequency, and then low-pass filtering the results. Thanks to the orthogonality of sinusoidal signals with different frequencies, the magnitude extraction is not affected by noise or other perturbation frequencies on the dc bus. Thus, the estimates of $\tilde{f}_{c,l}, \tilde{\phi}_{m,l}$ can still be accurate when different converters are connected to the common dc bus, and a perturbation with different frequency is injected into each of them.

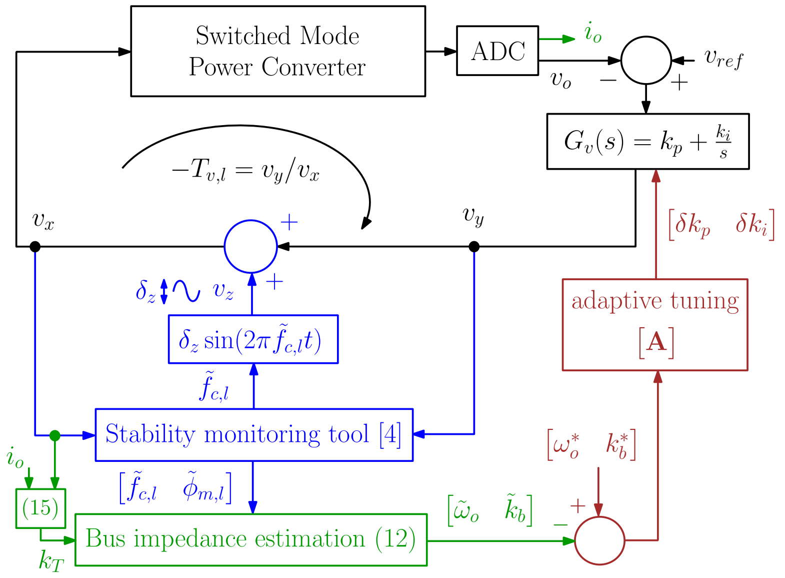

Fig. 5.11. Proposed online monitoring and tuning scheme. The peak bus impedance $\tilde{k}_b$ is estimated online, based on the phase margin of the voltage loop. The compensator gains of the voltage regulator (k_p, k_i) are, then, tuned by the matrix **A** to keep the bus impedance in an allowable region.

Herein, we propose to use the monitored phase margin to estimate the bus impedance, based on approximation (5.13). Using (5.13) requires the continuous measurement of k_T. Notice that k_T can be obtained using measurements available within the digital controller, where we already sample the outgoing current and the bus voltage at the injection frequency:

$$k_T = |Z_T(j\,2\pi \tilde{f}_{c,l})| \simeq \frac{|v_o(j\,2\pi \tilde{f}_{c,l})|}{|i_o(j\,2\pi \tilde{f}_{c,l})|} \tag{5.19}$$

Fig. 5.11 shows a diagram of the proposed monitoring and tuning technique, which uses loop injection without interrupting the feedback path. More specifically, it consists of three steps:

i. Apply the monitoring tool detailed in [72] to estimate the crossover frequency $\tilde{f}_{c,l}$ and the phase margin $\tilde{\phi}_{m,l}$ of the voltage loop.

ii. Estimate the peak value of bus impedance. In particular, $\tilde{\omega}_o \simeq 2\pi \tilde{f}_{c,l}$, and $\tilde{k}_b$ can be found based on (5.13), noticing that: $\angle T_{v,l}(j\omega_o) \simeq -180$ deg $+\tilde{\phi}_{m,l}$.

iii. Autotune the compensator gains of the voltage regulator (k_p, k_i), in order to keep the bus impedance in an allowable impedance region.

Regarding Fig. 5.11, it is worth remarking that, the small-signal perturbation on the output voltage: $\hat{v}_o(j\,2\pi\tilde{f}_{c,l})$ is equal to $\hat{v}_x(j\,2\pi\tilde{f}_{c,l}) = \hat{v}_y(j\,2\pi\tilde{f}_{c,l})$. Thus, calculation of k_T only needs the output current i_o in addition to the signals used in the loop gain monitoring part (v_x, v_y).

The 2-by-2 tuning matrix **A** is designed based on the external loop plant, similarly to [67, 85]. Herein, for simplicity, **A** is assumed to consist of only integral terms:

$$\mathbf{A}(\mathbf{s}) = \begin{bmatrix} a_1/s & a_2/s \\ a_3/s & a_4/s \end{bmatrix} \tag{5.20}$$

The integral gains a_1, a_2, a_3, a_4 are chosen numerically; based on the small-signal variations of the crossover frequency and peak bus impedance, under changes in the proportional and integral gains of the voltage regulator [85]. It is worth mentioning that the reference value for the peak of bus impedance k_b^* is chosen so as to satisfy the PBSC and AIR, discussed in Section 5.2. If the peak of bus impedance always maintains a desired margin with respect to the load subsystem impedance, we can make sure that the system is always damped. In particular, herein a 4 dB gain margin between the bus impedance and the load subsystem impedance is considered: k_b^*/k_T=-4 dB. This margin is obtained by following a design procedure similar to [32]. Notice also that, comparing with (5.13), this corresponds to a voltage loop phase margin of 45 deg.

5.6 Case Study and Experimental Results

Fig. 5.12 shows the prototype considered in this work, which emulates an islanded dc microgrid. It consists of two buck converters. The source-side converter emulates a DER converter, and the load-side converter acts as a CPL over the bandwidth of the source converter. The setup parameters are listed in Table 5.4. The proposed peak bus impedance monitoring and tuning tool shown in Fig. 5.11 is implemented in the digital controller of the source converter (dSPACE DS1104 in this prototype).

The source converter controller contains two control loops: the inductor current loop, and the output voltage loop. The current and the voltage regulators ($G_i(s)$, $G_v(s)$) are designed based on standard procedures [39], for a nominal resistive load. In particular, the current loop bandwidth and phase margin are, respectively, 1 kHz, and 80 deg, and the voltage loop bandwidth and phase margin are, respectively, $f_c = 100\,\text{Hz}$, and $\phi_m = 55$ deg. However, when connecting the source

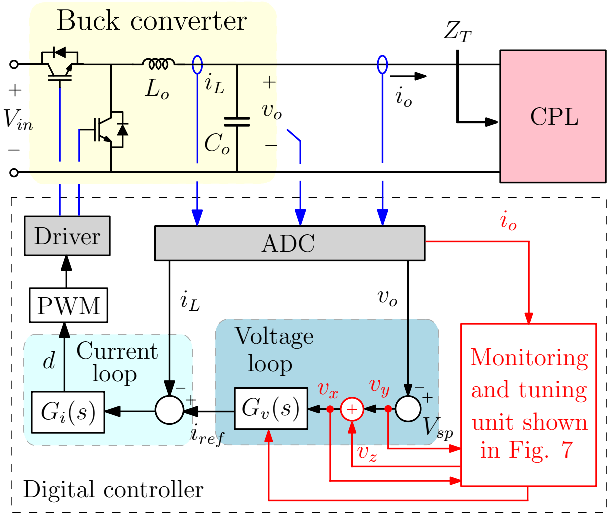

Fig. 5.12. The laboratory setup emulating an islanded dc microgrid. The source converter implements the online monitoring and tuning tool in Fig. 5.11.

converter to the CPL, the stability margins of the voltage loop significantly change, while those of the current remain almost the same.

In order to validate the proposed monitoring and tuning approach, the voltage loop gains and the bus impedances in different cases are plotted and compared with the experimentally measured ones. To obtain the measurements, a small-signal pseudo-random binary sequence (PRBS) is injected on top of the converter's duty cycle, to stimulate the system over a wide-frequency range. The desired transfer function is, then, found by performing Fourier Transform of the input and output, and calculating their ratio. PRBS-based frequency response measurement is well known because of its accurate and fast online measurement features, and it is well-documented in the literature [46,94]. Notice that these measurements are used for validation only and are not needed for the adaptive control technique implementation. A detailed investigation about PRBS-based bus impedance measurement is addressed in [32], based on which, a PRBS is injected in the control feedback

Parameter	Symbol	Value
Input voltage	V_{in}	200 V
Nominal bus voltage	V_{bus}	100 V
Nominal power	P^{nom}	1 kW
Output side inductance	L_o	1 mH
Output side capacitance	C_o	90 µF
Switching frequency	f_{sw}	20 kHz

Table 5.4: Parameters of the setup shown in Fig. 5.12

of the source converter to measure the load input impedance. Likewise, another PRBS that is orthogonal to the first one, is injected in the control feedback of the load converter to measure the source output impedance. As the perturbations are orthogonal, they can be injected at the same time without affecting the identification result. Then, the parallel combination of the obtained source and load impedances is computed as the bus impedance. In this chapter, the approach discussed in [32] is used to measure the bus impedance, while the implementation details are skipped to save space.

5.6.1 Before tuning

As mentioned above, the 450 W CPL leads to a decrease in the phase margin of the voltage loop (i.e., from 55 deg to 20 deg), as shown in Fig. 5.13. According to (5.13), this phase margin estimates a peak value of about 30 dB for the bus impedance (using $k_T = \frac{100^2}{450}$). To further validate this estimation, the bus impedance is experimentally measured and plotted in Fig. 5.14. As can be seen the actual value of the peak bus impedance is 27 dB, which is close to the peak value estimated based on the phase margin.

The above experiment is repeated with less CPL power (i.e., 225 W). Also for this case, the voltage loop gain and the bus impedance are respectively shown in Fig. 5.15 and Fig. 5.16, in both of which the analytical models are compared with

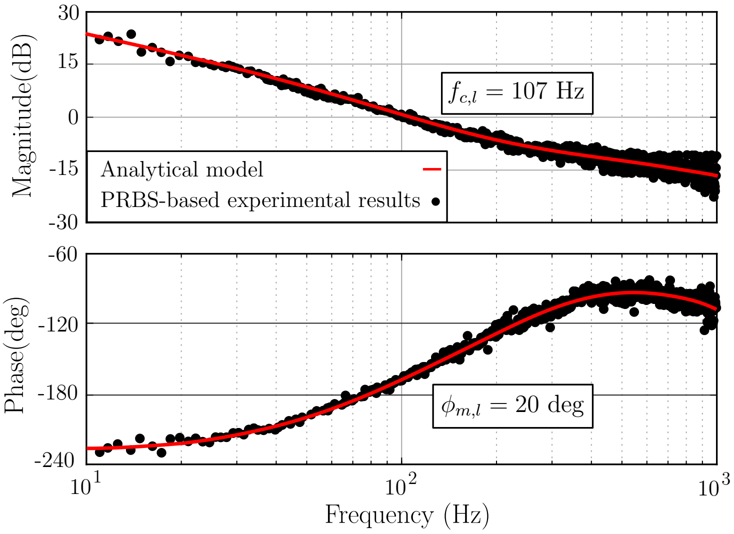

Fig. 5.13. Analytical and experimentally measured voltage loop gain $T_{v,l}$, with $P_{CPL} = 450$ W.

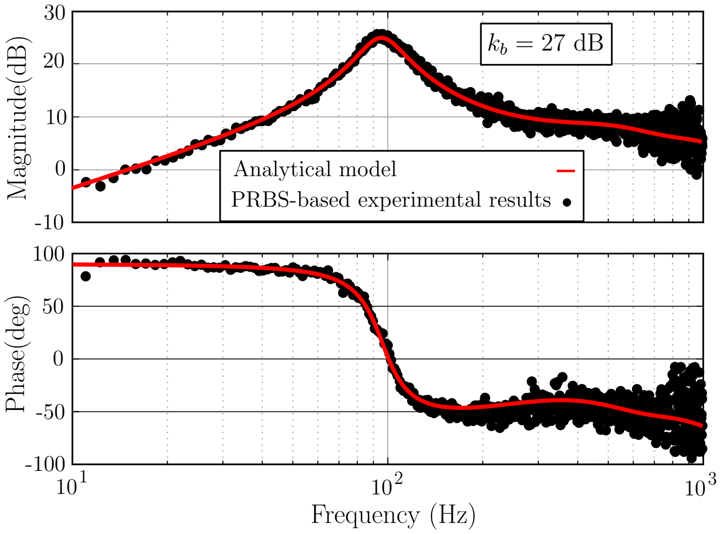

Fig. 5.14. Analytical and experimentally measured bus impedance Z_{bus}, with $P_{CPL} = 450$ W.

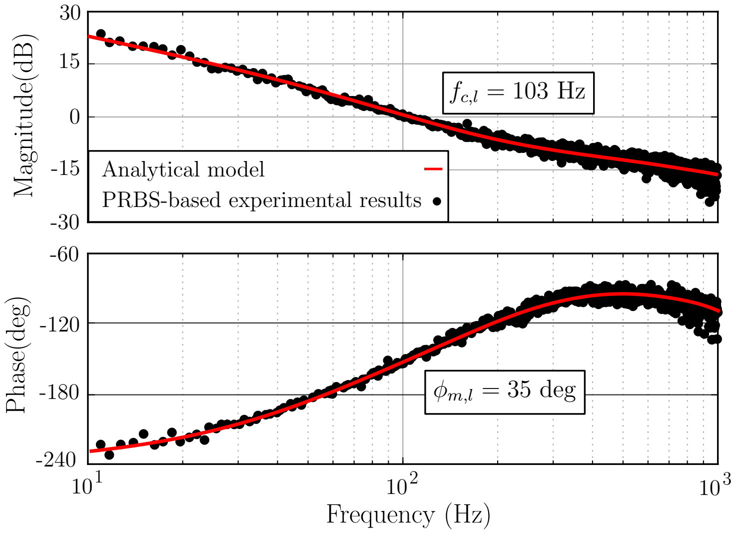

Fig. 5.15. Analytical and experimentally measured voltage loop gain $T_{v,l}$, with $P_{CPL} = 225$ W.

the experimental measurement results. Similarly to the previous case, the estimated bus impedance based on the phase margin (i.e., 27 dB) is near to measured value in Fig. 5.16 (i.e., 24.5 dB).

Regarding the figures Fig. 5.13, Fig. 5.14, Fig. 5.15 and Fig. 5.16 it is worth highlighting that in all cases the analytical models match well with the experimentally-measured frequency responses. This verifies the correctness of the performed analysis.

Fig. 5.17 shows the experimental results of the monitored crossover frequency and phase margin, as well as the peak bus impedance. In addition, the performance of

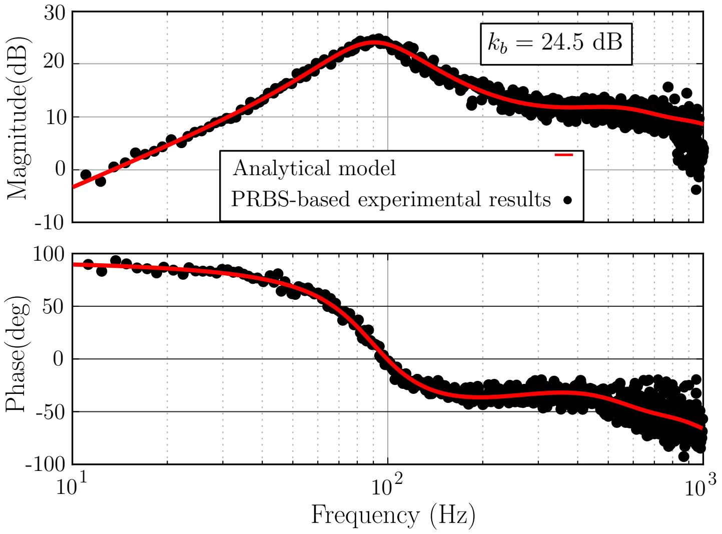

Fig. 5.16. Analytical and experimentally measured bus impedance Z_{bus}, with $P_{CPL} = 225$ W.

the proposed monitoring tool under a transient in the system is evaluated. In particular, when the CPL power is decreased from 450 W to 225 W, the phase margin is increased and the peak bus impedance is decreased. This is an interpretation of (5.1), according to which, the less CPL power implies the less destabilizing effect. The contrary holds for the case when the CPL power is increased from 225 W to 450 W. Notably in Fig. 5.17, the estimated phase margins are close to the measured ones in Fig. 5.13 and Fig. 5.15. Also the peak values of bus impedance are near to the measured values in Fig. 5.14 and Fig. 5.16. Based on Fig. 5.14, it

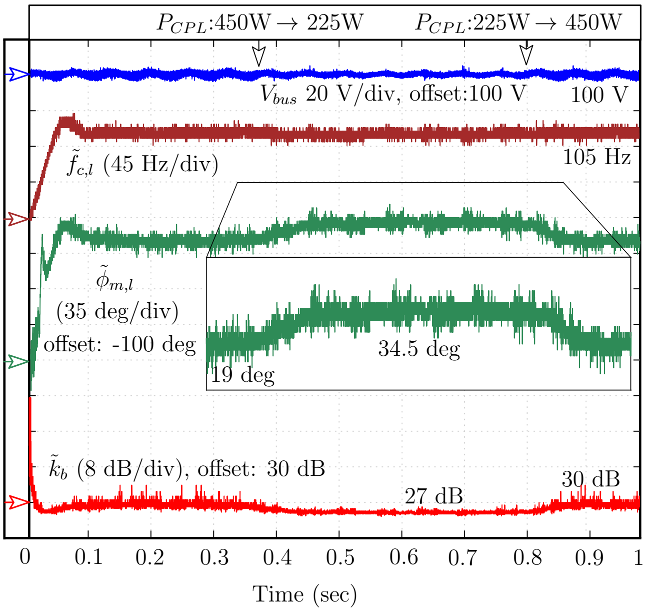

Fig. 5.17. Experimental results of the proposed monitoring tool in steady-state and under transient.

can be seen that the phase of the bus impedance is confined within the -90 deg, $+90$ deg sector. Also, the bus impedance only includes RHP poles, although the poles are not herein plotted, due to space limits. Thus, based on the discussion of Section 5.2, the PBSC is not violated. However, the relatively large resonance in Z_{bus} leads to a low damping level in the interconnected system. This is also confirmed by the phase margin of 20 deg in Fig. 5.13, which considerably deviates from the original one (55 deg). Therefore, we should tune the voltage regulator of the source $G_v(s)$, in order to damp the bus impedance, which also will increase the phase margin.

5.6.2 After tuning

The tuning action is implemented on the source converter of the setup shown in Fig. 5.12 (by keeping the CPL power at 450 W). To implement the tuning, in this work, we set the reference value of the peak bus impedance k_b^* to 22 dB, which is chosen based on the 4 dB gain margin criterion discussed in Section 5.5. This will limit the bus impedance inside an allowable region. On the other hand, the estimations of this work are based on assuming the resonance frequency of bus impedance to be close to the designed bandwidth of the voltage loop f_c. Therefore, in general, the reference crossover frequency should stay close to the originally-designed bandwidth, i.e., $\omega_o^* \simeq 2\pi f_c$. Nevertheless, in the following experiment, we slightly increase the reference crossover frequency (from 100Hz to 125 Hz), in order to evaluate the performance of the proposed estimation and monitoring unit under some discrepancy between the voltage loop bandwidth and the bus impedance resonance frequency ($\omega_o^* \simeq 2\pi 125$ rad/s). In this work, a diagonal tuning matrix $\mathbf{A}$ is used, with the following integral gains: $a_1 = 0.001$, $a_2 = 0$,$a_3 = 0$, $a_4 = 0.28$.

Experimentally-measured frequency response of the voltage loop, after tuning the $G_v(s)$ parameters, is shown in Fig. 5.18. In this figure, the analytical model of the voltage loop is plotted by applying the updated values of k_i, k_p. As can be seen, the new phase margin is 50 deg, confirming, thus, the successful improvement of the dynamic performance. Using this value to estimate the peak bus impedance based on (5.13), gives 23 dB. The close matching between the new value of the peak bus impedance and the reference value, confirms the correct tuning of the voltage regulator, that leads to the desired damping of the bus impedance. It is worth mentioning that, a similar test with $\omega_o^* \simeq 2\pi 100$ red/s is also performed and similar damping is observed. However, for brevity, the results of this additional experiment are not herein reported.

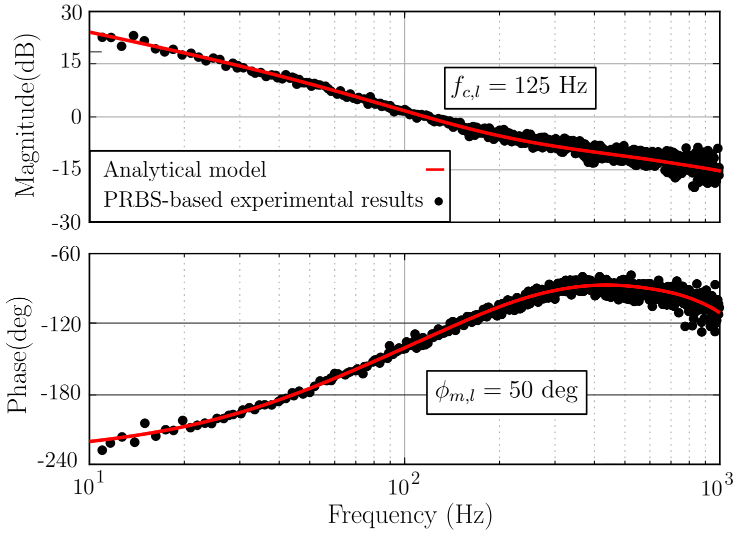

Fig. 5.18. Analytical and experimentally measured voltage loop gain $T_{v,l}$, after tuning G_v.

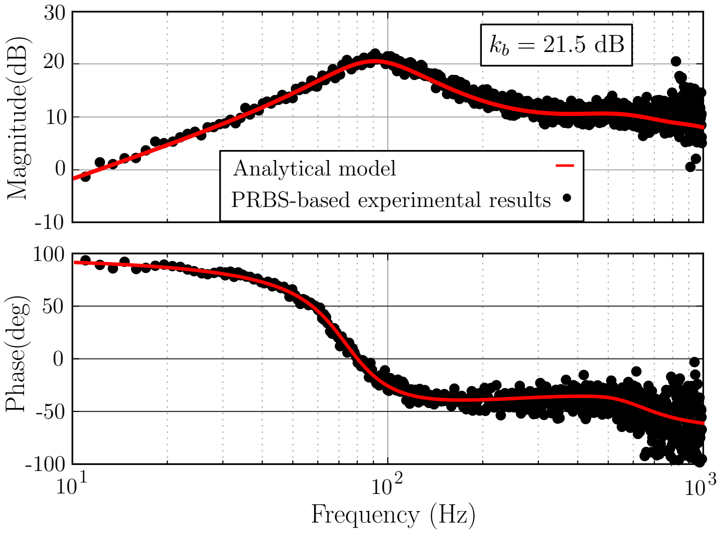

Fig. 5.19. Analytical and experimentally measured bus impedance Z_{bus}, after tuning G_v.

Similarly to the case before tuning, also here the accuracy of the implemented monitoring tool is verified by bus impedance measurement. Experimentally-obtained frequency response of the bus impedance is compared with the analytical model (plotted by using the new k_i, k_p) in Fig. 5.19. As can be seen, a good matching is observed between the analytical model and the experimental measurements. Also, the 21.5 dB peak value of bus impedance highlights two important points: a) correctness of the implemented monitoring tool, despite the existing difference between bus impedance resonance and crossover frequency of the voltage loop b) successful damping of the bus impedance by means of the proposed tuning approach.

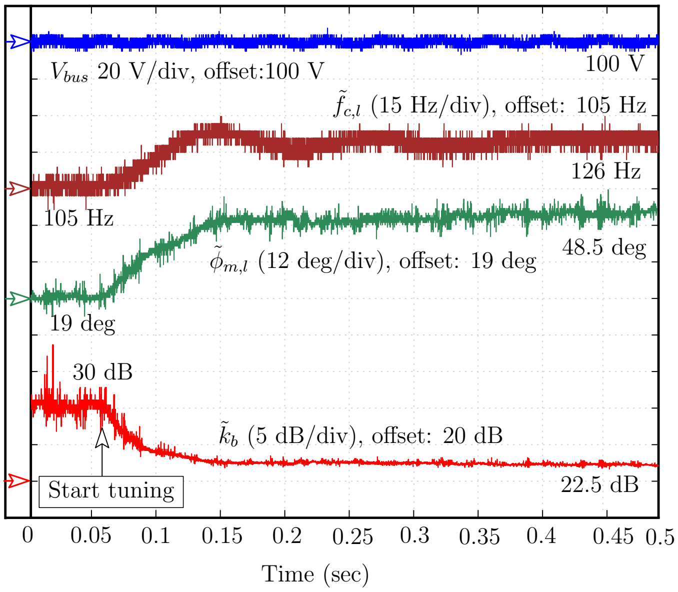

Fig. 5.20. Experimental results of the proposed monitoring and tuning unit.

	$\tilde{k}_b$ monitored online (Fig. 5.17, Fig. 5.20)	$\tilde{k}_b$ estimated based on $\phi_{m,l}$ (Fig. 5.13, Fig. 5.18)	k_b measured (Fig. 5.14, Fig. 5.19)
before tuning	30 dB	30 dB	27 dB
after tuning	22.5 dB	23 dB	21.5 dB

Table 5.5: Summary of the experimental results of the peak value of bus impedance

Fig. 5.20 shows the experimental results of the proposed monitoring and tuning unit. In particular, the crossover frequency, the phase margin, and the peak bus impedance are shown. As can be seen, when starting to tune the PI gains, the estimated phase margin increases and the peak bus impedance accordingly decreases, as expected by the bus impedance damping goal. The monitored value of phase margin after tuning is close to the measured one in Fig. 5.18. Also the peak value of bus impedance is near to the measured value in Fig. 5.19. Also the crossover frequency increases to around the reference value.

Table 5.5 summarizes the experimental results of the peak value of bus impedance before and after tuning. The estimations based on the phase margin, as well as those monitored online are also included. As can be seen, a good matching can be observed both before and after tuning, confirming the accuracy of the estimations as well as the successful achievement of the tuning goal.

Finally, Fig. 5.21 shows the bus voltage, under a step change in the CPL power. In particular, the step response of the bus voltage both before and after tuning G_v parameters is displayed. As can be seen, the system is well-stabilized by

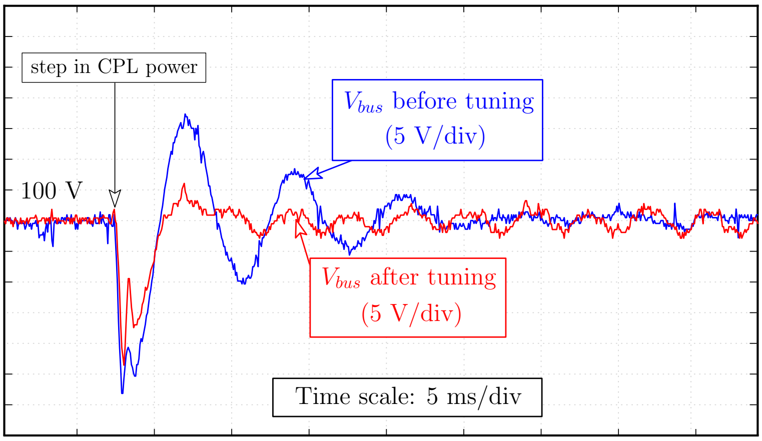

Fig. 5.21. Experimental results of the bus voltage step response before and after tuning G_v.

the proposed online monitoring and tuning approach. Notably, despite the high level of noise in the laboratory prototype, the monitoring unit provides accurate estimations, and accordingly, the tuning part shows a good performance. Hence, both time-domain and frequency-domain information of the system confirm the effectiveness of the proposed stabilization method.

5.7 Summary

This chapter proposes to estimate the peak value of bus impedance in dc microgrids based on the phase margin of the voltage (or droop) loop of a generic DER power converter. The Middlebrook's injection method allows to estimate the crossover frequency and the phase margin of the voltage or droop loop. The obtained phase margin is then used to estimate the peak value of bus impedance, based on which, the stability of an interconnected power converter system can be understood. Subsequently, the voltage regulator parameters can be effectively tuned, in order to damp the bus impedance, ensuring, thus, reliable operation of the dc microgrid. The proposed monitoring and tuning method is applied to a laboratory setup. In order to validate the estimation accuracy, the frequency responses of bus impedance and voltage loop gain are experimentally measured. According to the reported results, the estimated peak values of bus impedance show a good matching with the values obtained from the measured bus impedance. Experimentally measured loop gains also confirm the correctness of the phase margins used to estimate the bus impedance. In addition, the high peak in bus impedance (low phase margin) is effectively damped by using the applied tuning algorithm. In conclusion, the proposed method eliminates the need for impedance measurement, is simple to implement, is accurate, and is robust against noise and perturbations that may come from other paralleled converters. These properties make this approach practical for dc microgrid applications.

Chapter 6

Conclusions and Future Work

Power electronic converters used in a dc microgrid environment are usually equipped with several control loops. When many converters are connected to a common dc bus, the performance of some loops can be different from the behavior designed for the standalone converter, depending on the number, topology, and control of the interconnected converters. Thus, in order to know the performance of each loop in real-time, it is important to perform online and continuous stability monitoring. The monitored data can be effectively utilized to tune the controller of the loop under study, with the aim to keep a desired dynamic performance for each power converter, regardless of the interconnected converters.

This work firstly, investigates an on-line stability monitoring technique for power converters operating in dc microgrids. The technique is inspired by the Middlebrook's injection method, and allows to estimate and monitor the stability margins of any control loop under consideration (e.g., current, voltage, or droop control loops). Since we target a multi-converter environment, the presence of multiple perturbations coming from the monitoring units of several converters is also taken into account. For the experimental validation, a laboratory setup composed of three buck converters, a CPL, and a resistive load is implemented to emulate a dc microgrid. Then, the proposed monitoring tool is applied to different control loops. The obtained accuracy in the estimated stability margins, both in steady-state condition and under a transient, validate the effectiveness of the proposed monitoring technique.

Then, two different on-line tuning techniques are proposed, which are both based on injecting a small-signal perturbation at the desired crossover frequency into a generic SMPS control loop. The signals right before, and right after the injection point are then processed and, subsequently, some error vectors are defined. Finally, the regulator parameters are tuned to make the error signal converge to zero, allowing, thus, to achieve the desired phase margin and crossover frequency. In addition, the situation in which an unfeasible phase margin is desired, is also taken into account. This case can happen when the applied regulator provides its maximum allowable phase to compensate a generic control loop, at the reference crossover frequency; but, still the phase margin of that loop is less than the desired reference phase margin. These tuning techniques are also experimentally verified in the laboratory setup described above.

As the stability margins monitored online do not give a full picture of the control performance, sometimes it might be necessary to monitor the loop gain frequency response over the entire bandwidth. To do so, this work proposes to use PRBSs because of their well known advantages, i.e., the short identification time, the adjustable injection bandwidths, the simple generation algorithm, the low peak factor, and most importantly, the possibility to generate several PRBSs with different frequency components (orthogonal PRBSs). In this research, we propose simultaneous injection of multiple orthogonal PRBSs into different control loops of dc microgrid power converters. By doing so, the frequency responses of all the desired control loops can be measured within a single experiment, providing, thus, a rapid loop gain monitoring. The proposed identification algorithm is experimentally verified in the dc microgrid setup described above. Also, the necessity of having multiple excitations to perform multiple loop gain identification is experimentally confirmed. Finally, the experimental identification results are used in adaptive tuning of a generic control loop, in order to achieve a desired dynamic performance.

Although stability monitoring of a generic control loop within dc microgrid converters, takes account for the effect of other converters connected to the same dc bus, but some loops may not provide a comprehensive and system-level stability assessment. In this context, the dc bus impedance is defined in the literature as the parallel combination all the source and load converters impedances. Bus impedance has been demonstrated to give a stability measure of the whole dc microgrid. This work proposes to estimate the peak value of bus impedance based on the phase margin of the voltage (or droop) loop of a generic DER power converter. To this end, the monitored phase margin described above is utilized. The obtained peak bus impedance is then damped by tuning the voltage regulator parameters, that can ensure a reliable operation for the dc microgrid. Experimental implementation of this technique proves the applicability of the proposed method in online estimation and damping of dc microgrid bus impedance.

Based on the experimental results in all of the above-mentioned loop gain injection cases, the bus voltage and the inductor current are not significantly affected by the small-signal perturbations. Because the provisions discussed in this work are applied to the perturbation amplitudes.

To summarize, in the context of a smart dc microgrid, the proposed online stability monitoring is showing merit. This can be followed by the proposed autotuning methods to ensure a reliable operation of the system. In other cases—where a full picture about the performance of different loops over the entire bandwidth is desired—multiple orthogonal PRBSs can be simultaneously injected in several control loops. This will provide the frequency responses of all the loops in a single measurement cycle. Finally, in order to further assess the microgrid-level stability and dynamic performance, the monitored phase margin of some loops can be effectively used to estimate the peak value of the dc bus impedance.

Several aspects of this research can be further investigated in future. In particular:

- Extension of the proposed stability monitoring and autotuning techniques to the ac microgrids requires a dedicated study. In this case, if we assume to work in *dq* synchronous reference frame, we shall deal with MIMO loop gain measurement and MIMO stability analysis, which is of course, of particular interest.

- This work proposes to simultaneously inject N orthogonal PRBSs to identify N generic control loops within dc microgrid power converters, in one measurement cycle. Based on the orthogonal PRBS generation algorithm discussed in Chapter 4, this technique leads to an increase in the measurement time by a factor of two, for each additional loop. However, by further signal processing steps, one can apply a single PRBS with N different modulation indexes for N different control loops. This way, the identification time of N control loops remains equal to the one of a single loop. A future investigation on this is very appealing from many perspectives.

- The proposed bus impedance estimation technique is performed based on the phase margin of the voltage (or the droop) loop of source-side converters.

In this case, the main assumption is that, the crossover frequency of the voltage (or the droop) loop is very close to the resonance frequency of the bus impedance. The validity of this assumption is shown by a literature search and some simulation and experimental studies. However, in order to establish a generic relationship between bus impedance and phase margin, some future investigations are necessary.

Bibliography

[1] P. Fairley, "Edison's revenge: the rise of dc power," *MIT Technology Review*, 2012.

[2] T. Dragicevic, J. C. Vasquez, J. M. Guerrero, and D. Skrlec, "Advanced lvdc electrical power architectures and microgrids: A step toward a new generation of power distribution networks." *IEEE Electrification Magazine*, vol. 2, no. 1, pp. 54–65, March 2014.

[3] Russel Gold, "One Man's Quest to Transform American Energy," *Simon and Schuster, Inc., Wall Street Journal*, 2019.

[4] R. H. Lasseter, "Microgrids," in *2002 IEEE Power Engineering Society Winter Meeting. Conference Proceedings (Cat. No. 02CH37309)*, vol. 1. IEEE, 2002, pp. 305–308.

[5] P. Wang, L. Goel, X. Liu, and F. H. Choo, "Harmonizing ac and dc: A hybrid ac/dc future grid solution," *IEEE Power and Energy Magazine*, vol. 11, no. 3, pp. 76–83, 2013.

[6] M. I. Henderson, D. Novosel, and M. L. Crow, "Electric power grid modernization trends, challenges, and opportunities," *no. November*, 2017.

[7] PwC global power & utilities, "Electricity beyond the grid - Accelerating access to sustainable power for all," Tech. Rep., 2016. [Online]. Available: https://www.pwc.com/gx/en/energy-utilities-mining/pdf/electricity-beyond-grid.pdf

[8] P. C. Loh, D. Li, Y. K. Chai, and F. Blaabjerg, "Autonomous operation of hybrid microgrid with ac and dc subgrids," *IEEE transactions on power electronics*, vol. 28, no. 5, pp. 2214–2223, 2012.

[9] R. W. De Doncker, "Power electronic technologies for flexible dc distribution grids," in *2014 International Power Electronics Conference (IPEC-Hiroshima 2014-ECCE ASIA)*. IEEE, 2014, pp. 736–743.

[10] T. Dragičević, X. Lu, J. C. Vasquez, and J. M. Guerrero, "Dc microgrids—part ii: A review of power architectures, applications, and standardization issues," *IEEE Transactions on Power Electronics*, vol. 31, no. 5, pp. 3528–3549, 2015.

[11] N. C. Ekneligoda and W. W. Weaver, "A game theoretic bus selection method for loads in multibus dc power systems," *IEEE Transactions on Industrial Electronics*, vol. 61, no. 4, pp. 1669–1678, 2013.

[12] R. S. Balog and P. T. Krein, "Bus selection in multibus dc microgrids," *IEEE Transactions on Power Electronics*, vol. 26, no. 3, pp. 860–867, 2010.

[13] G. AlLee and W. Tschudi, "Edison redux: 380 vdc brings reliability and efficiency to sustainable data centers," *IEEE Power and Energy Magazine*, vol. 10, no. 6, pp. 50–59, 2012.

[14] R. W. De Doncker, C. Meyer, R. U. Lenke, and F. Mura, "Power electronics for future utility applications," in *2007 7th International Conference on Power Electronics and Drive Systems.* IEEE, 2007, pp. K–1.

[15] F. Blaabjerg, Z. Chen, and S. B. Kjaer, "Power electronics as efficient interface in dispersed power generation systems," *IEEE transactions on power electronics*, vol. 19, no. 5, pp. 1184–1194, 2004.

[16] R. M. Strzelecki, *Power electronics in smart electrical energy networks.* Springer Science & Business Media, 2008.

[17] G. Liu, T. Caldognetto, and P. Mattavelli, "Power-based droop control in dc microgrids enabling seamless disconnection from ac grids," in *2017 IEEE Second International Conference on DC Microgrids (ICDCM)*, 2017, pp. 523–528.

[18] X. Lu, J. M. Guerrero, K. Sun, and J. C. Vasquez, "An improved droop control method for dc microgrids based on low bandwidth communication with dc bus voltage restoration and enhanced current sharing accuracy," *IEEE Transactions on Power Electronics*, vol. 29, no. 4, pp. 1800–1812, April 2014.

[19] S. I. Gkavanoudis, K. O. Oureilidis, and C. S. Demoulias, "An adaptive droop control method for balancing the soc of distributed batteries in ac microgrids," in *IEEE 17th Workshop on Control and Modeling for Power Electronics (COMPEL), 2016*, pp. 1–6.

[20] V. Nasirian, S. Moayedi, A. Davoudi, and F. L. Lewis, "Distributed cooperative control of dc microgrids," *IEEE Transactions on Power Electronics*, vol. 30, no. 4, pp. 2288–2303, 2014.

[21] Y. Gu, W. Li, and X. He, "Frequency-coordinating virtual impedance for autonomous power management of dc microgrid," *IEEE Transactions on Power Electronics*, vol. 30, no. 4, pp. 2328–2337, April 2015.

[22] T. Dragičević, X. Lu, J. C. Vasquez, and J. M. Guerrero, "Dc microgrids—part i: A review of control strategies and stabilization techniques," *IEEE Transactions on power electronics*, vol. 31, no. 7, pp. 4876–4891, 2015.

[23] E. Koutroulis and K. Kalaitzakis, "Design of a maximum power tracking system for wind-energy-conversion applications," *IEEE transactions on industrial electronics*, vol. 53, no. 2, pp. 486–494, 2006.

[24] B. Subudhi and R. Pradhan, "A comparative study on maximum power point tracking techniques for photovoltaic power systems," *IEEE Transactions on sustainable energy*, vol. 4, no. 1, pp. 89–98, 2012.

[25] T. B. Reddy, *Linden's handbook of batteries.* McGraw-hill New York, 2011, vol. 4.

[26] L. Meng, A. Luna, E. R. Díaz, B. Sun, T. Dragicevic, M. Savaghebi, J. C. Vasquez, J. M. Guerrero, M. Graells, and F. Andrade, "Flexible system integration and advanced hierarchical control architectures in the microgrid research laboratory of aalborg university," *IEEE Transactions on Industry Applications*, vol. 52, no. 2, pp. 1736–1749, 2016.

[27] L. Che and M. Shahidehpour, "Dc microgrids: Economic operation and enhancement of resilience by hierarchical control," *IEEE Transactions on Smart Grid*, vol. 5, no. 5, pp. 2517–2526, 2014.

[28] B. Wang, M. Sechilariu, and F. Locment, "Intelligent dc microgrid with smart grid communications: Control strategy consideration and design," *IEEE transactions on smart grid*, vol. 3, no. 4, pp. 2148–2156, 2012.

[29] R. Thomas, "The stability of aircraft dc power systems with inverter loads," *Transactions of the American Institute of Electrical Engineers, Part II: Applications and Industry*, vol. 76, no. 4, pp. 183–188, 1957.

[30] N. O. Sokal, "System oscillations from negative input resistance at power input port of switching-mode regulator, amplifier, dc/dc converter, or dc/dc

inverter," in *1973 IEEE Power Electronics Specialists Conference.* IEEE, 1973, pp. 138–140.

[31] G. Venkataramanan and C. Marnay, "A larger role for microgrids," *IEEE Power and Energy Magazine*, vol. 6, no. 3, pp. 78–82, May 2008.

[32] H. Abdollahi, S. Arrua, T. Roinila, and E. Santi, "A novel dc power distribution system stabilization method based on adaptive resonance-enhanced voltage controller," *IEEE Transactions on Industrial Electronics*, vol. 66, no. 7, pp. 5653–5662, 2019.

[33] Y. Jang and R. W. Erickson, "Physical origins of input filter oscillations in current programmed converters," *IEEE Transactions on Power Electronics*, vol. 7, no. 4, pp. 725–733, 1992.

[34] R. D. Middlebrook, "Input filter considerations in design and application of switching regulators," *IEEE Industry Applications Society Annual Meeting, Chicago. Oct,1976*, pp. 366–382.

[35] X. Feng, J. Liu, and F. C. Lee, "Impedance specifications for stable dc distributed power systems," *IEEE Transactions on Power Electronics*, vol. 17, no. 2, pp. 157 – 162, March 2002.

[36] A. Emadi, A. Khaligh, C. H. Rivetta, and G. A. Williamson, "Constant power loads and negative impedance instability in automotive systems: definition, modeling, stability, and control of power electronic converters and motor drives," *IEEE Transactions on vehicular technology*, vol. 55, no. 4, pp. 1112–1125, 2006.

[37] A. Riccobono, M. Cupelli, A. Monti, E. Santi, T. Roinila, H. Abdollahi, S. Arrua, and R. A. Dougal, "Stability of shipboard dc power distribution: Online impedance-based systems methods," *IEEE Electrification Magazine*, vol. 5, no. 3, pp. 55–67, 2017.

[38] R. W. Erickson and D. Maksimovic, *Fundamentals of power electronics.* Springer Science & Business Media, 2007.

[39] L. Corradini, D. Maksimović, P. Mattavelli, and R. Zane, *Digital control of high-frequency switched-mode power converters.* John Wiley & Sons, 2015, vol. 48.

[40] M. Bhardwaj, S. Choudhury, R. Poley, and B. Akin, "Online frequency response analysis: A powerful plug-in tool for compensation design and health

assessment of digitally controlled power converters," *IEEE Transactions on Industry Applications*, vol. 52, no. 3, pp. 2426–2435, 2016.

[41] J. Castello and J. M. Espi, "Dsp implementation for measuring the loop gain frequency response of digitally controlled power converters," vol. 27, no. 9, pp. 4113–4121, Sept. 2012.

[42] M. Cespedes and J. Sun, "Adaptive control of grid-connected inverters based on online grid impedance measurements," *IEEE Transactions on sustainable energy*, vol. 5, no. 2, pp. 516–523, April 2014.

[43] A. Barkley and E. Santi, "Improved online identification of a dc–dc converter and its control loop gain using cross-correlation methods," *IEEE Transactions on power electronics*, vol. 24, no. 8, pp. 2021–2031, 2009.

[44] T. Roinila, M. Vilkko, and T. Suntio, "Fast loop gain measurement of a switched-mode converter using a binary signal with a specified fourier amplitude spectrum," *IEEE Transactions on Power Electronics*, vol. 24, no. 12, pp. 2746–2755, 2009.

[45] T. Roinila, J. Huusari, and M. Vilkko, "On frequency-response measurements of power-electronic systems applying mimo identification techniques," vol. 60, no. 11, pp. 5270–5276, Nov. 2013.

[46] T. Roinila, H. Abdollahi, S. Arrua, and E. Santi, "Adaptive control of dc power distribution systems: Applying pseudo-random sequences and fourier techniques," in *2018 International Power Electronics Conference (IPEC-Niigata 2018-ECCE Asia)*. IEEE, 2018, pp. 1719–1723.

[47] E. Santi, H. Y. Cho, A. B. Barkley, D. Martin, and A. Riccobono, "Tools to address system level issues in power electronics: The digital network analyzer method and the positive feedforward control technique," in *IEEE 8th International Conference on Power Electronics and ECCE Asia (ICPE & ECCE), 2011*, pp. 2106–2113.

[48] B. Miao, R. Zane, and D. Maksimovic, "Practical on-line identification of power converter dynamic responses," in *IEEE Twentieth Annual Applied Power Electronics Conference and Exposition (APEC 2005)*, pp. 57–62.

[49] G. E. Pitel and P. T. Krein, "Real-time system identification for load monitoring and transient handling of dc-dc supplies," in *IEEE Power Electronics Specialists Conference (PESC 2008)*, pp. 3807–3813.

[50] M. M. F. S. Algreer, “Microprocessor based signal processing techniques for system identification and adaptive control of dc-dc converters,” Ph.D. dissertation, School of Electrical and Electronic Engineering, Newcastle University, UK, 2012.

[51] R. D. Middlebrook, “Measurement of loop gain in feedback systems,” *International Journal of Electronics Theoretical and Experimental*, vol. 38, no. 4, pp. 485–512, 1975.

[52] J. Morroni, R. Zane, and D. Maksimovic, “An online stability margin monitor for digitally controlled switched-mode power supplies,” *IEEE Transactions on Power Electronics*, vol. 24, no. 11, pp. 2639–2648, 2009.

[53] N. Pogaku, M. Prodanovic, and T. C. Green, “Modeling, analysis and testing of autonomous operation of an inverter-based microgrid,” *IEEE Transactions on power electronics*, vol. 22, no. 2, pp. 613–625, 2007.

[54] K. Areerak, S. Bozhko, G. Asher, L. De Lillo, and D. W. Thomas, “Stability study for a hybrid ac-dc more-electric aircraft power system,” *IEEE Transactions on Aerospace and Electronic Systems*, vol. 48, no. 1, pp. 329–347, 2012.

[55] P. Magne, B. Nahid-Mobarakeh, and S. Pierfederici, “General active global stabilization of multiloads dc-power networks,” *IEEE Transactions on Power Electronics*, vol. 27, no. 4, pp. 1788–1798, 2011.

[56] L. Lewis, B. Cho, F. Lee, and B. Carpenter, “Modeling, analysis and design of distributed power systems,” in *20th Annual IEEE Power Electronics Specialists Conference*, 1989, pp. 152–159.

[57] M. Cespedes, L. Xing, and J. Sun, “Constant-power load system stabilization by passive damping,” *IEEE Transactions on Power Electronics*, vol. 26, no. 7, pp. 1832–1836, 2011.

[58] M. Belkhayat, R. Cooley, and A. Witulski, “Large signal stability criteria for distributed systems with constant power loads,” in *Proceedings of PESC’95-Power Electronics Specialist Conference*, vol. 2. IEEE, 1995, pp. 1333–1338.

[59] X. Wang, R. Yao, and F. Rao, “Three-step impedance criterion for small-signal stability analysis in two-stage dc distributed power systems,” *IEEE power electronics letters*, vol. 1, no. 3, pp. 83–87, 2003.

[60] C. M. Wildrick, F. C. Lee, B. H. Cho, and B. Choi, "A method of defining the load impedance specification for a stable distributed power system," *IEEE Transactions on power Electronics*, vol. 10, no. 3, pp. 280–285, 1995.

[61] H. Suryanarayana and S. Sudhoff, "Refinements in generalized immittance based stability analysis of dc power electronics based distribution systems," in *2015 IEEE Electric Ship Technologies Symposium (ESTS)*, 2015, pp. 80–85.

[62] A. Riccobono and E. Santi, "A novel passivity-based stability criterion (pbsc) for switching converter dc distribution systems," in *2012 Twenty-Seventh Annual IEEE Applied Power Electronics Conference and Exposition (APEC)*. IEEE, 2012, pp. 2560–2567.

[63] J. Siegers, S. Arrua, and E. Santi, "Allowable bus impedance region for mvdc distribution systems and stabilizing controller design using positive feed-forward control," in *2016 IEEE Energy Conversion Congress and Exposition (ECCE)*. IEEE, 2016, pp. 1–8.

[64] T. Roinila, H. Abdollahi, S. Arrua, and E. Santi, "Real-time stability analysis and control of multiconverter systems by using mimo-identification techniques," *IEEE Transactions on Power Electronics*, vol. 34, no. 4, pp. 3948–3957, 2019.

[65] T. Caldognetto, Q. Liu, and S. Buso, "Self-tuning of triple-loop controlled grid-connected inverters," in *2018 IEEE Energy Conversion Congress and Exposition (ECCE)*. IEEE, 2018, pp. 7121–7127.

[66] R. Hassan, H. Wang, and R. Zane, "Continuous stability monitoring of dc microgrids using controlled injection," in *2019 IEEE Applied Power Electronics Conference and Exposition (APEC)*. IEEE, 2019, pp. 1357–1364.

[67] L. Corradini, P. Mattavelli, W. Stefanutti, and S. Saggini, "Simplified model reference-based autotuningfor digitally controlled smps," *IEEE transactions on power electronics*, vol. 23, no. 4, pp. 1956–1963, 2008.

[68] S. Saggini, M. Loghi, O. Zambetti, A. Zafarana, and L. Corradini, "Autotuning technique for digital constant on-time controllers," in *2014 IEEE Applied Power Electronics Conference and Exposition-APEC 2014*, pp. 1059–1065.

[69] W. Stefanutti, P. Mattavelli, S. Saggini, and M. Ghioni, "Autotuning of digitally controlled dc–dc converters based on relay feedback," *IEEE Transactions on Power Electronics*, vol. 22, no. 1, pp. 199–207, 2007.

[70] I. Kaya and D. P. Atherton, "Exact parameter estimation from relay autotuning under static load disturbances," in *Proceedings of the American Control Conference,2001*, pp. 3274–3279.

[71] T. Strasser, F. Andrén, J. Kathan, C. Cecati, C. Buccella, P. Siano, P. Leitão, G. Zhabelova, V. Vyatkin, P. Vrba, and V. Mařík, "A Review of Architectures and Concepts for Intelligence in Future Electric Energy Systems," *IEEE Transactions on Industrial Electronics*, vol. 62, no. 4, pp. 2424–2438, April 2015.

[72] A. Khodamoradi, G. Liu, P. Mattavelli, T. Caldognetto, and P. Magnone, "Analysis of an on-line stability monitoring approach for dc microgrid power converters," *IEEE Transactions on Power Electronics*, 2018.

[73] ——, "On-line stability monitoring for power converters in dc microgrids," in *2017 IEEE Second International Conference on DC Microgrids (ICDCM)*. IEEE, 2017, pp. 302–308.

[74] T. Roinila, T. Messo, and E. Santi, "Mimo-identification techniques for rapid impedance-based stability assessment of three phase systems in dq domain," *IEEE Transactions on Power Electronics, Issue. 99*, 2017.

[75] T. Roinila, H. Abdollahi, S. Arrua, and E. Santi, "Online measurement of bus impedance of interconnected power electronics systems: Applying orthogonal sequences," in *2017 IEEE Energy Conversion Congress and Exposition (ECCE)*, pp. 5783–5788.

[76] J. G. Proakis, M. Salehi, N. Zhou, and X. Li, *Communication systems engineering*. Prentice Hall New Jersey, 1994, vol. 2.

[77] P. Tenti, A. Costabeber, P. Mattavelli, and D. Trombetti, "Distribution loss minimization by token ring control of power electronic interfaces in residential microgrids," *IEEE Transactions on Industrial Electronics*, vol. 59, no. 10, pp. 3817–3826, 2012.

[78] G. Liu, "Advanced controllers of power electronic converters in dc microgrids," Ph.D. dissertation, University of Padova, 2019.

[79] "SFRA tool." [Online]. Available: http://www.ti.com/tool/SFRA

[80] J. Morroni, A. Dolgov, M. Shirazi, R. Zane, and D. Maksimovic, "Online health monitoring in digitally controlled power converters," in *2007 IEEE Power Electronics Specialists Conference*. IEEE, 2007, pp. 112–118.

[81] B. Miao, R. Zane, and D. Maksimovic, "System identification of power converters with digital control through cross-correlation methods," *IEEE Transactions on Power Electronics*, vol. 20, no. 5, pp. 1093–1099, 2005.

[82] M. Shirazi, R. Zane, and D. Maksimovic, "An autotuning digital controller for dc–dc power converters based on online frequency-response measurement," *IEEE Transactions on Power Electronics*, vol. 24, no. 11, pp. 2578–2588, 2009.

[83] A. Barkley, R. Dougal, and E. Santi, "Adaptive control of power converters using digital network analyzer techniques," in *2011 Twenty-Sixth Annual IEEE Applied Power Electronics Conference and Exposition (APEC)*. IEEE, 2011, pp. 1824–1832.

[84] Z. Zhao and A. Prodi, "Limit-cycle oscillations based auto-tuning system for digitally controlled dc–dc power supplies," *IEEE Transactions on Power Electronics*, vol. 22, no. 6, pp. 2211–2222, 2007.

[85] J. Morroni, R. Zane, and D. Maksimovic, "Design and implementation of an adaptive tuning system based on desired phase margin for digitally controlled dc–dc converters," *IEEE Transactions on Power Electronics*, vol. 24, no. 2, pp. 559–564, 2009.

[86] A. Khodamoradi, G. Liu, and P. Mattavelli, "Auto-tuning of dc microgrid power converters based on a constant frequency injection," in *21th European Conference on Power Electronics and Applications (EPE'19 ECCE Europe)*, 2019.

[87] B. Subudhi and R. Pradhan, "A comparative study on maximum power point tracking techniques for photovoltaic power systems," *IEEE Transactions on sustainable energy*, vol. 4, no. 1, pp. 89–98, 2012.

[88] S. Anand and B. Fernandes, "Optimal voltage level for dc microgrids," in *IECON 2010-36th Annual Conference on IEEE Industrial Electronics Society*. IEEE, 2010, pp. 3034–3039.

[89] Y. Ito, Y. Zhongqing, and H. Akagi, "Dc microgrid based distribution power generation system," in *The 4th International Power Electronics and Motion Control Conference, 2004. IPEMC 2004.*, vol. 3. IEEE, 2004, pp. 1740–1745.

[90] A. Barkley and E. Santi, "Online monitoring of network impedances using digital network analyzer techniques," in *2009 Twenty-Fourth Annual IEEE*

Applied Power Electronics Conference and Exposition. IEEE, 2009, pp. 440–446.

[91] L. Lennart, "System identification: theory for the user," *PTR Prentice Hall, Upper Saddle River, NJ*, pp. 1–14, 1999.

[92] R. Luhtala, T. Roinila, and T. Messo, "Implementation of real-time impedance-based stability assessment of grid-connected systems using mimo-identification techniques," Sept.-Oct. 2018.

[93] T. Roinila and T. Messo, "Online grid-impedance measurement using ternary-sequence injection," 2018.

[94] K. Godfrey, *Perturbation signals for system identification.* Prentice Hall International (UK) Ltd., 1993.

[95] L. Yao, J. Zhao, and J. Qian, "An improved pseudo-random binary sequence design for multivariable system identification (a16-395)," in *2006 6th World Congress on Intelligent Control and Automation*, vol. 1, pp. 1768–1772.

[96] A. Khodamoradi, G. Liu, P. Mattavelli, and T. Messo, "Simultaneous identification of multiple control loops in dc microgrid power converters," *IEEE Transaction on Industrial Electronics*, 2019.

[97] G. Liu, P. Mattavelli, and S. Saggini, "Design of droop controllers for converters in dc microgrids towards reducing bus capacitance," in *20th European Conference on Power Electronics and Applications (EPE'18 ECCE Europe)*, 2018.

[98] R. Pintelon and J. Schoukens, *System identification: a frequency domain approach.* John Wiley & Sons, 2012.

[99] C. L. Phillips, "Analytical bode design of controllers," vol. 28, no. 1, pp. 43–44, 1985.

[100] L. Ntogramatzidis and A. Ferrante, "Exact tuning of pid controllers in control feedback design," *IET control theory and applications*, vol. 5, no. 4, pp. 565–578, 2011.

[101] K. J. Astrom and B. Wittenmark, "Adaptive control 2nd edition," *Addison-Wesley Pub Co.*, 1994.

[102] J. Maciejowski, *Multivariable Feedback Design*, ser. Electronic systems engineering series. Addison-Wesley, 1989.

[103] B. Wen, “Stability analysis of three-phase ac power systems based on measured dq frame impedances,” Ph.D. dissertation, Virginia Tech, 2015.

[104] S. D. Sudhoff, S. F. Glover, P. T. Lamm, D. H. Schmucker, and D. E. Delisle, “Admittance space stability analysis of power electronic systems,” *IEEE Transactions on Aerospace and Electronic Systems*, vol. 36, no. 3, pp. 965–973, Jul 2000.

[105] S. Vesti, T. Suntio, J. A. Oliver, R. Prieto, and J. A. Cobos, “Impedance-based stability and transient-performance assessment applying maximum peak criteria,” *IEEE Transactions on Power Electronics*, vol. 28, no. 5, pp. 2099–2104, May 2013.

[106] J. Liu, X. Feng, F. C. Lee, and D. Borojevich, “Stability margin monitoring for dc distributed power systems via perturbation approaches,” *IEEE transactions on power electronics*, vol. 18, no. 6, pp. 1254–1261, 2003.

[107] X. Feng, J. Liu, and F. C. Lee, “Impedance specifications for stable dc distributed power systems,” *IEEE Transactions on Power Electronics*, vol. 17, no. 2, pp. 157–162, 2002.

[108] J. Siegers, S. Arrua, and E. Santi, “Stabilizing controller design for multibus mvdc distribution systems using a passivity-based stability criterion and positive feedforward control,” *IEEE Journal of Emerging and Selected Topics in Power Electronics*, vol. 5, no. 1, pp. 14–27, 2016.

[109] F. Chen, R. Burgos, D. Boroyevich, J. Vasquez, and J. M. Guerrero, “Investigation of nonlinear droop control in dc power distribution systems: Load sharing, voltage regulation, efficiency and stability,” *IEEE Transactions on Power Electronics*, 2019.

[110] A. Aldhaheri and A. H. Etemadi, “Stabilization and performance preservation of dc–dc cascaded systems by diminishing output impedance magnitude,” *IEEE Transactions on Industry Applications*, vol. 54, no. 2, pp. 1481–1489, 2017.

[111] S. Abe, T. Ninomiya, M. Hirokawa, and T. Zaitsu, “Stability design consideration for on-board distributed power system consisting of full-regulated bus converter and pols,” in *2006 37th IEEE Power Electronics Specialists Conference*. IEEE, 2006, pp. 1–5.

[112] X. Feng, Z. Ye, K. Xing, F. C. Lee, and D. Borojevic, “Impedance specification and impedance improvement for dc distributed power system,” in

30th Annual IEEE Power Electronics Specialists Conference. Record.(Cat. No. 99CH36321), vol. 2. IEEE, 1999, pp. 889–894.

[113] X. Zhang, X. Ruan, and Q.-C. Zhong, "Improving the stability of cascaded dc/dc converter systems via shaping the input impedance of the load converter with a parallel or series virtual impedance," *IEEE Transactions on Industrial Electronics*, vol. 62, no. 12, pp. 7499–7512, 2015.

[114] L. Guo, S. Zhang, X. Li, Y. W. Li, C. Wang, and Y. Feng, "Stability analysis and damping enhancement based on frequency-dependent virtual impedance for dc microgrids," *IEEE Journal of emerging and selected topics in power electronics*, vol. 5, no. 1, pp. 338–350, 2016.

[115] M. E. Van Valkenburg, "Introduction to modern network synthesis," *John Wiley and Sons*, 1965.